



Title	Study on Fabrication and Self-Healing of Superoleophobic Practical Metal Surfaces
Author(s)	中山, 勝利
Citation	北海道大学. 博士(工学) 甲第12924号
Issue Date	2017-09-25
DOI	10.14943/doctoral.k12924
Doc URL	http://hdl.handle.net/2115/68224
Type	theses (doctoral)
File Information	Katsutoshi_Nakayama.pdf



[Instructions for use](#)

Study on Fabrication and Self-Healing of Superoleophobic Practical Metal Surfaces

by

Katsutoshi Nakayama

A Thesis

Submitted to the Graduate School of Chemical Sciences and
Engineering in Partial Fulfillment of the Requirements for the
Degree of Doctor of Philosophy in Engineering

at

Hokkaido University

September 2017

Table of Contents

<i>Chapter 1 Introduction</i>	1
1.1 Overview	2
1.2 Design of Superhydrophobic and superoleophobic surfaces	3
1.2.1 Theoretical basis	3
1.2.2 Examples of superhydrophobic surfaces	6
1.2.3 Design and examples of superoleophobic surfaces	7
1.3 Fabrication methods of rough engineering metal surfaces ..	8
1.3.1 Electrochemical and chemical etching	8
1.3.2 Anodizing	9
1.4 Surface compositions to control the wettability	12
1.4.1 Self-assembled monolayer coatings	12
1.4.2 Hydrophobic rare-earth oxide (REO)	13
1.5 Objective and construction of this thesis	15
1.5.1 Challenging issues practical superoleophobic surfaces	15
1.5.2 Objective in the research	16
1.5.3 Construction of thesis	17
References	17

3.4	Conclusions	67
	References.....	68
<i>Chapter 4 Self-Healing Superoleophobic Surface with Porous Anodic Alumina Surface..... 91</i>		
4.1	Introduction	92
4.2	Experimental	93
4.2.1	Formation of nanoporous surfaces.....	93
4.2.2	Formation of dual-pore hierarchically rough surface	93
4.2.3	Organic monolayer coating and infiltration of low-surface-tension molecules in nanopores.....	94
4.2.4	Characterizations	94
4.2.5	Wettability evaluations.....	95
4.3	Results and discussion	96
4.3.1	The effect of anodic nanopore diameter on the self-healing property	96
4.3.2	The effect of anodic nanopore length on the self-healing behavior	98
4.3.3	The self-healing superoleophobicity using dual-pore hierarchically rough aluminum surface.....	100
4.4	Conclusions	101
	References.....	102
<i>Chapter 5 Fabrication of Self-Healing Superhydrophobic CeO₂ Surface by Practical Electrochemical Processes..... 115</i>		

Table of Contents

5.1	Introduction	116
5.2	Experimental	117
5.2.1	Specimen preparation	117
5.2.2	Characterizations	118
5.2.3	Wettability evaluation	119
5.3	Results and discussion	120
5.3.1	CeO ₂ coating on stainless steel plate	120
5.3.2	Introduction of surface roughness of CeO ₂ for superhydrophobicity	123
5.3.3	Self-healing property of superhydrophobic CeO ₂ surface	126
5.3.4	Application to oil/water separation	127
5.4	Conclusions	128
	References.....	128
	<i>Chapter 6 General Conclusions</i>	143
	<i>Acknowledgements</i>	148
	<i>List of Publications</i>	151

Chapter 1

Introduction

1.1 Overview

It has been known that the surfaces of some plants and legs of some insects show superhydrophobic properties; for instance, lotus leaf is one of the most well-known examples. The superhydrophobic surface is often defined as a surface that show a water contact angle higher than $>150^\circ$, a very low water sliding angle, and/or low contact angle hysteresis, which is the difference of advancing and receding angles, of less than 10° . The superhydrophobicity on the lotus leaf results in self-cleaning property; contaminant particles on the leaf can be readily removed by water droplets in rainy days. Since early 1990s, an emergent progress of electron microscopy, which allows observation of surfaces at high resolution, disclosed that the high water repellency of the lotus leaf is originated from its hierarchical surface morphology, consisting of nanoscale needle-like wax crystals superimposed on microscale papillae [1]. In addition to lotus leaf, water strider's legs are also one of the most famous natural superhydrophobic surfaces. Water striders have non-wetting legs that enable them to stand effortlessly and move quickly on water. The feature believed due to a surface-tension effect caused by secreted wax as well as lotus leaf. In addition, the legs are covered by large numbers of oriented tiny hairs (microsetae) with fine nanogrooves [2]. Consequently, it is accepted that the key parameters to obtain superhydrophobic surfaces are surface geometry and surface composition (low surface free energy material).

Inspired by the nature, many efforts have been made in the last two decades to develop artificial superhydrophobic surfaces on engineering materials for various practical applications, such as self-cleaning, anti-icing, anti-fouling, anti-corrosion and

fluid drag reduction [3]. In many cases, even the produced surface is highly repellent to water, exposure to the ambient environment results in contamination with organic pollutions, e.g. oils, and consequently loss of superhydrophobic nature. Therefore, super-oil-repellent surfaces are needed for practical applications of superhydrophobic surfaces showing self-cleaning property. There are many reports for the fabrication of superoleophobic surfaces in the last decades, however, the superoleophobicity reported are mostly limited to liquids with surface tensions higher than $\sim 28 \text{ mN m}^{-1}$ [4]. Stability and durability of the superoleophobicity is also still challenging issue. In this thesis, the surface has been designed to show the real superoleophobicity even to liquids with surface tensions less than 20 mN m^{-1} . The surfaces have been fabricated only using industrially applicable wet processes. Attempts have been also made to introduce self-healing properties for durable super-liquid-repellency.

1.2 Design of superhydrophobic and superoleophobic surfaces

1.2.1 Theoretical basis

Pioneering work explaining the solid-liquid interactions was conducted by Thomas Young in 1805. According to his model, the surface of a liquid is an interface between that liquid and some other medium. The shape of a liquid droplet on a flat solid surface (e.g. contact angle θ) is described by the equilibrium among the solid surface tension (γ_S), the liquid surface tension (γ_L) and the interface tension between solid and liquid (γ_{SL}) at

contact point (Fig. 1.1). This balance is expressed using the Young's equation [5],

$$\gamma_S = \gamma_{SL} + \gamma_L \cos \theta \quad (1.1)$$

When the contact angles for a droplet are less or higher than 90° , the surface is “hydrophilic”/“hydrophobic” and “oleophilic”/“oleophobic” for water and oil, respectively. In particular, when the contact angles are higher than 150° , the surface is defined as “superhydrophobic” and “superoleophobic” for water and oil, respectively. For the practical use of engineering materials, in many cases, the surface modification needs to be performed on valve metals, on which a stable passivating oxide, hydroxide or oxyhydroxide layer is developed when contacting air because the oxidized state of those metals is more thermodynamically favorable. The oxidized surface has high surface energy, and therefore, the surfaces of valve metals and alloys are usually hydrophilic and oleophilic in nature. For the more active metals and alloys such as iron and magnesium, an organic paint layers are typically coated to improve their corrosion resistance. Because of the low surface energy of the organic layer, the coated metals and alloys in most cases are hydrophobic in nature. In spite of the fact that the metal surface is coated with an organic layer, the coated surface is usually oleophilic, because of low surface tensions of oil.

It is generally accepted that Young's equation is just applicable for an ideal smooth surface. As early as 1936, Wenzel reported the relationship between the water contact angle and the surface roughness [6]. This model assumed that the rough surface is completely wetted by water. In this mode, the apparent contact angle θ_R on a rough surface is described by the following equation,

$$\cos \theta_R = \frac{R(\gamma_S - \gamma_{SL})}{\gamma_L} = R \cos \theta \quad (1.2)$$

where R and θ are the roughness factor, which is the ratio of the actual rough surface to the projected area, and the intrinsic contact angle of the liquid droplet on a flat substrate, respectively. According to this equation, $\cos \theta_R$ should be large positive or negative values when θ is higher or lower than 90° , respectively. Hence, a wetting (hydrophilic or oleophilic) surface becomes more wetting, while a non-wetting (hydrophobic or oleophobic) surface becomes more non-wetting, as shown in Fig. 1.2.

When a porous surface is hydrophobic, the inside of pores cannot be filled with water. In 1944, Cassie and Baxter also proposed an extended model to describe the wettability on a composite solid surface consisting of two materials with different surface energies [7]. One of the solid materials can be replaced to air, as shown in Fig. 1.3. In this case, the apparent contact angle θ_R can be expressed by the following equation,

$$\cos \theta_R = f - 1 + f \cos \theta \quad (1.3)$$

where f and θ stand for the area fraction and the intrinsic contact angle of the solid surface, respectively.

By looking at the Young's equation, one may notice that the contact angle higher than 150° cannot be obtained for both water and oils even on a flat surface completely covered by $-\text{CF}_3$ groups with the lowest surface tension (6 mN m^{-1}) among all available materials. The report by Nishio et al. stands that the water contact angle on a CF_3 -covered flat glass surface can be $\sim 120^\circ$ at most [8]. Thus, surface roughness is needed to obtain a superhydrophobic surface.

In contrast, it is more difficult to obtain oleophobicity compared with hydrophobicity because the surface tensions of oils are typically much lower than that of water. According to Eq. (1.1), when the contact angle θ is 90° , γ_s must be equal to γ_{SL} . γ_{SL} can be approximated by the following equation [9],

$$\gamma_{SL} = \gamma_s + \gamma_L - \sqrt{\gamma_s \gamma_L} \quad (1.4)$$

Combining Eq. (1.1) and (1.4), $\gamma_s = \gamma_L/4$ for $\theta = 90^\circ$. Taking into account the above considerations one may easily understand that the γ_s value must be 5-7 mN m⁻¹ because typical surface tensions of oils are less than 30 mN m⁻¹. Such a small surface tension for a solid can probably be provided only by the $-\text{CF}_3$ groups. In other words, the contact angles of most oils are less than 90° even on the surface completely covered by organic groups. Hence, specific design is needed to develop superoleophobic surfaces.

1.2.2 Examples of artificial superhydrophobic surfaces

The superhydrophobicity and superoleophobicity indicate the surfaces on which the water and oil droplets present contact angles higher than 150° . As described examples in 1.1, there are many superhydrophobic surfaces with peculiar microstructures in nature. Inspired by natural features of super-repellent surfaces, the wettability of various materials has been changed either by creating a hierarchical rough microstructure, or by modifying the substrate with a layer of chemical coating. The pioneering research have been reported by Onda and Tsujii in 1996 [10]. They demonstrated superhydrophobic surface of alkylketendimer with fractal surface geometry with a contact angle of 174° . Tadanaga et al. fabricated a transparent superhydrophobic coating with nanoscale asperity

formed by boiling water treatment of an alumina thin film prepared by a sol-gel method, followed by fluoroalkylsilane (FAS) monolayer coating [11, 12]. The coating has been applied as an anti-reflection coating for inside lens of camera in 1997 [13].

A number of the reports on superhydrophobic surfaces have been shown during the past decades, demonstrating their applications as self-cleaning, anti-corrosion, icephobic coating, etc. [14-17]. However, the reported surfaces cannot repel oils; superhydrophobicity could be lost when oils adhere. Therefore, superoleophobic surfaces, which can repel oils, are needed to completely prevent contamination. Taking into account much lower surface tension of oil comparing to that of water, the formation of superoleophobic surface seems to be challenging even the surface is covered by $-\text{CF}_3$ [9, 18].

1.2.3 Design and examples of superoleophobic surfaces

In 2007, Tuteja et al. proposed and demonstrated that superoleophobic surfaces that are designed by the introduction of specific surface geometry: re-entrant or overhang, as shown in Figs. 1.4 [19, 20]. The reason for formation of specific contact angles is so called the “pinning effect” for liquids as demonstrated in Figs. 1.5. If one considers that the equilibrium contact angle of this liquid on the surface to be θ and the bending angle of the surface edge to be α , the liquid droplet cannot move over the edge of the solid surface until the contact angle exceeds $\theta + \alpha$. The contact angle is then in arbitrary value between θ and $\theta + \alpha$ in this situation, and can be much greater than the equilibrated value (θ) [21]. Thus, on the re-entrant or overhang morphologies, the interface which liquids shape convexity can be formed between liquids and air; the Cassie-Baxter condition with

air pocket in the gaps can be kept even for oils [19, 22]. In particular, introduction of superoleophobicity to practical metals is of crucial importance in industries. Hence, the most important key factor to fabricate superoleophobic practical metals is how to introduce peculiar morphologies on the surfaces.

1.3 Fabrication methods of rough engineering metal surfaces

Surface roughening of valve and non-valve metals is one of the most important methods to provide new functions, including high-liquid-repellency, for wide industrial applications. The surface roughening includes dry and wet processes such as: photolithography, sputtering, plasma etching, electroplating, film formation with sol-gel method, electrochemical etching and chemical etching, anodizing. However, the dry processes, including photolithography, sputtering or plasma etching, are not suitable for large-scale industrial production because these methods need large and expensive instruments. In this study, the author focuses on the practical wet processes, especially electrochemical and chemical etching and anodizing, which are most applicable for large-scale development, to introduce peculiar surface geometry on practical metal surfaces. This section describes on wet etching and anodizing processes.

1.3.1 Electrochemical and chemical etching

As described in the previous section, introduction of peculiar surface geometry is

needed to fabricate superoleophobic surface. Among some methods to control the metal surface morphology, etching is one of the efficient methods to fabricate superoleophobic surface with the introduction of peculiar surface geometry.

Etching is an active corrosion phenomenon in which solid surfaces, such as metals are dissolved in corrosive solutions. There are mainly two types of etching: electrochemical and chemical ones. In electrochemical etching, metals are dissolved under anodic polarized conditions. An example of the industrial use of the electrochemical etching is alternating current and direct current etching of aluminum foils used for electrolytic capacitor; the etching has been utilized to obtain anode with high surface areas [23, 24]. By adding oxidizing agents in corrosive solutions, etching of metals proceeds chemically. Under selected conditions, both chemical and electrochemical etching produce highly rough surfaces, which are suitable to control the surface wettability [25].

1.3.2 Anodizing

The anodizing is a high voltage electrochemical conversion process that forms barrier-type oxide layers or nanoporous/nanotubular oxides on valve metals and alloys, mainly depending on composition of electrolytes used [26]. The valve metals, such as aluminum, tantalum, niobium, titanium, tungsten, molybdenum, vanadium, bismuth, zirconium, hafnium, etc., are typically used, resulting in the oxide formation of thickness ranging from few nanometers to hundreds of micrometers [27, 28-37]. The recent reports also demonstrate possibility of oxide formation on active metals such as iron and steel

[37-42]. As shown in Fig. 1.6, the barrier-type film has compact structure and homogeneous film thickness, while porous film consists of many nanopores vertically arranged to the metal surface and semispherical barrier-layer underneath at the metal oxide interface [43, 44].

(a) Barrier-type anodic film

Usually anodizing deals with so called valve metals and for those metals and their alloys considerably thick anodic layers can be grown by applying relatively high voltage in suitable electrolyte. Some typical anodizing electrolytes are i) acidic electrolytes such as: sulfuric, oxalic, phosphoric acid, ii) neutral electrolytes such as: disodium molybdate, ammonium pentaborate [45-53]. The above conditions stand for most of valve metals except aluminum for which the dissolution is more governed by pH of electrolyte. Anodic oxide layers, *i.e.* barrier-type oxides, are considered to grow under high electric field mechanism. The growth of an oxide layer comprises simultaneous migration of cations towards the film/electrolyte interface and anions towards the metal/film interface [53-55]. The reason for the ions migration is that the high voltage is applied over the oxide layer, *i.e.*, electric field strength typically of the order of 10^8 V m^{-1} is established [44].

(b) Porous-type anodic film

The porous type oxides are mainly formed in the form of nanopores, e.g. anodic alumina or nanotubes, e.g. anodic titania [44, 56]. When aluminum is anodized in acidic or alkaline solutions, such as sulfuric acid [45, 46], oxalic acid [46-48], phosphoric acid

[49, 50], citric acid [57, 58], malic acid [59], tartaric acid [60], malonic acid [61], etidronic acid [62], chromic acid [63], and borax [64], the porous anodic films, which consist of many nanopores arranged vertically against metal substrate and semi-spherical barrier layer underneath porous one, can be formed, as shown in Fig. 1.6b [46, 65]. The ordered nanoporous/nanotubular structures are considered to be formed due to displacement of the film material above its original surface position due to synergistic effect of pits generation (field assisted oxide dissolution), stress generated at metal oxide interface, electrostriction, and plastic oxide flow, switching the growth of barrier-layer to nanotube/nanopore [45, 66].

Diameter of the pores and cells, that is the spherical unit of the barrier layer, depend on the formation voltage and electrolyte species. In addition, the cell arrangement, that is the pore arrangement, can be hexagonally self-organized. Ideally hexagonal arrangement can be obtained by control of electrolyte species and/or formation voltage. Typically, the diameters are amplified by increase of the voltage or using organic acid electrolytes with low acidity (Fig. 1.7) [46, 48, 49, 58, 62, 67, 68].

Pore geometry of anodic oxides is suitable to control of the surface wettability. In 2011, Fujii et al. have demonstrated a micro/nano-hierarchical structure, which was developed by oblique angle sputtering deposition of Al-Nb pillar arrays and successive anodizing in hot phosphate/glycerol, sulfuric and oxalic acid electrolytes. Superoleophobic surface was obtained, as shown in Fig. 1.8 [27, 69, 70].

1.4 Surface compositions to control the wettability

As describe above, in order to obtain high-liquid-repellent surfaces, the surface free energy of solid materials should be reduced. The surface free energy depends on the chemical composition. Zisman et al. reported that the surface free energy decreased in the order $-\text{CH}_2\text{CH}_2-$ (31 mN m^{-1}) $>$ $-\text{CH}_3$ ($22\text{-}24 \text{ mN m}^{-1}$) $>$ $-\text{CF}_2\text{CF}_2-$ (18 mN m^{-1}) $>$ $-\text{CF}_2\text{H}$ (15 mN m^{-1}) $>$ $-\text{CF}_3$ (6 mN m^{-1}) [71]. Thus, in order to control the surface free energy of solid materials, the surface should be covered by these organic groups entirely.

1.4.1 Self-assembled monolayer coatings

Self-assembled monolayer (SAM) coating, which is formed by chemical adsorption of organic molecules on solid material surfaces, is one of the most efficient methods to control of the surface wettability [72]. This is an ultra-thin coating which compact molecular aggregate can be formed with self-assembly due to interaction among adsorption molecules at the adsorption step. If correct organic species are selected, the surface function, reactivity and coating structure can be precisely controlled. For many oxides the surface is typically hydrophilic, and therefore coating with low-surface-tension material, such as $-\text{CH}_3$ or $-\text{CF}_3$, is desired to obtain super-liquid-repellency. This can be successfully realized by using SAMs in order to decrease the surface free energy [73-76].

One of the advantage of SAMs is that the monolayer can be easily formed on both flat and porous structures. The correct choose of head groups in the SAMs chain is particularly important in view of chemical bonding between molecule and desired substrate, and therefore provide proper coverage and adhesion for monolayer. Table 1.1

shows examples of typical combinations between substrate surfaces and organic molecules [28, 77]. For aluminum surface, for instance, alkylsilanes, alkylisocyanates, alkylphosphoric acids, alkylphosphonic acids or carboxylic acids have been used so far; some studies have reported that phosphoric acid or alkylphosphoric acid can form strong chemical bonds not only surface but also adjacent molecules as shown in Fig. 1.9 [28, 78, 79], while alkylisocyanates or carboxylic acids form only monolayer because of only one reactive group [78, 80].

Even though both alkylsilanes and alkylphosphoric acids are suitable species for aluminum, alkylphosphoric acids favor rather than alkylsilanes in case of hydrophobization with SAMs. Sato et al. have experimentally indicated this is due to high-molecular-ordering of alkylphosphoric acid compared to alkylsilanes [81, 82]. In addition, the authors have also reported that hydrophilization of substrate surface by plasma treatment before SAM coating is an important step to obtain ideal monolayer [82].

1.4.2 Hydrophobic rare-earth oxide (REO)

Although super-liquid-repellent surfaces have been developed with organic coatings, they have some disadvantages in practical applications, more specifically inherently poor mechanical, chemical and thermal stability. In order to improve the low-durability problem, hydrophobic properties have been explored in some inorganic metal oxides as well. In 2013, Azimi et al. reported that the rare-earth oxide (REO) material surfaces are highly hydrophobic and they are thermally stable even at 1000°C [83]. Typical surfaces of metal oxides, such as aluminum oxide, have a large number of polar

Table 1.1 Combination of head groups and substrates used in forming SAMs on metals, oxides and semiconductors [27, 76].

Molecules	Substrate
Alkyl thiol: R-SH	Metals Au, Ag, Cu, Ge, Pd, Hg, Ir, Ni, Pt, Zn, Fe, GaAs, InP
Carboxylic acid: R-COOH	Oxide Al ₂ O ₃ , AgO, CuO, Zr/Al ₂ O ₃ , Oxide-NH ₂ , Fe _x O _y , Ti/TiO ₂
Phosphonic acid: R-PO ₃ H ₂ Alkyl Phosphoric acid: RO-PO ₃ H ₂	Oxide ZrO ₂ , TiO ₂ , Al ₂ O ₃ , Ta ₂ O ₅ , Zr/Al ₂ O ₃
Organosilane: R-SiX ₃ X = Cl, OCH ₃ , OC ₂ H ₅	Oxide HfO ₂ , ITO, PtO, TiO ₂ , ZrO ₂ , Glass, Mica, SiO ₂ , SnO ₂ , GeO ₂ , Al ₂ O ₃ , SUS, PZT
Alkylamine: R-NH ₂	Semiconductor FeS ₂ , Mica, SUS316L, YBa ₂ Cu ₂ O _{7-δ}
Alkyl isocyanate: R-NCO	Oxide Al ₂ O ₃ , TiO ₂ , Oxide-COOH, -NH ₂
Monoalkyl silane: R-SiH ₃	Metal Au

sites originating from unsaturated metal and oxygen atoms that act as Lewis acid and base sites, respectively. Thus, a hydrogen bond can be formed with interfacial water molecules, resulting in hydrophilicity (Fig. 1.10a). On the other hand, metal atoms in REOs have a unique electron structure, where the inner unfilled $4f$ orbitals, which contribute to chemical reactions, are shielded by the filled outer $5s^2p^6$ orbitals. Consequently, these

metal atoms have lesser tendency to interact with water molecules. Hence, water molecules next to the surface cannot maintain their hydrogen-bonding network, resulting in hydrophobicity, as shown in Fig. 1.10b [83].

Azimi et al. have also demonstrated that the pellet or sputtered coating of REOs have high hydrophobicity, thermal stability and wear resistance. Since the REOs coated on the textured surface can exhibit superhydrophobicity [83]. It is expected that rare-earth oxide ceramics will find widespread applicability as robust hydrophobic surfaces.

1.5 Objective and construction of this thesis

1.5.1 Challenging issues practical superoleophobic surfaces

Recently, some researchers have reported super-liquid-repellent surfaces. However, most surfaces can repel liquids with limited surface tensions up to 27.5 mN m^{-1} (hexadecane); fabrication of super-liquid-repellent surfaces which can repel any liquid with surface tension less than that of hexadecane is still challenging. In addition, durability of the super-liquid-repellent surfaces must also be improved. Most superoleophobic surfaces reported so far are not sufficiently durable for practical applications. Superoleophobic surfaces are expected to be used for outdoor buildings, automobile engines, etc. Taking into account the above considerations, superoleophobic surfaces, which can resist any extrinsic stimuli, are needed.

For practical application of superoleophobic surfaces, durable surfaces should be developed by facile methods applicable for industrial scale. The super-liquid-repellent

surfaces are typically fabricated by complex and expensive dry processes such as lithography or sputtering, and therefore the exploration of a facile and scalable process is needed. As an applicable fabrication method of superoleophobic surfaces, practical wet process is promising. This process is facile and cheap, which can be completed by simply immersing the specimen in a solution. In order to extend the application of superoleophobic surfaces, the exploration of highly durable superoleophobic surfaces by wet process is greatly desirable.

1.5.2 Objective of the research

The main goal of this thesis is fabrication of super-liquid-repellent surfaces which are practically applicable in a large scale. More specifically, the author designs the micrometer-scale random roughness and more complex hierarchical geometry formed by chemical etching and subsequent anodizing, applicable to obtain superoleophobicity even for oil droplets with lower surface tension. Subsequently, the surface free energy is expected to be reduced by a coating of fluoroalkyl SAM, forming a superoleophobic surface (Fig. 1.11).

In order to improve the durability, the author expected to design self-healing events occurring on superoleophobic surface by infiltration of healing agent into anodized nanopores. In addition, as another improvement method of durability, the author also discusses the possibility of replacement of instable organic monolayer coating by hydrophobic rare-earth oxide coating which can be formed on a metal surface by practical electrochemical deposition.

1.5.3 Construction of thesis

This thesis consists of six chapters. In Chapter 1, the background of this study is described. In Chapter 2 and 3, fabrication of hierarchical aluminum surfaces, their surface wettability and durability are discussed. In Chapter 4, the self-healing property of super-liquid-repellent surface with anodized nanopores is discussed to improve the durability. Furthermore, cerium oxide coating formed by electrochemical process is described in Chapter 5, as a possible replacement of organic SAM. Finally, general conclusions of this thesis are described in Chapter 6.

References

- [1] W. Barthlott, C. Neinhuis, *Planta* **202**, 1 (1997).
- [2] X. Gao, L. Jiang, *Nature* **432**, 36 (2004).
- [3] J. Yong, F. Chen, Q. Yang, J. Huo, X. Hou, *Chem. Soc. Rev.* Advance Article (2017).
- [4] H. Bellanger, T. Darmanin, E. T. de Givenchy, F. Guittard, *Chem. Rev.* **114**, 2694 (2014).
- [5] T. Young, *Phil. Trans. Roy. Soc. London* **95**, 65 (1805).
- [6] R. N. Wenzel, *Ind. Eng. Chem.* **28**, 988 (1936).
- [7] A. B. D. Cassie, S. Baxter, *Trans. Faraday Soc.* **40**, 546 (1944).
- [8] T. Nishio, M. Megro, K. Nakamae, M. Matsushita, Y. Ueda, *Langmuir* **15**, 4321 (1999).
- [9] K. Tsujii, T. Yamamoto, T. Onda, S. Shibuuchi, *Angew. Chem. Int. Ed.* **36**, 1011

(1997).

- [10] T. Onda, S. Shibuuchi, N. Satoh, K. Tsujii, *Langmuir* **12**, 2125 (1996).
- [11] K. Tadanaga, N. Katata, T. Minami, *J. Am. Ceram. Soc.* **80**, 1040 (1997).
- [12] K. Tadanaga, N. Katata, T. Minami, *J. Am. Ceram. Soc.* **80**, 3213 (1997).
- [13] K. Tadanaga, *J. Ceram. Soc. Jpn.* **121**, 819 (2013).
- [14] I. Sas, R. E. Gorga, J. A. Joines, K. A. Thoney, *J. Poly. Sci. B* **50**, 824 (2012).
- [15] D. Zhang, L. Wang, H. Qian, X. Li, *J. Coat. Technol. Res.* **13**, 11 (2016).
- [16] H. Sojoudi, M. Wang, N. D. Boscher, G. H. McKinley, K. K. Gleason, *Soft Matter* **12**, 1938 (2016).
- [17] G. Wang, S. Liu, S. Wei, Y. Liu, J. Lian, Q. Jiang, *Sci. Rep.* **6**, 20933 (2016).
- [18] A. W. Adamson, A. P. Gast, "Physical Chemistry of Surfaces", John Wiley & Sons, Inc. 368 (1997).
- [19] A. Tuteja, W. Choi, M. L. Ma, J. M. Mabry, S. A. Mazzella, G. C. Rutledge, G. H. McKinley, R. E. Cohen, *Science* **318**, 1618 (2007).
- [20] A. Tuteja, W. Choi, J. M. Mabry, G. H. McKinley, R. E. Cohen, *Proc. Natl. Acad. Sci. U.S.A.* **105**, 18200 (2008).
- [21] K. Kurogi, H. Yan, K. Tsujii, *Colloids Surf. A* **317**, 592 (2008).
- [22] H. Zhao, K. Park, K. Law, *Langmuir* **28**, 14925 (2012).
- [23] W. Post, *I.R.E. Trans. Comp. Parts* **9**, 53 (1962).
- [24] S. Ono, Doctoral thesis at Graduate School of Engineering, Hokkaido Univ. (2012).
- [25] T. Fujii, Doctoral thesis at Graduate School of Engineering, Hokkaido Univ. (2012).
- [26] D. Wang, L. Zhang, W. Lee, M. Knez, L. Liu, *Small* **9**, 1025 (2013).

- [27] F. Brown, W. D. Mackintosh, *J. Electrochem. Soc.* **120**, 1096 (1973).
- [28] J. P. S. Pringle, *J. Electrochem. Soc.* **120**, 398 (1973).
- [29] J. P. S. Pringle, *Electrochim. Acta* **25**, 1423 (1980).
- [30] K. Khalil, A. Bowen, J. S. L. Leach, *Electrochim. Acta* **33**, 1721 (1988).
- [31] A. Di Paola, F. D. Quarto, C. Sunseri, *Corros. Sci.* **20**, 1067 (1980).
- [32] A. G. Gad-Allah, H. A. A. El-Rahman, *J. Appl. Electrochem.* **17**, 1065 (1987).
- [33] R. G. Keil, R. E. Salomon, *J. Electrochem. Soc.* **115**, 628 (1968).
- [34] M. Metikos-Hukovic, *J. Electrochim. Acta* **26**, 989 (1981).
- [35] C. Ortega, J. Siejka, *J. Electrochem. Soc.* **129**, 1905 (1982).
- [36] H. A. A. El-Rahman, M. M. Abou-Romia, *J. Appl. Electrochem.* **20**, 39 (1990).
- [37] K. Shahzad, Doctoral thesis at Graduate School of Chemical Sciences and Engineering, Hokkaido Univ. (2016).
- [38] H. Habazaki, Y. Konno, Y. Aoki, P. Skeldon, G. E. Thompson, *J. Phys. Chem. C* **114**, 18853 (2010).
- [39] Y. Konno, E. Tsuji, P. Skeldon, G. E. Thompson, H. Habazaki, *J. Solid State Electrochem.* **16**, 3887 (2012).
- [40] Y. Konno, S. Yang, E. Tsuji, Y. Aoki, P. Skeldon, G. E. Thompson, H. Habazaki, *ECS Trans.* **50**, 183 (2013).
- [41] K. Shahzad, E. Tsuji, Y. Aoki, H. Habazaki, *Electrochim. Acta.* **151**, 363 (2015).
- [42] H. Habazaki, K. Shahzad, T. Hiraga, E. Tsuji, Y. Aoki, *ECS Trans.* **69**, 211 (2015).
- [43] J. W. Diggie, T. C. Downie, C. W. Goulding, *Chem. Rev.* **69**, 365 (1969).
- [44] W. Lee, S. Park, *Chem. Rev.* **114**, 7487 (2014).

- [45] H. Masuda, F. Hasegawa, S. Ono, *J. Electrochem. Soc.* **144**, L127 (1997).
- [46] A. P. Li, F. Müller, A. Birner, K. Nielsch, U. Gösele, *J. Appl. Phys.* **84**, 6023 (1998).
- [47] H. Masuda, K. Fukuda, *Science* **268**, 1466 (1995).
- [48] F. Li, L. Zhang, R. M. Metzger, *Chem. Mater.* **10**, 2470 (1998).
- [49] H. Masuda, K. Yada, A. Osaka, *Jpn. J. Appl. Phys.* **37**, L1340 (1998).
- [50] K. Nielsch, J. Choi, K. Schwirn, R. B. Wehrspohn, U. Gösele, *Nano Lett.* **2**, 677 (2002).
- [51] J. P. S. Pringle, *J. Electrochem. Soc.* **120**, 398 (1973).
- [52] J. P. S. Pringle, *Electrochim. Acta* **25**, 1423 (1980).
- [53] G. C. Wood, P. Skeldon, G. E. Thompson, K. Skeldon, *J. Electrochem. Soc.* **143**, 74 (1996).
- [54] P. Skeldon, K. Shimizu, G. E. Thompson, G. C. Wood, *Thin Solid Films* **123**, 127 (1985).
- [55] H. Habazaki, K. Shimizu, P. Skeldon, G. E. Thompson, G. C. Wood, *J. Surf. Finish. Soc. Jpn.* **19**, 772 (1998).
- [56] R. Beranek, H. Hildebrand, P. Schmuki, *Electrochem. Solid-State Lett.* **6**, B12 (2003).
- [57] S. Ono, M. Saito, M. Ishiguro, H. Asoh, *J. Electrochem. Soc.* **151**, B473 (2004).
- [58] Y. Katsuta, A. Yasumori, K. Wada, K. Kurashia, S. Suehara, S. Inoue, *J. Non-Cryst. Solids* **354**, 451 (2008).
- [59] T. Kikuchi, T. Yamamoto, R. O. Suzuki, *Appl. Surf. Sci.* **284**, 907 (2013).
- [60] S. Ono, M. Saito, H. Asoh, *Electrochim. Acta* **51**, 827 (2005).
- [61] J. Ren, Y. Zuo, *Appl. Surf. Sci.* **261**, 193 (2012).

- [62] T. Kikuchi, O. Nishinaga, S. Natsui, R. O. Suzuki, *Electrochim. Acta* **156**, 235 (2015).
- [63] G. E. Thompson, G. C. Wood, R. Hutchings, *Trans. IMF* **58**, 21 (2003).
- [64] A. Pakes, G. E. Thompson, P. Skeldon, P. C. Morgan, K. Shimizu, *Trans. IMF* **77**, 171 (1999).
- [65] F. Keller, M. S. Hunter, D. L. Robinson, *J. Electrochem. Soc.* **100**, 411 (1953).
- [66] S. Ono, *J. Surf. Sci. Jpn.* **19**, 790 (1998).
- [67] S. Z. Chu, K. Wada, S. Inoue, M. Isogai, Y. Katsuta, A. Yasumori, *J. Electrochem. Soc.* **153**, B384 (2006).
- [68] O. Nishinaga, T. Kikuchi, S. Natsui, R. O. Suzuki, *Sci. Rep.* **3**, 2748 (2013).
- [69] T. Fujii, Y. Aoki, H. Habazaki, *Langmuir* **27**, 11752 (2011).
- [70] T. Fujii, H. Sato, E. Tsuji, Y. Aoki, H. Habazaki, *J. Phys. Chem. C* **116**, 23308 (2012).
- [71] W. A. Zisman, *Ind. Eng. Chem.* **57**, 25 (1965).
- [72] A. Ulman, *Chem. Rev.* **96**, 1553 (1996).
- [73] A. Hozumi, Y. Yokogawa, T. Kameyama, H. Sugimura, K. Hayashi, H. Shirayama, O. Takai, *J. Vac. Sci. Technol. A* **19**, 1812 (2001).
- [74] A. Hozumi, H. Taoda, T. Saito, N. Shirahata, *J. NanoSci. Nanotechnol.* **9**, 455 (2009).
- [75] A. Hozumi, K. Ushiyama, H. Sugimura, O. Takai, *Langmuir* **15**, 7600 (1999).
- [76] H. Sugimura, K. Ushiyama, A. Hozumi, O. Takai, *Langmuir* **16**, 885 (2000).
- [77] J. C. Love, L. A. Estroff, J. K. Kriebel, R. G. Nuzzo, G. M. Whitesides, *Chem. Rev.* **105**, 1107 (2005).
- [78] J. A. DeRose, E. Hoque, B. Bhushan, H. J. Mathieu, *Surf. Sci.* **602**, 1360 (2008).
- [79] M. J. Pellerite, T. D. Dunbar, L. D. Boardman, E. J. Wood, *J. Phys. Chem. B* **107**,

11726 (2003).

[80] A. Hozumi, K. Bokyoung, T. J. McCarthy, *Langmuir* **25**, 6834 (2009).

[81] H. Habazaki, H. Sato, E. Tsuji, Y. Aoki, K. Shimizu, *ECS Trans.* **58**, 75 (2014).

[82] H. Sato, T. Fujii, E. Tsuji, Y. Aoki, K. Shimizu, P. Skeldon, G. E. Thompson, H. Habazaki, *Surf. Interface Anal.* **45**, 1441 (2013).

[83] G. Azimi, R. Dhiman, H. Kwon, A. T. Paxson, K. K. Varanasi, *Nat. Mater.* **12**, 315 (2013).

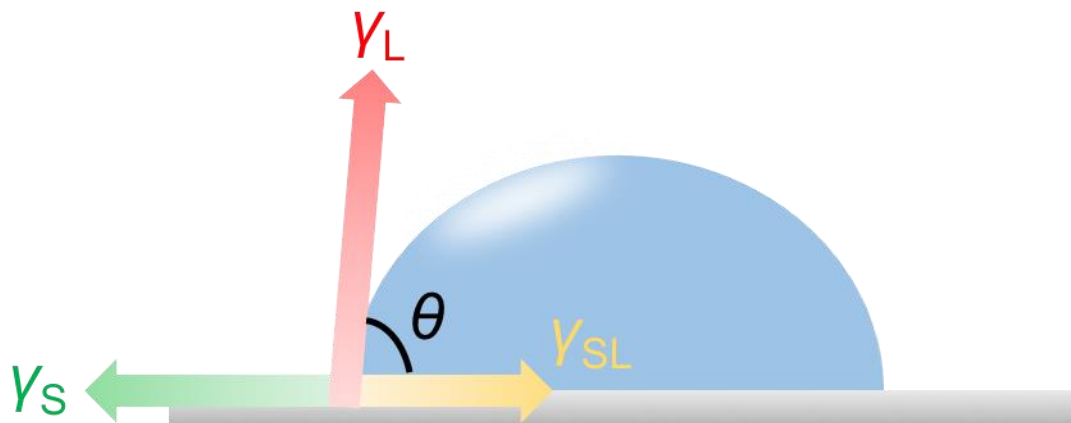


Figure 1.1 Schematic illustration showing the correlation between the contact angle of liquid on a flat surface and three interface tensions.

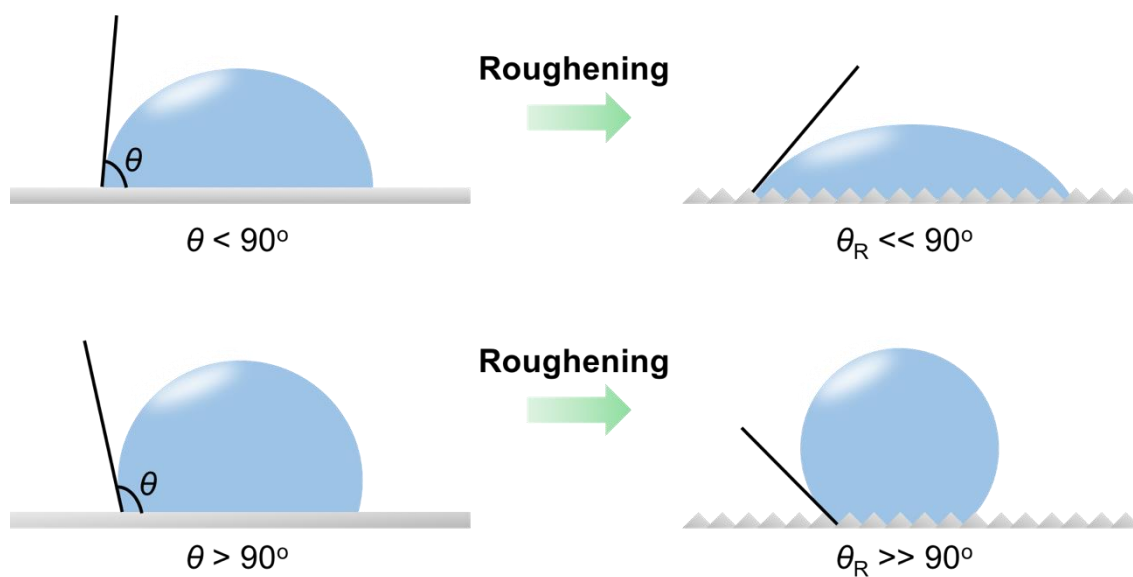


Figure 1.2 Schematic illustrations for changes in the wettability by introduction of surface roughness in Wenzel state.

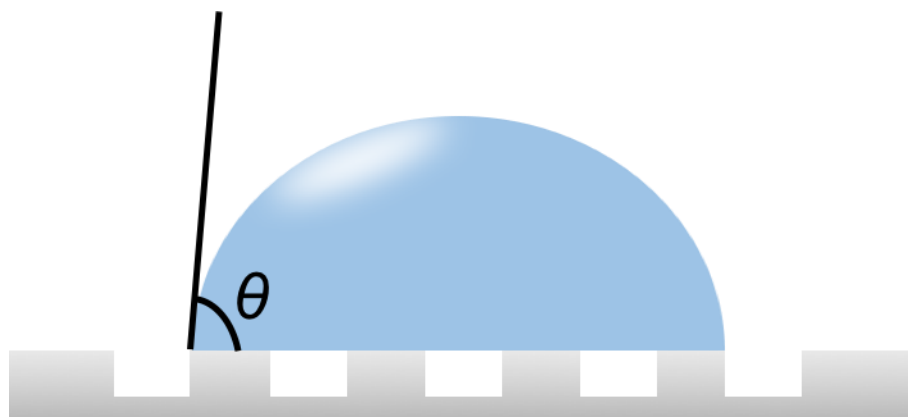


Figure 1.3 Schematic illustration for a liquid droplet on the rough surface in Cassie-Baxter state.

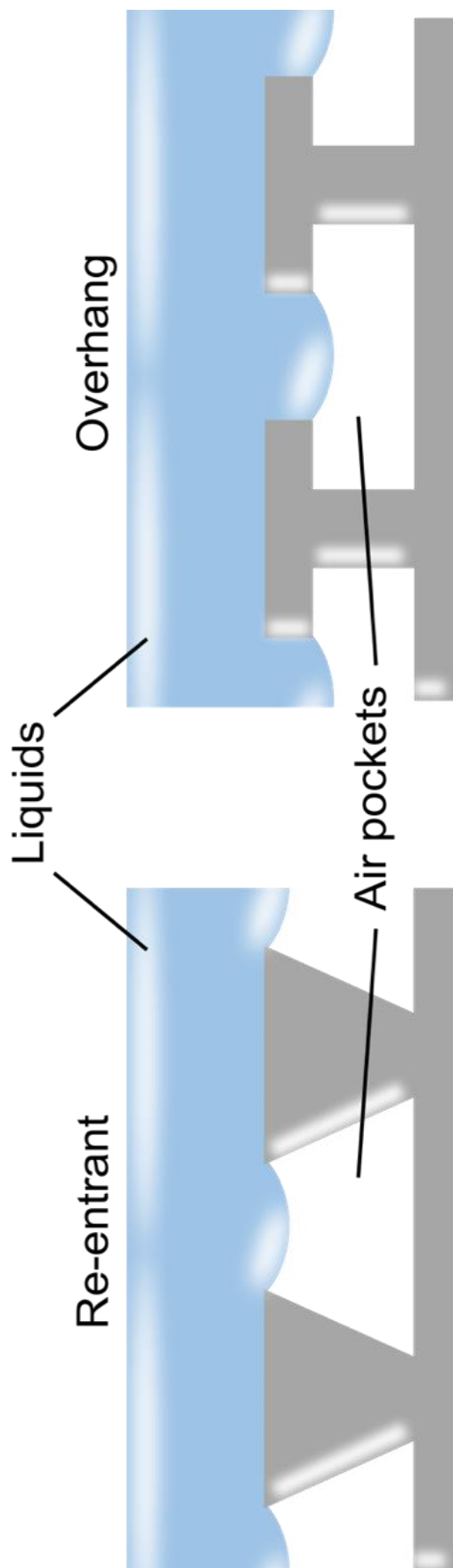


Figure 1.4 Schematic illustration of re-entrant and overhang morphological structures preventing the penetration of oil liquids by developing the sagging liquid-air interfaces.

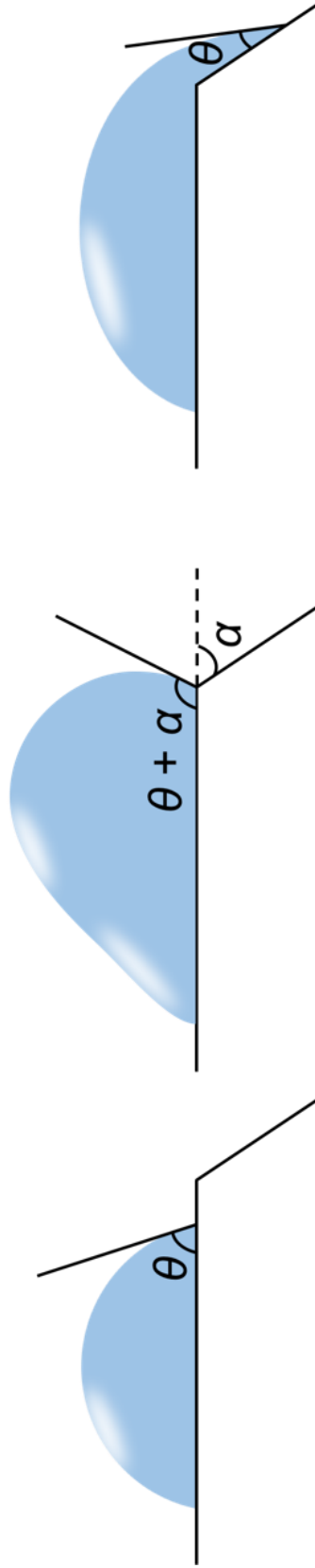


Figure 1.5 Schematic illustration of the pinning effect for a liquid droplet [17].

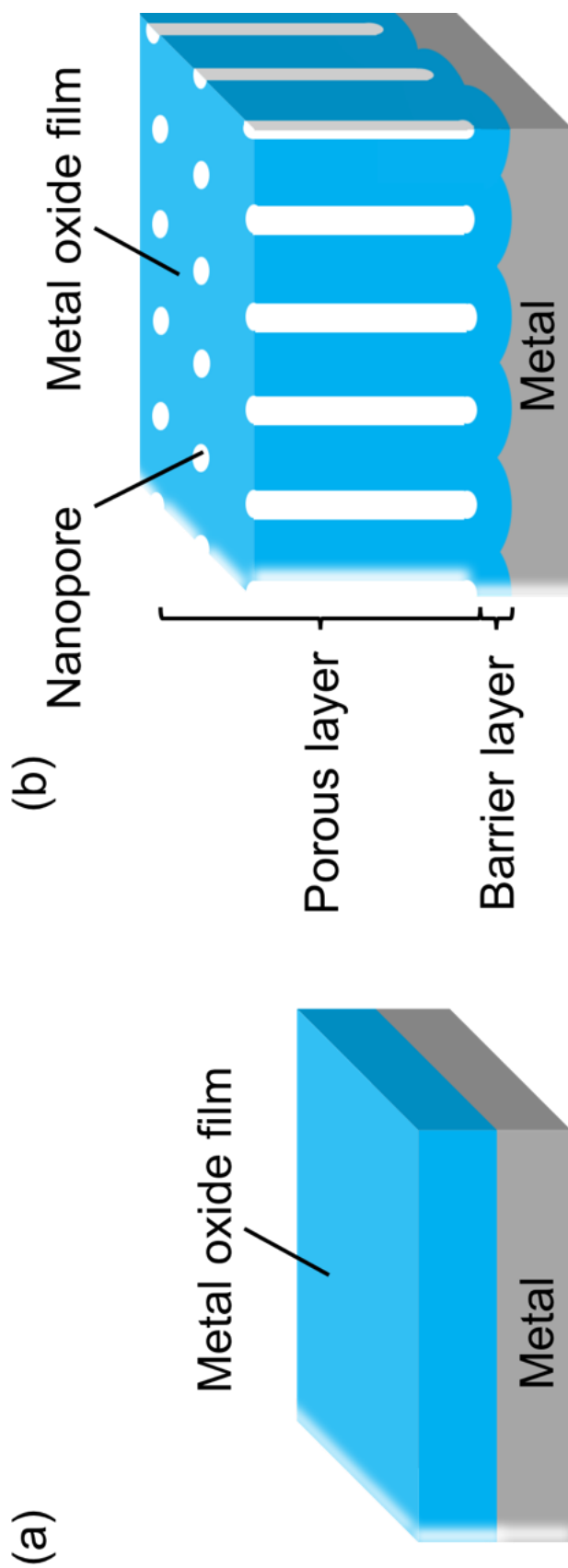


Figure 1.6 Schematic illustrations of (a) barrier and (b) porous anodized film.

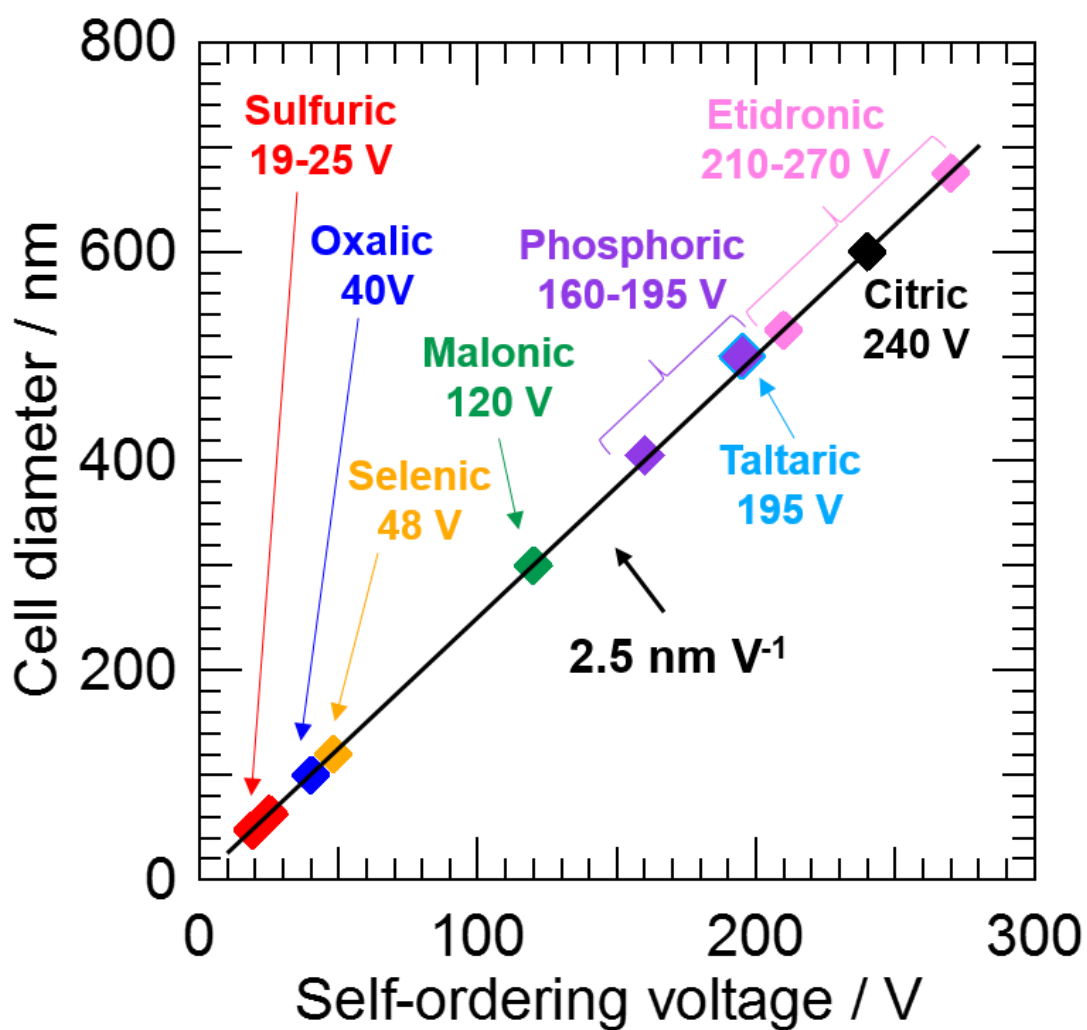


Figure 1.7 Self-ordering regimes in typical and hard anodizing by using sulfuric (red symbol) [45, 46], oxalic (blue symbol) [46-48], selenic (yellow symbol) [68], malonic (green symbol) [61], phosphoric (purple symbol) [49, 50], tartaric (sky-blue symbol) [60], citric (black symbol) [57, 58], and etidronic acid (pink symbol) [62].

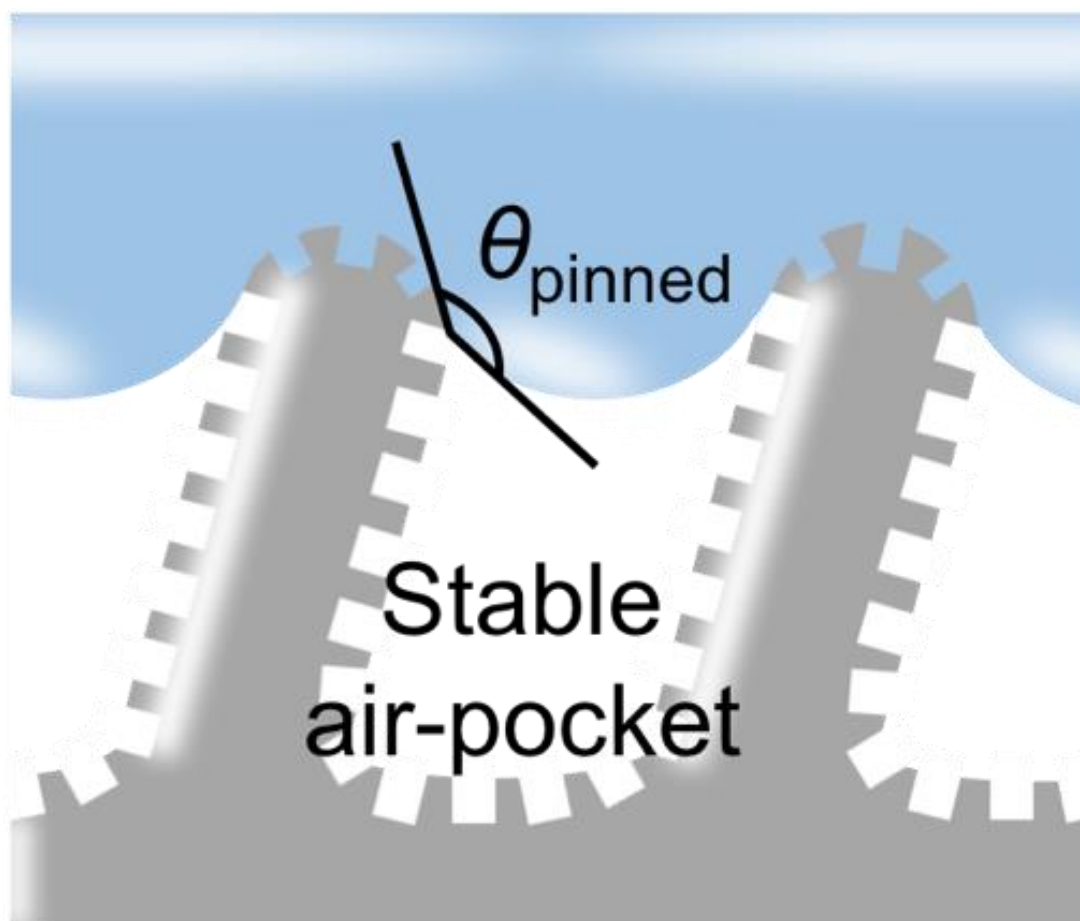


Figure 1.8 Schematic illustration showing the pinning effect for liquids on the submicropillar/nanopore hierarchical structure. (a) Liquids can penetrate into gaps without nanopores, (b) while be pinned close to surface with sufficient nanopores (c) [26, 57].

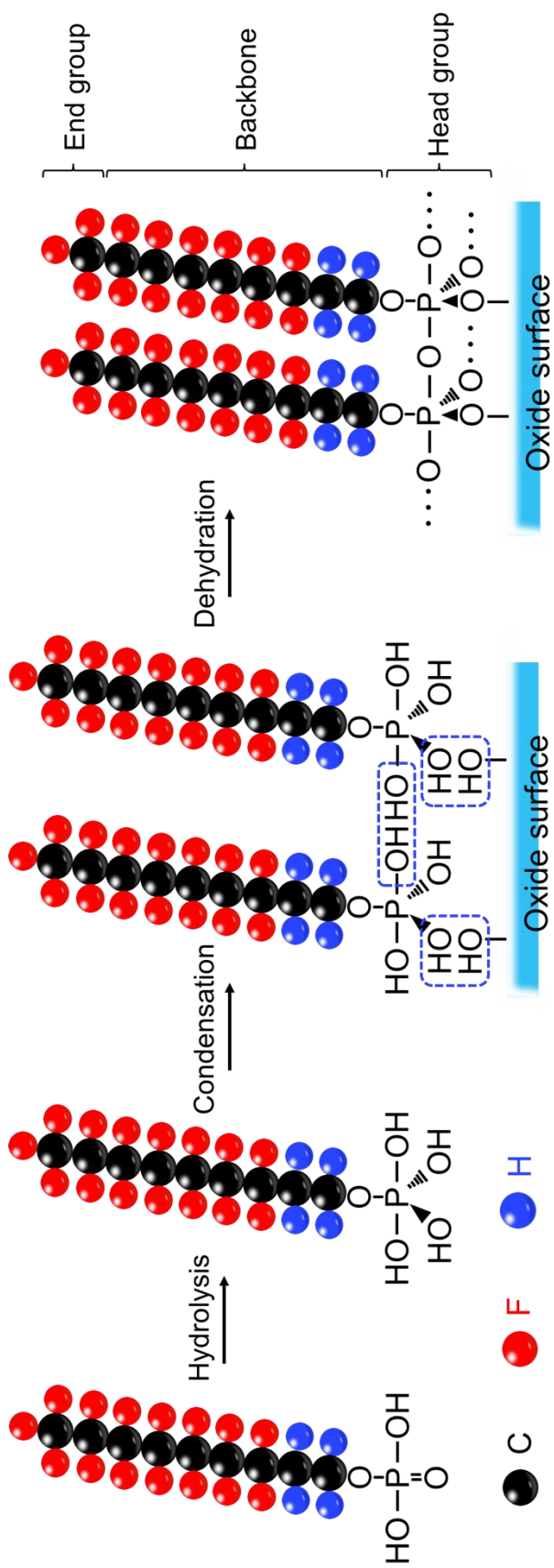


Figure 1.9 Schematic illustrations showing formation process of self-assembled monolayers (SAM) with fluoroalkylphosphoric acid [26].

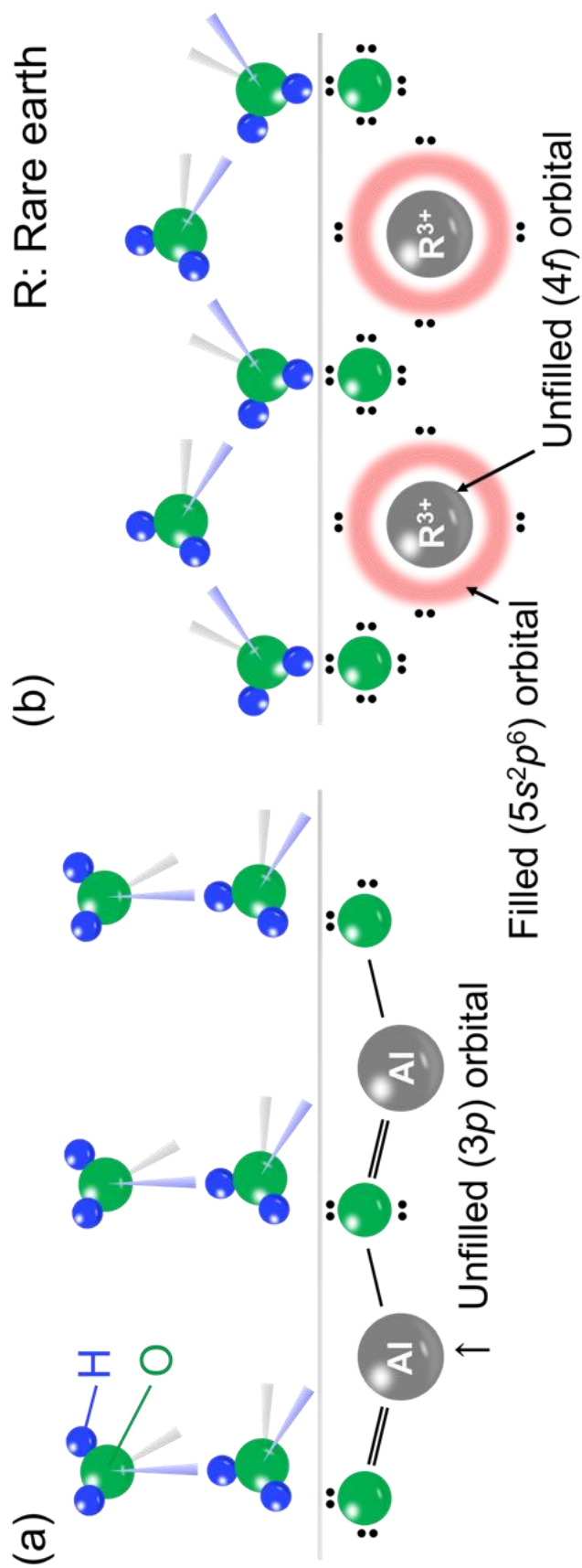


Figure 1.10 Schematic of the orientation of water molecules next to an (a) alumina and (b) REOs surface (surface and water molecules not to scale).

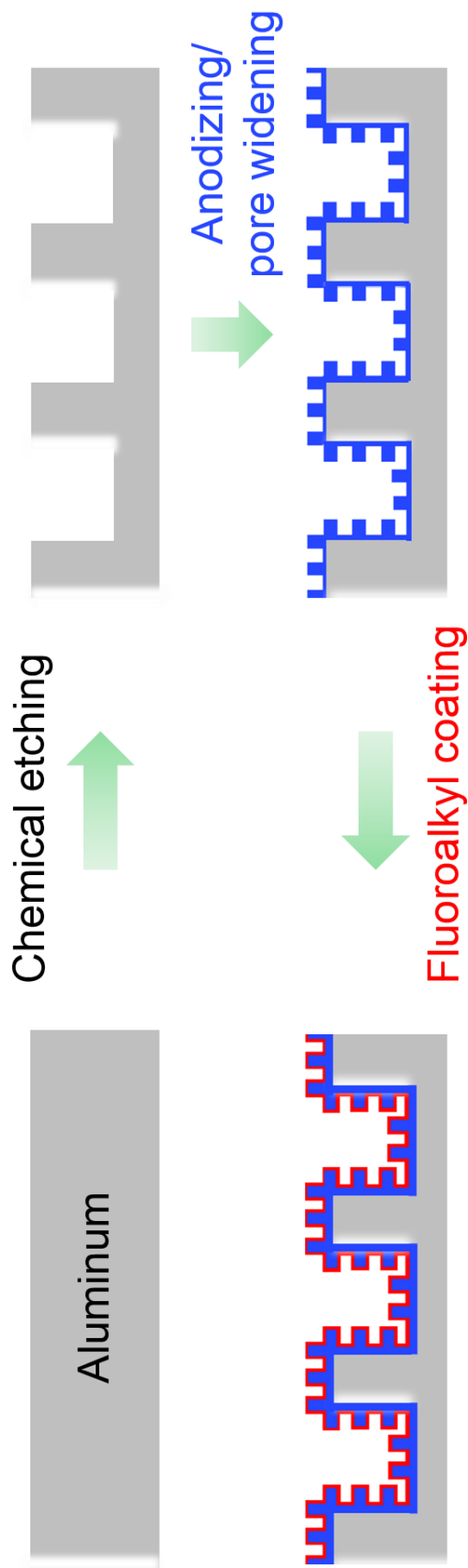


Figure 1.11 Schematic illustration drawing the process for preparation of superoleophobic aluminum surface.

Chapter 2

***Control of Surface Morphological
Structure on Aluminum Substrates
by Multi-Step Wet Process***

2.1 Introduction

Hierarchical surface geometry on solid materials is of crucial importance to fabricate the superhydrophobic and superoleophobic surfaces. As described in Chapter 1, recent studies have demonstrated that a re-entrant surface geometry including a micro/nano hierarchical structure is effective in obtaining superoleophobic surfaces [1-5]. Such geometry is particularly useful for super-repellency to low-surface-tension liquids [6]. Fujii et al. reported that in dual-pillar or submicrometer-pillar/nanopore hierarchical surfaces, the gap distance among submicrometer-pillars and nanopore porosity are the most important factors [3-5]. However, these geometries were fabricated by dry processes such as lithography or magnetron sputtering methods, and these methods are not suitable for practical application for the cost-effective industrial production of superhydrophobic and superoleophobic surfaces. For the industrial large scale production, we must use a simple and efficient method, such as wet process. Wet process is the simplest and most efficient method in industries. In particular, anodizing of aluminum is one of the promising processes to introduce geometrically controlled surfaces. Zhou et al. reported the formation of alumina nanowires on the faceted aluminum surface by two-step anodizing. After fluoroalkylsilane coating, the surface showed the superoleophobicity for a range of liquids including silicone oil with 22 mN m^{-1} [7]. Habazaki et al. fabricated a submicro/nano-hierarchical morphology on aluminum surface by anodizing of the scalloped aluminum surface, which was also prepared by anodizing and film dissolution. The surface showed super-repellency for rapeseed oil [8].

In this chapter, the author discusses the fabrication of hierarchical dual- or triple-

pore surface geometries on aluminum metal plate or mesh using a combination of practical and cost-effective surface finishing methods, i.e., chemical etching, anodizing, and pore widening. Particular attention has been paid to understand the relationship between morphology and the condition of each process to control the surface geometry.

2.2 Experimental

High-purity (99.99%) aluminum sheets, 0.5 mm thick, or meshes with 100 openings per inch (the size of openings is 150 μm) were used. After pre-treating the aluminum sheets in 1 mol dm⁻³ NaOH solutions at 333 K for 120 s and subsequently in 1 mol dm⁻³ HNO₃ at 333 K for 180 s, chemical etching was carried out by immersion in a mixture of 0.2 mol dm⁻³ CuCl₂ and several concentrations (1 to 6 mol dm⁻³) of HCl at 298 K for a suitable time. For aluminum meshes, pre-treatment was not taken place and etching time was shorter than that for sheets to avoid excess dissolution in NaOH or etchant. After chemical etching, specimen was rinsed with concentrated HNO₃ to remove the copper deposited on the surfaces. Nanoporous anodic alumina layers were formed by anodizing the chemically etched aluminum at 25 V in 0.3 mol dm⁻³ H₂SO₄ aqueous electrolyte at 288 K for 180 s to grow approximately 360 nm thick nanoporous oxide layer on the entire surface. The size of the nanopores in the anodic alumina layer was controlled by the subsequent pore widening treatment in 5 wt% H₃PO₄ at 303 K for suitable time (Fig. 2.1). Then, the surface morphology of the specimens was observed using a field emission scanning electron microscope (SEM, JEOL Co. JSM-6500F).

2.3 Results and discussion

2.3.1 Surface roughening by chemical etching on aluminum sheets

Numbers of micrometer or submicrometer pits can be introduced on aluminum surface by electrochemical and chemical etching. DC etching of aluminum in HCl solutions at elevated temperatures develops tunnel pits of several tens μm length and ~ 1 μm width [9-12]. In contrast, AC etching in the similar HCl solutions produces a rough etched layer comprising inter-connected cubic pits [13-16]. The size of the cubic pits is usually submicrometers. In this study, more simple chemical etching has been used [17]. Fig. 2.2 shows scanning electron micrographs of the aluminum sheet surfaces after chemical etching in the solutions containing $0.2 \text{ mol dm}^{-3} \text{ CuCl}_2$ and several concentrations of HCl. At all HCl concentrations, pits developed over the entire surface with clear observable cubic shapes. The time required to form pits over the entire surface was dependent upon the HCl concentration; longer time was needed at the lower HCl concentrations because of reduced pit nucleation rates. The cubic pit size tends to decrease with an increase in the HCl concentration, from several micrometers at $1 \text{ mol dm}^{-3} \text{ HCl}$ (Fig. 2.2a) to the submicrometer range at $6 \text{ mol dm}^{-3} \text{ HCl}$ (Fig. 2.2d). At higher HCl concentrations, higher density of small pits are developed. In electrochemical DC etching of aluminum in HCl solutions, tunnel pits are formed on aluminum, and it is reported that the growth of tunnel pits is terminated when the aluminum chloride is saturated at the tip of the tunnel pits [12]. The formation of smaller pits at higher HCl concentrations in this study is probably associated with the faster saturation in the pits by increasing HCl concentration.

2.3.2 Formation of hierarchically rough aluminum plate

In order to introduce nanoscale pores on the entire etched surface, the etched specimens were anodized. As described in Chapter 1, anodizing of aluminum in acid electrolytes, including sulfuric acid, oxalic acid and phosphoric acid, results in the formation of nanoporous oxide films with self-organized cylindrical pore channels [18-21]. The size of pores and the interpore distance are controlled by anodizing voltage and the electrolyte composition [20-25]. In this study, the etched aluminum was anodized at 25 V in 0.3 mol dm⁻³ sulfuric acid, at which relatively small pores were developed. Fig. 2.3a shows SEM images after anodizing for 180 s. At the available resolution of SEM, nanopores distributed uniformly on the etched surface are visible after pore widening for longer than 600 s in H₃PO₄ solution, as shown in Figs. 2.3b-d. The nanopore size proportionally increases with the duration of the pore-widening treatment, from approximately 12 nm at 600 s to 45 nm at 1200 s. According to a plot shown in Fig. 2.4, nanopores slowly expanded with an approximate rate of 2.3 nm min⁻¹. Thus, the nanopore diameter can readily be controlled by this method without complete-dissolution of porous film. The porosity also increases from 14 to 33% by an increase in the pore widening time from 600 to 1200 s. During anodizing and pore widening, the micrometer-scale roughness, developed by chemical etching, was maintained and simply nanopore structure was introduced, such that dual scale micrometer-nanopore rough surfaces were successfully developed by these practical wet processes.

2.3.3 Formation of triple-pore hierarchically rough aluminum mesh

According to Onda and Tsujii, a fractal structure is efficient for superhydrophobicity or superoleophobicity [26]. Thus, it is expected that the surface with multi-pore hierarchical structure of a fractal-like geometry shows higher liquid repellency. The author tried to fabricate a triple-pore hierarchical morphology using aluminum mesh. Fig. 2.5a shows the scanning electron micrograph of the aluminum mesh used in this study. The mesh consists of aluminum wire 100 μm in diameter and the mesh opening is ~ 150 μm . The surface of the aluminum wire is smooth, but after chemical etching in an aqueous solution containing 1 mol dm^{-3} HCl and 0.2 mol dm^{-3} CuCl_2 , the wire surface became rough, as shown in Fig. 2.5b. The surface roughening occurred through the development of a number of cubic pits on the entire wide surface (Fig. 2.5c). The size of the pits was 1-3 μm , which changed with the HCl concentration, as discussed above. When the etched specimens were further anodized at 25 V in a 0.3 mol dm^{-3} sulfuric acid aqueous electrolyte and then immersed in a 5 wt% H_3PO_4 solution for 900 s at 303 K, an oxide film with nanopores ~ 30 nm in diameter was formed uniformly on the etched surface (Fig. 2.5d). The oxide film formed by anodizing had cylindrical pore channels, which were developed normal to the metal surface. Thus, a triple-scale porous surface, consisting of ~ 100 μm mesh openings, ~ 1 μm etch pits, and ~ 30 nm nanopores, was obtained by a combination of simple chemical and electrochemical treatments of aluminum mesh.

Similar to aluminum plate, the size of the etch pits formed by chemical etching was controlled by the HCl concentration in the etching solution as well as aluminum sheet specimen. Fig. 2.6 shows the SEM micrographs of the aluminum mesh with microscale

etch pits and nanopores. The size of the microscale etch pits changed with the HCl concentration. Obviously, the size of the etch pits decreased with an increase in the HCl concentration from 1-3 μm at 1 mol dm^{-3} HCl to $\sim 0.2 \mu\text{m}$ at 6 mol dm^{-3} HCl. There are no difference of the size of the etch pits in each solution for both aluminum plate and mesh. Anodizing and pore widening form the nanopores $\sim 30 \text{ nm}$ in diameter uniformly regardless of the etch pit size. Thus, the aluminum surfaces with triple-pore hierarchical morphologies with different micrometer etch pits were obtained successfully.

2.4 Conclusions

In this chapter, rough surfaces with dual- or triple-scale hierarchically porous geometries are formed on aluminum sheet or mesh surfaces by a combination of practical wet processes: chemical etching in a mixed solution of HCl and CuCl_2 , anodizing in sulfuric acid electrolyte, and pore widening in H_3PO_4 aqueous solution. The sizes of etch pits and nanopores are controlled by the HCl concentration in etching solution and the immersion time in H_3PO_4 solution after anodizing, respectively. The size of etch pits is controlled from \sim a few μm to submicrometer and the diameter of nanopores from 0 to $\sim 45 \text{ nm}$. In this manner, just a combination of practical wet process is useful to form hierarchically rough aluminum surfaces with controlled sizes of pits and nanopores. The developed hierarchical geometries are schematically shown in Fig. 2.7.

References

- [1] A. Tuteja, W. Choi, M. L. Ma, J. M. Mabry, S. A. Mazzella, G. C. Rutledge, G. H. McKinley, R. E. Cohen, *Science* **318**, 1618 (2007).
- [2] A. Tuteja, W. Choi, J. M. Mabry, G. H. McKinley, R. E. Cohen, *Proc. Natl. Acad. Sci. U.S.A.* **105**, 18200 (2008).
- [3] T. Fujii, Y. Aoki, H. Habazaki, *Langmuir* **27**, 11752 (2011).
- [4] T. Fujii, H. Sato, E. Tsuji, Y. Aoki, H. Habazaki, *J. Phys. Chem. C* **116**, 23308 (2012).
- [5] T. Fujii, Doctoral thesis at Graduate School of Engineering, Hokkaido Univ. (2012).
- [6] K. Tsujii, T. Yamamoto, T. Onda, S. Shibuuchi, *Angew. Chem. Int. Ed.* **36**, 1011 (1997).
- [7] H. Zhou, H. Wang, H. Niu, A. Gestos, T. Lin, *Adv. Funct. Mater.* **23**, 1664 (2013).
- [8] H. Habazaki, T. Fujii, E. Tsuji, Y. Aoki, H. Habazaki, *ECS Trans.* **50**, 217 (2013).
- [9] S. Ono, T. Makino, R. S. Alwitt, *J. Electrochem. Soc.* **152**, B39 (2005).
- [10] N. Osawa, K. Fukuoka, *Corros. Sci.*, **42**, 585 (2000).
- [11] D. Goad, *J. Electrochem. Soc.* **144**, 1965 (1997).
- [12] K. Hebert, R. Alkire, *J. Electrochem. Soc.* **135**, 2146 (1988).
- [13] S. Ono, H. Habazaki, *Corros. Sci.* **51**, 2364 (2009).
- [14] K. H. Na, S. I. Pyun, *Corros. Sci.* **49**, 2663 (2007).
- [15] J. H. Seo, J. H. Ryu, D. N. Lee, *J. Electrochem. Soc.* **150**, B433 (2003).
- [16] C. K. Dyer, R. S. Alwitt, *J. Electrochem. Soc.* **128**, 300 (1981).
- [17] D. A. Wang, L. B. Zhang, W. Lee, M. Knez, L. F. Liu, *Small* **9**, 1025 (2013).
- [18] F. Keller, M. S. Hunter, D. L. Robinson, *J. Electrochem. Soc.* **100**, 411 (1953).

- [19] J. P. O'Sullivan, G. C. Wood, *Proc. R. Soc. London, A* **317**, 511 (1970).
- [20] H. Masuda, K. Fukuda, *Science* **268**, 1466 (1995).
- [21] G. E. Thompson, *Thin Solid Films* **297**, 192 (1997).
- [22] K. Ebihara, H. Takahashi, M. Nagayama, *J. Surf. Finish. Soc. Jpn.* **33**, 156 (1982).
- [23] K. Ebihara, H. Takahashi, M. Nagayama, *J. Surf. Finish. Soc. Jpn.* **34**, 548 (1983).
- [24] H. Masuda, F. Hasegawa, S. Ono, *J. Electrochem. Soc.* **144**, L127 (1997).
- [25] H. Masuda, K. Yada, A. Osaka, *Jpn. J. Appl. Phys.* **37**, L1340 (1998).
- [26] T. Onda, S. Shibuuchi, N. Satoh, K. Tsujii, *Langmuir* **12**, 2125 (1996).

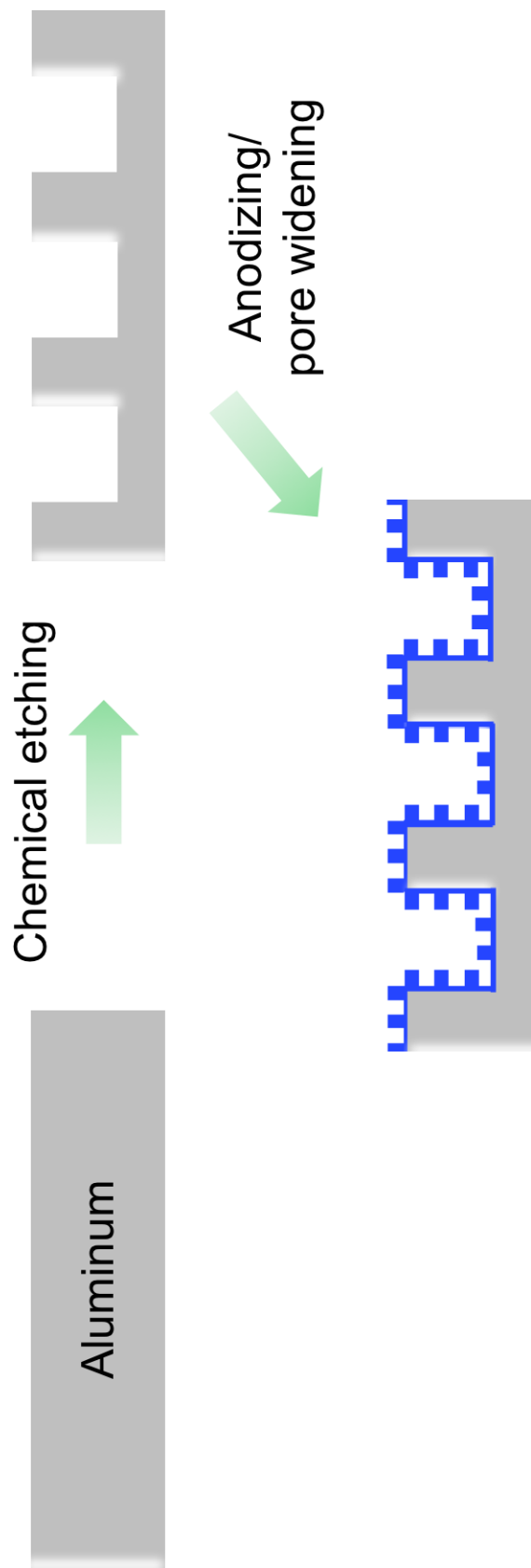


Figure 2.1 Schematic illustration showing the multi-step wet process in this study.

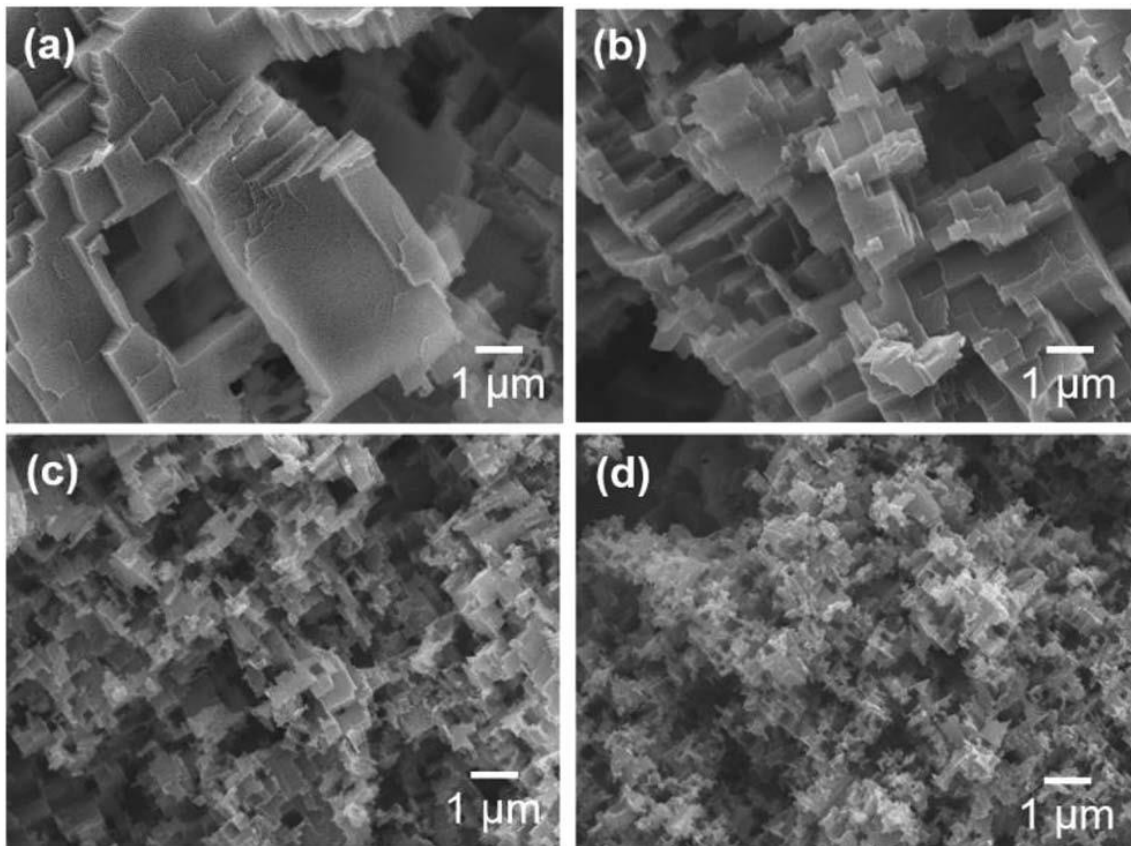


Figure 2.2 SEM images of the aluminum surfaces etched in solutions containing 0.2 mol dm⁻³ CuCl₂ and (a) 1, (b) 2, (c) 4, and (d) 6 mol dm⁻³ HCl for 360, 180, 40 and 20 s, respectively.

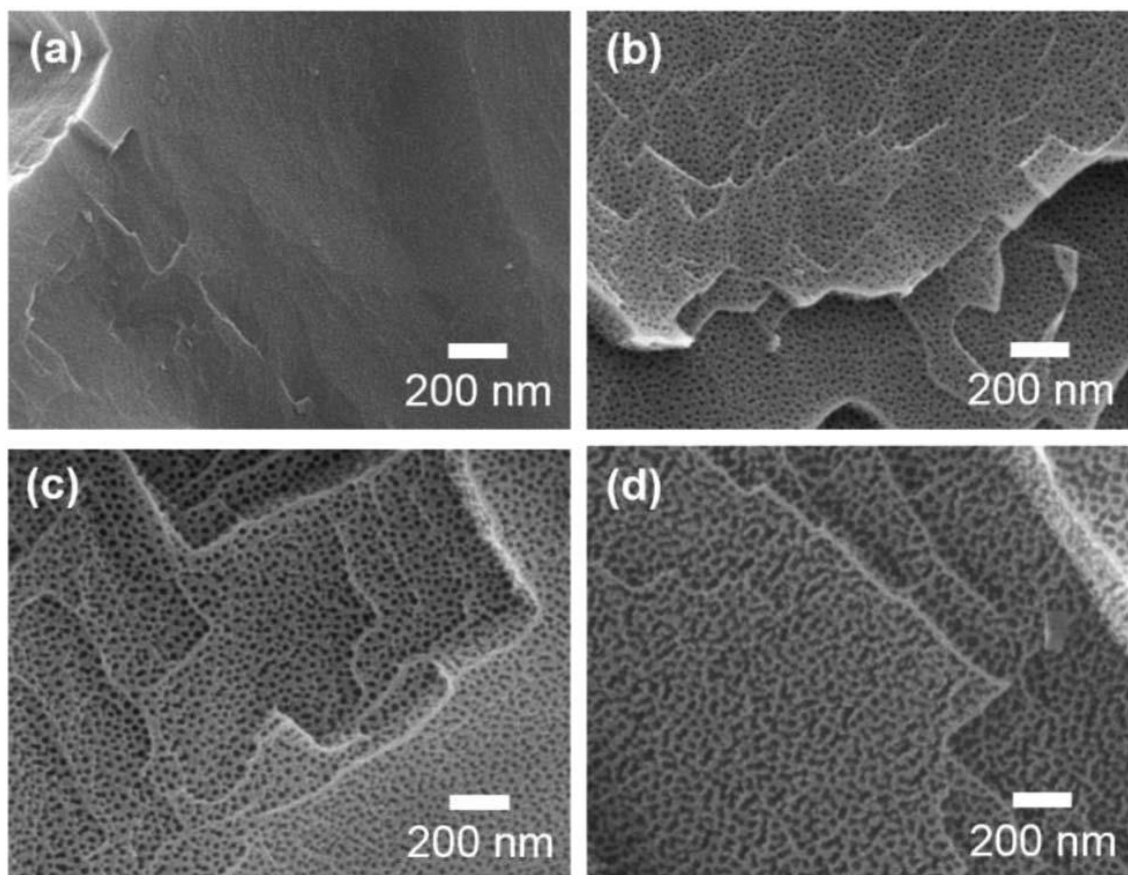


Figure 2.3 SEM images of the aluminum surfaces etched in solutions containing $0.2 \text{ mol dm}^{-3} \text{ CuCl}_2$ and $2 \text{ mol dm}^{-3} \text{ HCl}$; then anodized in $0.3 \text{ mol dm}^{-3} \text{ H}_2\text{SO}_4$ electrolyte at a constant voltage of 25 V for 180 s at 288 K; and finally immersed in 5 wt% H_3PO_4 for (a) 0, (b) 600, (c) 900, and (d) 1200 s.

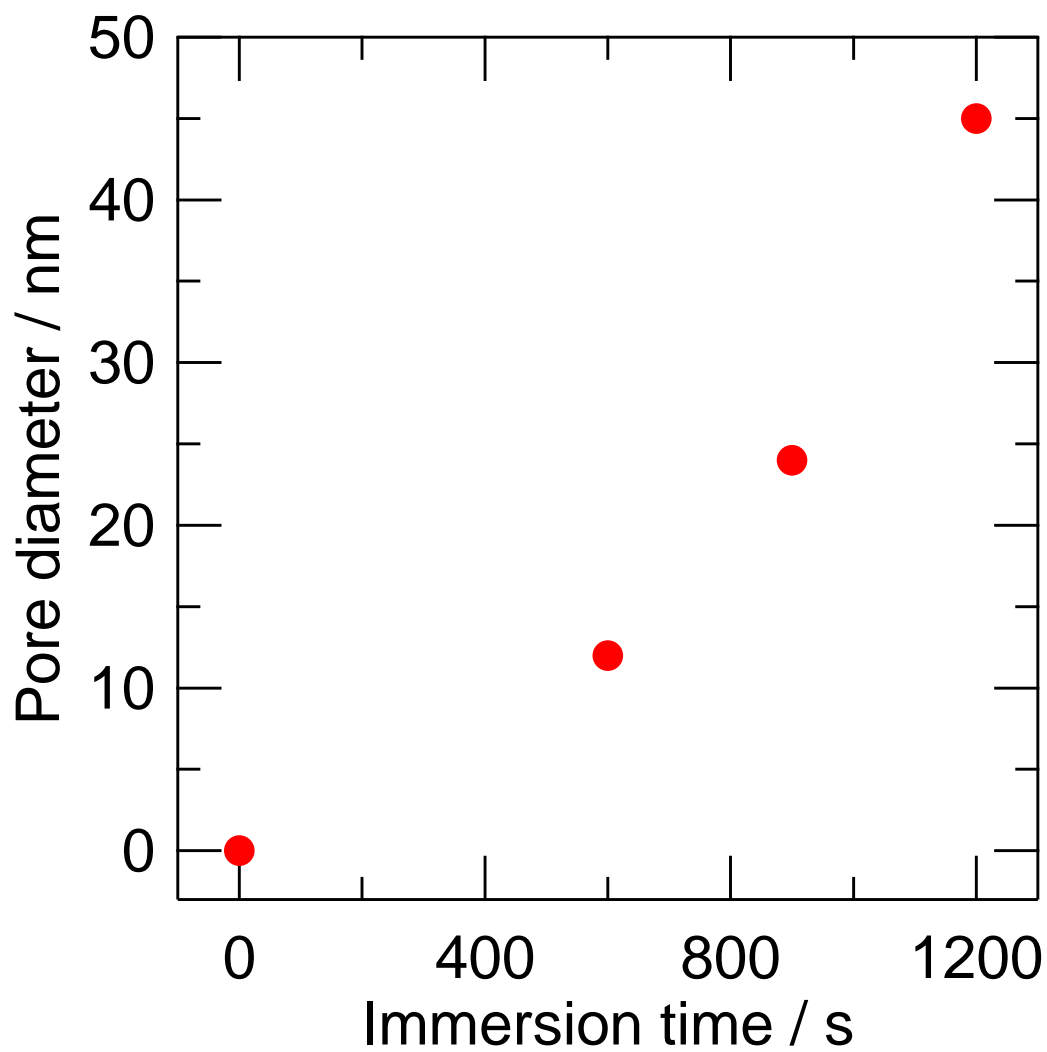


Figure 2.4 Plot of the change in nanopore diameters to immersion time in 5 wt% H_3PO_4 .

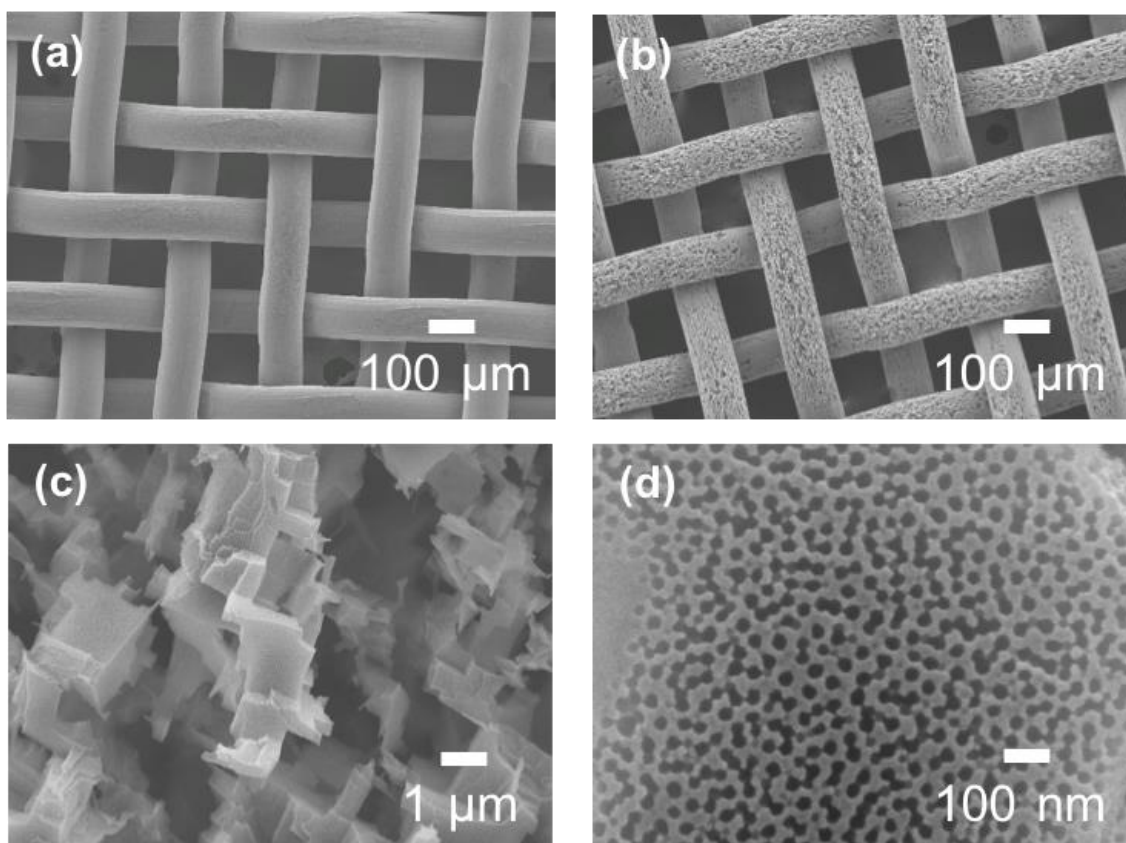


Figure 2.5 SEM images of aluminum mesh surfaces (a) as-received and (b-d) chemically etched in a solution containing $0.2 \text{ mol dm}^{-3} \text{ CuCl}_2$ and $1 \text{ mol dm}^{-3} \text{ HCl}$ for 60 s and then anodized at a constant voltage of 25 V in 0.3 mol dm^{-3} sulfuric acid for 180 s and pore-widened in 5 wt% H_3PO_4 solution for 900 s at 303 K.

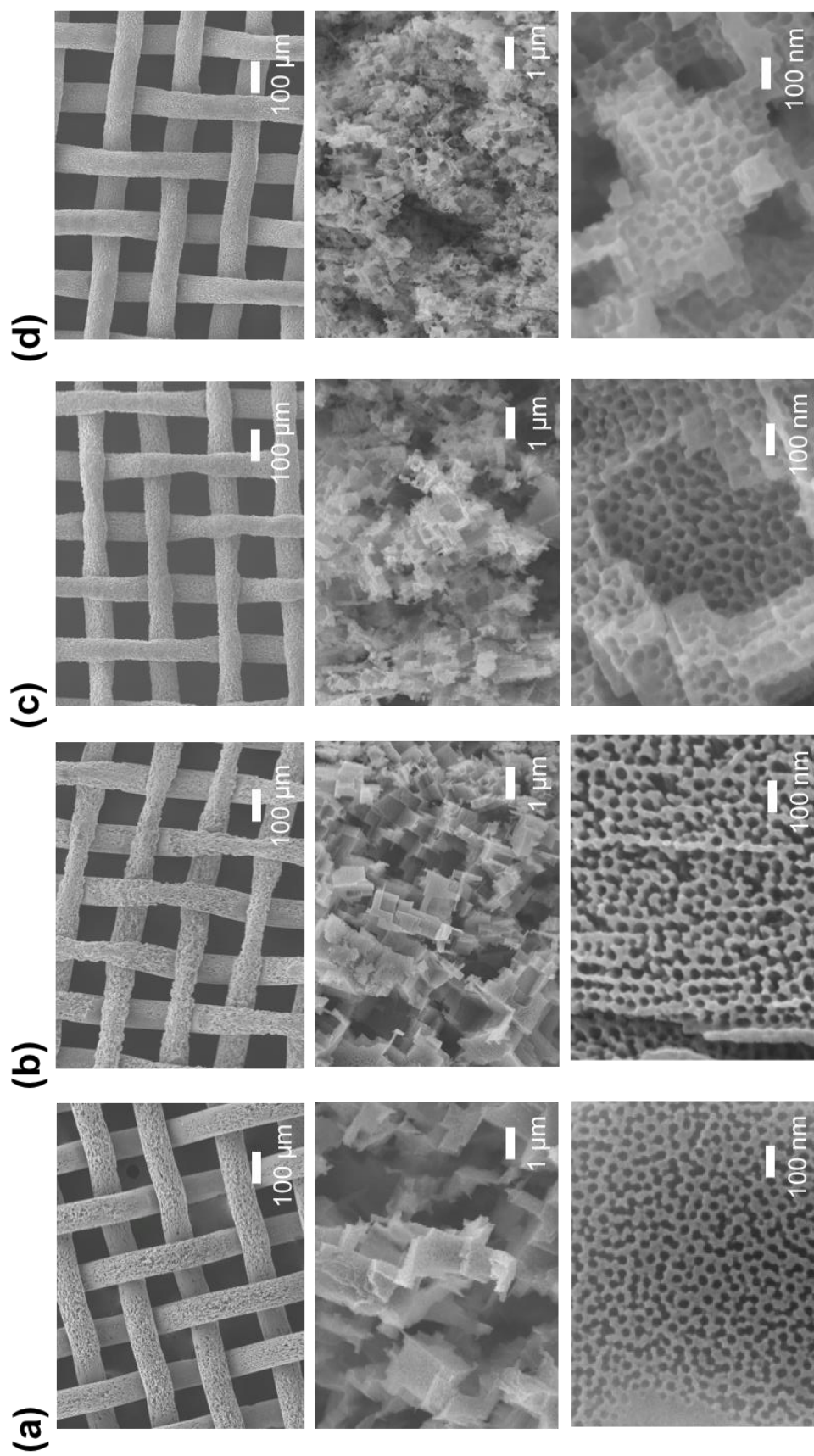


Figure 2.6 SEM images of aluminum mesh surfaces with micrometer etch pits and nanopores. The etch pits were formed in 0.2 mol dm^{-3} CuCl_2 and (a) 1, (b) 2, (c) 4, and (d) 6 mol dm^{-3} HCl solutions.

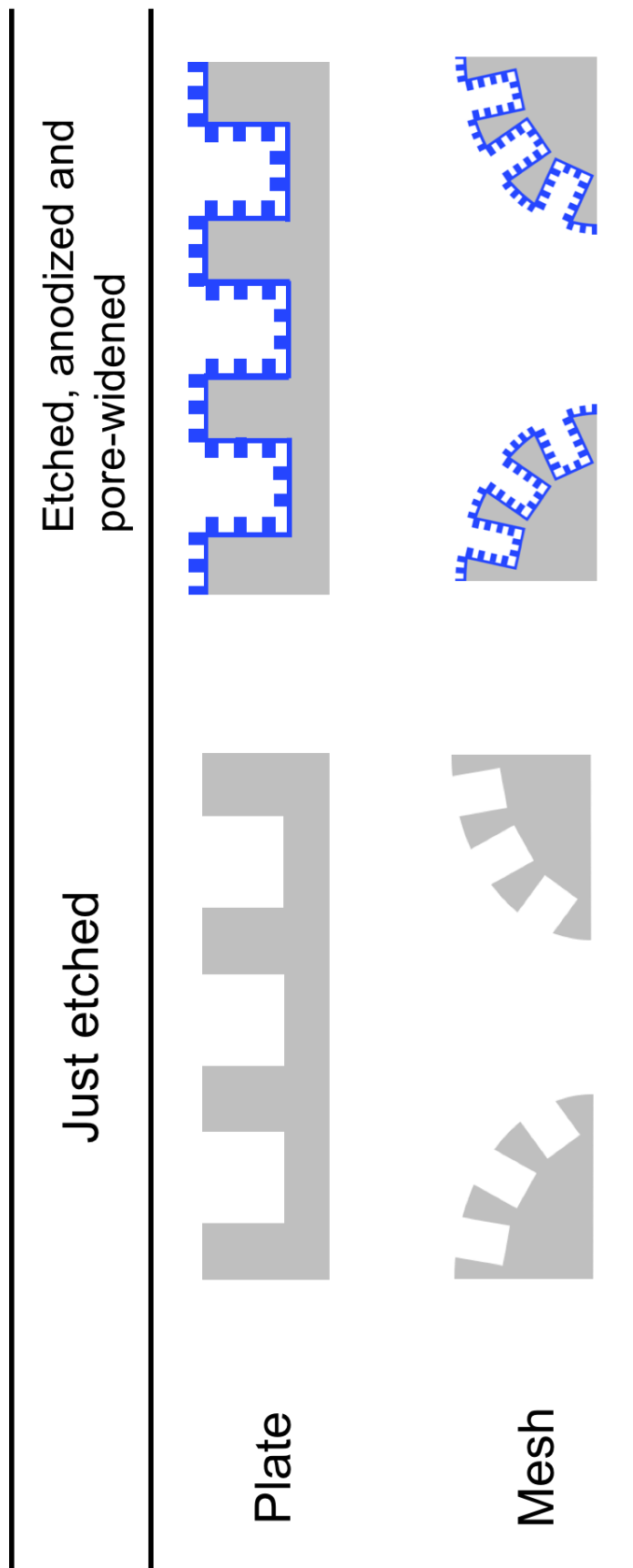


Figure 2.7 Schematic illustrations drawing several morphologies fabricated on aluminum specimens by chemical etching, anodizing and pore widening in this chapter.

Chapter 3

Evaluation of Surface Wettability of Hierarchically Rough Aluminum Surfaces

3.1 Introduction

In the last decades there are many reports showing the superoleophobicity. The superoleophobicity has been achieved by the introduction of re-entrant or hierarchical surface geometries even if the contact angle of oils was less than 90° on their flat counterparts. However, the reported superoleophobicity reported so far has been mostly limited to liquids with surface tensions not less than 27.5 mN m^{-1} (e.g. hexadecane) [1-5]. There are only a very few examples for high contact angle $>150^\circ$ and low contact angle hysteresis $<5^\circ$ for liquids with surface tensions less than 25 mN m^{-1} [6, 7]. Although there have been several reports on superoleophobicity for liquids with surface tensions lower than that of hexadecane recently, the fabrication of super-liquid-repellent surface for any liquids is still challenging. In order to prepare superoleophobic surfaces even for liquids with surface tensions lower than 25 mN m^{-1} , it is expected that fractal-like or more complex re-entrant geometries are suitable [7, 8]. The author considered that fabrication of more random and complex micrometer-scale geometries in the hierarchical structure is necessary. In addition, it is also of importance to fabricate superoleophobic surfaces by practical processes for large-scale industrial production and applications. Therefore, the author prepared micro/nano hierarchical geometry on aluminum surface by a combined practical wet process of chemical etching and anodizing, in Chapter 2.

Herein, in this chapter, the author evaluated the surface wettability of aluminum specimens with hierarchical multi-pore geometries described in the previous chapter, and also controlled the surface wettability by the self-assembled monolayer coating for an application to oil/water separation material. In addition, mechanical, thermal, and

chemical durability of hierarchical aluminum specimens also discussed since durability is of crucial importance for practical applications.

3.2 Experimental

In order to reduce the surface free energy of hierarchical aluminum specimens fabricated in the previous chapter by coating with an organic self-assembled monolayer, the specimens were immersed in ethanol containing 1 mmol dm^{-3} 1H,1H,2H,2H-perfluorodecyl phosphoric acid (FAP) or 1 mmol dm^{-3} *n*-tetradecyl phosphonic acid (TDP) for 48 h at room temperature. Prior to coating, the specimen surfaces were cleaned using a plasma cleaner (Harrick Plasma Co., PDC-32G); by this process a contaminant hydrocarbon layer was removed from the surfaces, and surface –OH groups were introduced. This cleaning process accelerated the formation of organic monolayer coatings [9]. The FAP was synthesized using the approach described in a previous report, and the chemical structure was checked by nuclear magnetic resonance analysis [10]. TDP was obtained from Sigma-Aldrich. Surface wettability was evaluated by contact angle measurements for water, rapeseed oil, hexadecane, dodecane, octane, and hexane droplets ($4 \mu\text{L}$) using an optical contact angle meter (Kyowa Interface Science Co., DM-CE1). The dynamic advancing and receding contact angle measurements were conducted by expansion/contraction method with a syringe.

3.3 Results and discussion

3.3.1 Surface wettability on hierarchically rough aluminum plate

The etched aluminum surface was superhydrophilic with a static contact angles being close to 0° . To convert the surface to superhydrophobic, organic monolayer coating was conducted. After FAP coating on the etched aluminum surface, the dynamic contact angles for water and several oils were measured. Fig. 3.1 shows the advancing contact angle and the contact angle hysteresis for water (surface tension, $\gamma = 72.8 \text{ mN m}^{-1}$) and rapeseed oils ($\gamma = 35 \text{ mN m}^{-1}$) on the chemically etched surface with a FAP coating. Regardless of the HCl concentrations in the etching solutions, i.e. the size of etch pits, the FAP-coated surfaces are superhydrophobic with advancing contact angles larger than 160° and the contact angle hysteresis less than 2° . Thus, the surface is superhydrophobic, even though nanopores are not introduced. Highly rough surfaces, comprising interconnected many cubic pits, makes the surface superhydrophobic. Even for rapeseed oil, the coated surfaces show advancing contact angles higher than 150° and relatively low contact angle hysteresis of $25\text{-}30^\circ$. Rapeseed oil droplets did not stick on the etched surface and rolled off from the surface when tilted to 20° .

However, the etched surface did not show the high repellency for liquids with lower surface tensions, including hexadecane ($\gamma = 27.5 \text{ mN m}^{-1}$). Thus, nanopores were introduced into the etched surface to introduce hierarchical roughness. Fig. 3.2 shows the change in the advancing contact angle and contact angle hysteresis of the etched and anodized aluminum surface as a function of the pore widening duration. Chemical etching was carried out in the solution containing 2 mol dm^{-3} HCl. Anodizing of the etched

aluminum result in an increase in the advancing contact angle for rapeseed oil to 160° , although the contact angle hysteresis is still 24° (no pore widening in Fig. 3.2). The advancing contact angle for rapeseed oil does not change with the pore widening time. Thus, the advancing contact angle is independent of the size of the nanopores. However, the contact angle hysteresis decreases significantly with pore widening time, and reaches $\sim 3^\circ$ after pore widening treatment for 1200 s, indicating that the size of the nanopores or the porosity of the etched pore walls is an important parameter for oil repellency. The water repellency is not influenced by the pore widening and chemical etching conditions, as shown in Figs. 3.1 and 3.2. The significant influence of pore widening on the rolling-off rate of a droplet of rapeseed oil is depicted in Fig. 3.3. The rapeseed oil droplet is rolled off on both surfaces with and without pore widening for 1200 s, but the rolling-off rate is markedly increased by the pore widening. The increased rolling-off rate should be associated with the reduced contact angle hysteresis by pore widening.

The role of micro-pits and nanopores on the liquid repellency can be explained using schematic illustrations shown in Fig. 3.4. The little influence of the introduction of nanopores on the water repellency is associated with the little penetration of water droplet into the micrometer-size pits. The static contact angle for water on the FAP-coated flat aluminum surface was $\sim 120^\circ$. Because of such high contact angle, the water droplet pins on the etched aluminum surface with no water penetration into pits, as shown in Fig. 3.4a. Thus, the introduction of nanopores does not influence the water repellency. For rapeseed oil, the FAP-coated surface is oleophilic; rapeseed oil does penetrate and pin underneath the re-entrant structure within the pits (Fig. 3.4b). The oil penetrates to the re-entrant

regions, at which further penetration is avoided by the pinning effect. Because of penetration to the re-entrant regions, the contact angle hysteresis is relatively high (25-30°) as shown in Fig. 3.1. When the nanopores are introduced and the porosity in the pit wall increases to more than 30%, pinning of rapeseed oil occurs at the nanopores developed on the pit walls close to the top surface (Fig. 3.4c). The suppression of the oil penetration by nanopores effectively enhances the roll-off rate of the oil droplet on the tilted surface (Fig. 3.3).

For the specimens chemically etched, anodized, and pore-widened for 1200 s, dynamic contact angle measurements were carried out for several liquids with further lower surface tensions. Fig. 3.5a discloses the approximately spherical liquid droplets of rapeseed oil, hexadecane, dodecane, and octane with surface tensions of 35.7, 27.5, 25.3, and 21.8 mN m⁻¹, respectively, on the hierarchical surface. Fig. 3.5b shows the influence of pit size (HCl concentration in the etching solution) on the advancing angle and the contact angle hysteresis for several liquids. The advancing contact angles of the specimen with pore widening for 1200 s, shown in Fig. 3.5b, are high, being $\geq 157^\circ$ even for octane, regardless of the pit size. Only a slight increase in the advancing contact angle is found with a decrease in the concentration of HCl in the etching solution. The contact angle hysteresis is also sufficiently low (4° or less) for rapeseed oil, hexadecane and dodecane. For these liquid droplets, the size of the etch pits (HCl concentration) does not influence the contact angle hysteresis. In contrast, a large influence of the pit size is found on the contact angle hysteresis for octane, which is the lowest surface tension examined. The contact angle hysteresis decreases from 18° to 4° by reducing the HCl concentration from

6 to 1 mol dm⁻³.

The sliding angles for several liquids were also measured. Fig. 3.6 shows the sliding angle for various liquid droplets (10 µL) on the FAP-coated hierarchical surfaces prepared at 1 mol dm⁻³ HCl solution for chemical etching, anodizing and pore widening for 1200 s. The sliding angle tends to increase with a decrease in the surface tension of liquid, but the value is still less than 10° even for octane. The sliding angle is also dependent upon the size of liquid droplet, decreasing gradually with an increase in the size of liquid droplet. This agrees with the previous report by Miwa et al [11]. They demonstrated that the sliding angle of water increases as the weight of the droplet decreases, as described by the following equation,

$$k = \left\{ \frac{9m^2(2 - 3 \cos^3 \theta)}{\pi^2} \right\}^{1/3} \frac{\sin \alpha (g\rho^{1/3})}{6 \sin \theta} \quad (3.1)$$

where k , m , θ , α , g and ρ are the constant which is related to the interaction energy between solid and liquid, weight of the droplet, the contact angle, the sliding angle, gravitational acceleration, and specific weight of water, respectively. For the surfaces with relatively small pits of less than 1 µm, the sliding angle becomes high for octane, although no significant pit size dependence of the sliding angle is found for other liquids with higher surface tensions. The results are consistent with the contact angle hysteresis shown in Fig. 3.5.

The findings in this study reveal that a large pit size is preferable for super-repellency for low-surface-tension liquids, being consistent with the previous report of the wettability of dual-pillar surfaces prepared by the oblique angle deposition of Al-Nb

alloy submicrometer pillar films and subsequent anodizing [3-5]. The gap size between neighboring submicrometer pillars was one of the important parameters for obtaining superoleophobicity, and a gap size larger than 400 nm was needed to observe super-repellency for rapeseed oil and hexadecane. Since the pit size in this study is much larger than the gap size of the dual-pillar surfaces, super repellency for liquids with lower surface tensions can be achieved. Tuteja et al. also demonstrated that relatively large pores of $>1 \mu\text{m}$ and relatively high porosity in the larger pore walls are essential for super repellency toward low-surface-tension liquids [9, 12].

In Figs. 3.5 and 3.6, relatively large influence of pit size on the contact angle hysteresis and sliding angle is found only for octane. This may result from the fact that the static contact angle for octane on the flat FAP-coated aluminum surface was as low as 45° and the angle increased to 65° for dodecane. Since the liquid penetration pressure into the pits increases with the reduction of the static contact angle and the decrease in the pit size, the relatively large pits should be needed for the effective pinning by nanopores for octane. The higher static contact angles on the flat surface for other liquids with higher surface tensions may result in the little influence of the pit size on the contact angle hysteresis and sliding angle.

3.3.2 Surface wettability on triple-pore hierarchical aluminum mesh

Fig. 3.7 shows the water and hexane droplets on various rough aluminum mesh surfaces shown in Fig. 2.4 (Chapter 2) after coating with an FAP monolayer. All the surfaces showed high static contact angles of $>150^\circ$ for water; the surfaces were

superhydrophobic. In contrast, the contact angles for hexane ($\gamma = 18.4 \text{ mN m}^{-1}$) were largely dependent upon the surface morphology. The aluminum mesh with nanoporous oxide showed a low contact angle for hexane below 10° ; the surface was superoleophilic. The contact angle on the etched aluminum mesh increased to $\sim 130^\circ$, and a further increase in the contact angle for hexane ($>150^\circ$) was found on the aluminum mesh with triple-pore hierarchical morphology. This contact angle is higher than that on the aluminum plate with nanopores and micrometer etch pits.

Fig. 3.8 shows the changes in the advancing contact angles and the CAH of various FAP-coated aluminum surfaces with the surface tension of the liquid. All four aluminum surfaces with double- and triple-pore hierarchical morphologies showed advancing contact angles higher than 160° and very low CAH for water; the CAH on the aluminum mesh with oxide nanopores was 12° , and those on the other three surfaces were lower than 2° . Thus, all the surfaces are superhydrophobic. The advancing contact angle on the aluminum mesh with oxide nanopores decreased gradually with a decrease in the liquid surface tension and became lower than 10° for liquids with surface tensions lower than 25 mN m^{-1} . The etched aluminum mesh showed higher repellency for oils; the advancing contact angles were higher than 150° for liquids with surface tensions higher than 22 mN m^{-1} . Moreover, the CAH was also lower than 10° for the liquids with surface tensions higher than 25 mN m^{-1} . Thus, the introduction of microscale roughness on the aluminum mesh is more effective in enhancing the oil repellency than the introduction of nanoscale roughness. Further improved liquid repellency of the FAP-coated aluminum mesh with triple-pore morphology is obvious in Fig. 3.8. This surface showed advancing contact

angles higher than 150° and CAH lower than 3° for any liquid, including hexane with a surface tension as low as 18.4 mN m^{-1} , examined in this study. In addition to hydrocarbon liquids, the advancing contact angle and CAH for 2-propenol ($\gamma = 20.5 \text{ mN m}^{-1}$) are 159° and 3.1° , and 159.5° and 2.9° for ethanol ($\gamma = 22.5 \text{ mN m}^{-1}$), and 160° and 2.7° for acetone ($\gamma = 23.3 \text{ mN m}^{-1}$), respectively. Thus, this surface is really superoleophobic. Such surfaces showing super-repellency for any liquid are still very limited. The triple-pore morphology is one of the important parameters for such high liquid repellency. In fact, the FAP-coated aluminum plate with microscale etch pits and oxide nanopores showed less repellency for liquids with low surface tensions as shown in Fig. 3.8; this surface also showed a high advancing contact angle above 150° for any liquid, but the CAH increased for liquids with surface tension of 25 mN m^{-1} or lower. The excellent liquid repellency is demonstrated in Fig. 3.9, in which a hexane droplet is seen clearly rolling off rapidly.

Figs. 3.10 presents the schematic illustration showing the influence of the surface morphology on the surface wettability. As described above, the chemically etched aluminum plate with a nanopore oxide layer showed superoleophobicity for many liquids with low surface tensions above 20 mN m^{-1} . However, hexane with a surface tension as low as 18.4 mN m^{-1} penetrates into pores to the depth where the complex re-entrant curvature is present (Fig. 3.10a). Thus, the contacting area is relatively large to hexane, resulting in the contact angle hysteresis larger than 40° .

When the nanopores were introduced on the aluminum mesh consisting of aluminum wire of $100 \mu\text{m}$ in diameter, the liquid repellency for oils was not as high as that of the chemically etched aluminum plate with nanopores (Fig. 3.9). As shown in Fig.

3.10b, the penetration of liquids with low surface tensions cannot be avoided in this case, and relatively low contact angles and high CAH are obtained on this surface. Fig. 3.10c shows the illustration of the simultaneous introduction of micrometer-scale etch pits and nanopores by chemical etching and anodizing of aluminum mesh, respectively. In this case, the hexane penetration occurred into etch pits vertical to the ground to the depth where the complex re-entrant curvature is present on the aluminum wire surfaces, while effectively suppressed by oblique etch pits on the aluminum wire sidewalls, and the liquid-solid contact area was limited by mesh pores 150 μm in diameter. Thus, the low CAH of $<3^\circ$ on the surface with triple-pore hierarchical morphology even for hexane may be associated with its limited solid-liquid contact area.

Kota et al. reported that the apparent contact angles of liquids on hierarchically structured surfaces could be determined by the following equation [13]:

$$\cos \theta_n = (1 - f_{LV,n}) \cos \theta_{n-1} - f_{LV,n} \quad (3.2)$$

Here, $n = 1, 2, 3, 4$ and so on, and is the number of scales of texture, $f_{LV, n}$ is the area fraction of the liquid-air interface for the n th scale of texture, and θ_n and θ_{n-1} are the apparent contact angles on hierarchically structured surfaces with n and $n - 1$ scales of texture, respectively. It is evident from the equation that θ_n increased as the number of scales of texture n increases. The increased advancing contact angle on the present triple-pore hierarchical morphology compared to the chemically etched aluminum mesh with only microscale pits is qualitatively consistent with this equation.

Fig. 3.11 shows the changes in the advancing contact angles and CAH with the surface tension of the liquid on the aluminum mesh surfaces with triple-pore hierarchical

morphologies and various etch pit sizes. The advancing contact angles and the CAH for liquids with surface tensions of $>25 \text{ mN m}^{-1}$ are almost independent of the size of the etch pits (HCl concentration), but the size of the etch pits have a significant influence on the CAH for the liquids with surface tensions of $<25 \text{ mN m}^{-1}$; the CAH decreases as the size of the etch pits increases. Even if the triple-pore hierarchical morphologies are developed, the difference in pore sizes affects the wettability, although the advancing contact angle is not influenced by the size of the etch pits as expected from eq. 3.2. It is likely that the suppression of liquid penetration into micrometer etch pits becomes more difficult for the smaller etch pits because the penetration pressure of liquid into etch pits increases as the size of etch pits decreases as well as hierarchically rough aluminum plate.

3.3.3 Application to oil/water separation

By coating the triple-pore aluminum mesh with an FAP monolayer, superoleophobicity for practically any liquid is achieved. The wettability is also dependent upon the coating material, i.e., surface free energy of coated material. The non-coated aluminum mesh showed contact angles of $<10^\circ$ for all liquids including water; the non-coated surface was superhydrophilic and superoleophilic. Thus, all liquids passed through the non-coated mesh readily. The TDP-coated aluminum mesh with $-\text{CH}_3$ surface had a surface free energy of $\sim 24 \text{ mN m}^{-1}$, which was estimated from the Zisman plot of the TDP-coated flat aluminum surface [14, 15]. The surface free energy obtained was a typical value of $-\text{CH}_3$ terminated surfaces. As shown in Fig. 3.12a, the TDP-coated aluminum mesh with triple-pore morphology is superhydrophobic with a contact angle

for water of 157° . However, this surface did not show high repellency for oils; the contact angles for both rapeseed oil and cyclohexane ($\gamma = 25.3 \text{ mN m}^{-1}$) were lower than 10° (Fig. 3.12b). The higher surface energy of $\sim 24 \text{ mN m}^{-1}$ for the TDP coating compared to that for the FAP coating (7 mN m^{-1}) changes the surface from superoleophobic (FAP coating) to superoleophilic (TDP coating).

Since the TDP-coated aluminum mesh showed completely different wettability for water (superhydrophobic) and oils (superoleophilic), the author attempted to use the aluminum mesh for water/oil separation. When the aluminum mesh without any surface treatment was used, both water and cyclohexane penetrated the mesh, and the water and cyclohexane were not separated. In contrast, only cyclohexane penetrated through the TDP-coated aluminum mesh with triple-pore morphology, and no penetration of water through the mesh occurred. Thus, water and cyclohexane were almost completely separated and collected in different containers (Fig. 3.13). Successful separation occurred even when a mixture of water and rapeseed oil with high viscosity was used. However, in this case, the aluminum mesh was wetted with the oils and was not easily cleaned after separation.

Another successful water/oil separation was achieved by using non-coated aluminum mesh with optimized triple-pore morphology. When the mesh was wetted with water, it was found that no penetration of oil occurred through the mesh. Thus, the separation treatment was performed using the non-coated aluminum mesh with triple-pore morphology. In this case, only water passed through the mesh, and cyclohexane or rapeseed oil did not (Fig. 3.14). The separation of water and oil was achieved with high

efficiency. The mesh was coated with a thin water layer, and no contamination of the mesh by oils occurred in this case. In this manner, the aluminum mesh with optimized triple-pore morphology is suitable for the water/oil separation application.

Separating oil and water mixtures is of key importance for cleanup of the environment after oil spillages. The present mesh with triple pore morphologies shows completely different wettability for water and oil and hence shows effective separation of these liquids. In addition, the mesh with the unique morphology could be prepared readily simply by a combination of practical chemical and electrochemical processes. The material is, therefore, promising for the development of new technologies to assist in the cleanup of environments contaminated with oils.

3.3.4 Stability of super-repellent-hierarchically rough aluminum surfaces

a) Thermal stability

The FAP-coated hierarchical dual-pore surface, chemically etched in the solution containing 1 mol dm^{-3} HCl and then anodized and pore-widened for 1200 s, was heated in air at several temperatures for 1 h in order to examine the thermal stability of the present superoleophobic surface. Fig. 3.15 shows the change in the advancing contact angle and contact angle hysteresis with heat treatment temperature. The low contact angle hysteresis less than 10° for rapeseed oil is maintained up to 125°C . Further heating at 175°C results in the increase in the contact angle hysteresis to 23° , although the advancing contact angle is still as high as 150°C for rapeseed oil. The surface becomes superoleophilic with

advancing contact angle close to 0° after heating at 225°C . Thermal decomposition of the fluoroalkyl coating may cause the thermal degradation. For water repellency, the thermal degradation temperature appears to shift towards higher temperature by 50°C . Thus, the surface becomes superhydrophilic after heating at 275°C . From XPS analysis the thermal decomposition of FAP at this temperature was confirmed from the marked reduction of fluorine concentration at the surface (Fig. 3.16).

b) The breakthrough pressure for a liquid droplet

Fig. 3.17 demonstrates bouncing water and dodecane droplets falling onto the super-repellent aluminum plate surface formed by chemical etching in the solution containing 1 mol dm^{-3} HCl and anodizing and pore-widening for 1200 s, confirming extremely high repellency even for liquids with low surface tensions. A falling droplet of dodecane (surface tension of 25.3 mN m^{-1}) does not penetrate the FAP-coated dual-pore surface, rebounding off this surface. This dynamic liquid repellency demonstrates the robustness of the composite interface on the dual-pore surface even for liquids with low surface tensions.

When a liquid droplet of density ρ is dropped under gravity from a height h , it impacts the solid surface with a breakthrough pressure, $P_{\text{breakthrough}} = \rho gh$, which is the minimum pressure that causes a transition from the Cassie-Baxter state to the fully wetted Wenzel state [7]. This is also an important physical characteristic of superoleophobic surfaces. Even at a height of 100 mm ($P_{\text{breakthrough}} = 735 \text{ Pa}$), the surface did not show the transition from the metastable Cassie–Baxter state to Wenzel state for dodecane. For

octane, the metastable Cassie–Baxter state was stable up to the height of 50 mm ($P_{\text{breakthrough}} = 343 \text{ Pa}$).

Fig. 3.18 shows the robustness of a hexane liquid droplet on hierarchical triple-pore aluminum mesh as a function of HCl concentration (the size of micrometer etch pits). As shown in Fig. 2.5 (Chapter 2) the etch pits become larger with a decrease in the HCl concentration. The higher $P_{\text{breakthrough}}$ is obtained at a lower HCl concentration (larger pit size), in agreement with the CAH. Even at a height of 50 mm ($P_{\text{breakthrough}} = 343 \text{ Pa}$), the surface formed at 1 mol dm^{-3} HCl did not show the transition from the metastable Cassie–Baxter state to the Wenzel state even for hexane.

c) Mechanical stability

For an application of superoleophobic surfaces in an outdoor atmosphere for long time, the mechanical stability against airborne particles, is of crucial importance. In this study, the mechanical stability was evaluated by dropping lots of glass beads with diameter of 0.5~0.7 mm and weight of ~0.25 mg from the height of 10 cm. Fig. 3.19 shows the change in the advancing contact angle and contact angle hysteresis as a function of dropping number of glass beads (50 g and ~20,000 beads per cycle). The superhydrophobic and superoleophobic properties can be maintained even after dropping beads 3 times, maintaining the advancing contact angles and contact angle hysteresis for water and hexadecane ~160° and <10°, respectively. However, after >4 times, the contact angle hysteresis increases to >10° for both water and hexadecane, resulting in loss of the superhydrophobic and superoleophobic properties. Fig. 3.20 shows scanning electron

micrographs on hierarchical dual-pore aluminum surface after 0-5 times of dropping of glass beads (50 g). The surface morphologies were almost similar to original one after 3 times of dropping, but the fraction of flat areas increases after dropping beads >4 times. SEM backscattering electron images shown in Fig. 3.21 disclose the presence of light appearance regions in the flat surface areas, probably indicating the damage of the FAP-coating. In these regions, the aluminum oxide surface is exposed, becoming one of the reasons for the degradation of the superoleophobicity. Since 50 g beads contain approximately 20000 beads, the super-repellent surface was impacted by beads with 2500 times cm^{-2} mathematically in this case. Thus, the super-liquid-repellent properties can be maintained even after approximately 7500 times cm^{-2} of impacts by free fall of glass beads from a height of 10 cm.

3.4 Conclusions

In this chapter, the surface wettability of hierarchical aluminum specimens prepared in Chapter 2 were evaluated after organic monolayer coating. The FAP-coated surfaces with optimized hierarchical multi-pore structure show super-repellency even for hexane with the surface tension as low as 18.4 mN m^{-1} . The size of the micrometer etch pits and nanopore porosity greatly influence the CAH for liquids with lower surface tensions, while hardly affect the wettability to water. The preparation process of the hierarchical aluminum surface is simple, cost-effective and practically readily applicable.

In addition, the TDP-coated aluminum mesh with the hierarchical triple-pore

geometry was superhydrophobic and superoleophilic; the mesh can be used successfully for water/oil separation. The non-coated hierarchical mesh is also useful for the separation; only water passes through the mesh in this case.

The thermal, mechanical, and chemical stabilities of superoleophobic aluminum surfaces were also evaluated. The superoleophobicity degraded at $>150^{\circ}\text{C}$ due to decomposition of FDPA monolayer coating. It was also confirmed the super-repellency gradually decreased by impacting numbers of small glass beads because of partial surface geometry destruction.

References

- [1] A. Tuteja, W. Choi, M. L. Ma, J. M. Mabry, S. A. Mazzella, G. C. Rutledge, G. H. McKinley, R. E. Cohen, *Science* **318**, 1618 (2007).
- [2] A. Tuteja, W. Choi, J. M. Mabry, G. H. McKinley, R. E. Cohen, *Proc. Natl. Acad. Sci. U.S.A.* **105**, 18200 (2008).
- [3] T. Fujii, Y. Aoki, H. Habazaki, *Langmuir* **27**, 11752 (2011).
- [4] T. Fujii, H. Sato, E. Tsuji, Y. Aoki, H. Habazaki, *J. Phys. Chem. C* **116**, 23308 (2012).
- [5] T. Fujii, Doctoral thesis at Graduate School of Engineering, Hokkaido Univ. (2012).
- [6] H. Zhou, H. Wang, H. Niu, A. Gestos, T. Lin, *Adv. Funct. Mater.* **23**, 1664 (2013).
- [7] A. K. Kota, Y. Li, J. M. Mabry, A. Tuteja, *Adv. Mater.* **24**, 5838 (2012).
- [8] T. Onda, S. Shibuichi, N. Satoh, K. Tsujii, *Langmuir* **12**, 2125 (1996).
- [9] H. Sato, T. Fujii, E. Tsuji, Y. Aoki, K. Shimizu, P. Skeldon, G. E. Thompson, H.

- Habazaki, *Surf. Interface Anal.* **45**, 1441 (2013).
- [10] S. Shibuichi, T. Yamamoto, T. Onda, K. Tsujii, *J. Colloid Interface Sci.* **208**, 287 (1998).
- [11] M. Miwa, A. Nakajima, A. Fujishima, K. Hashimoto, T. Watanabe, *Langmuir* **16**, 5754 (2000).
- [12] S. J. Pan, A. K. Kota, J. M. Mabry, A. Tuteja, *J. Am. Chem. Soc.* **135**, 578 (2013).
- [13] A. K. Kota, G. Kwon, A. Tuteja, *NPG Asia Mater.* **6**, e109 (2014).
- [14] W. A. Zisman, Contact angle, Wettability, and Adhesion, Chapter 1, *Adv. Chem. Ser.* **43**, 1 (1964).
- [15] H. Habazaki, H. Sato, E. Tsuji, Y. Aoki, K. Shimizu, *ECS Trans.* **58**, 75 (2014).

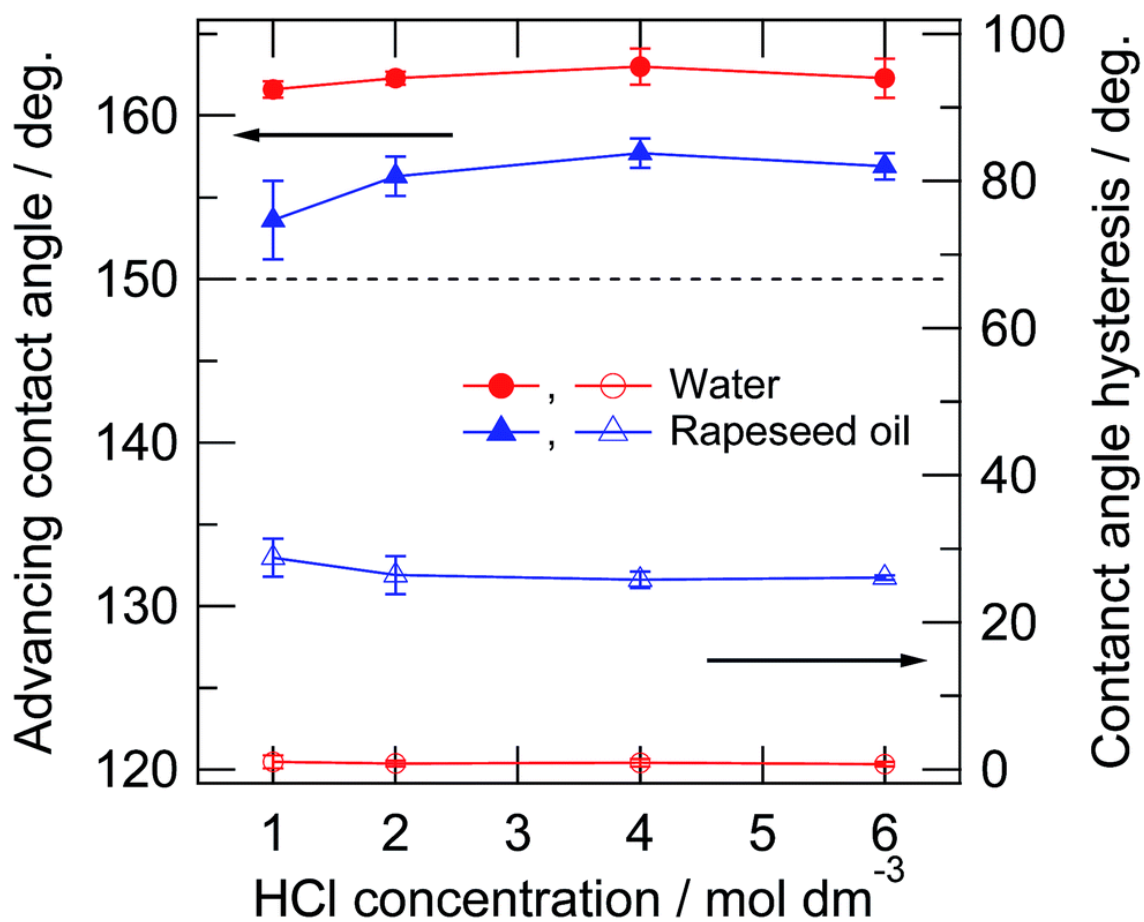


Figure 3.1 Advancing contact angles and contact angle hysteresis for water and rapeseed oil on the chemically etched surfaces with a FAP coating as a function of HCl concentration in the etching solution.

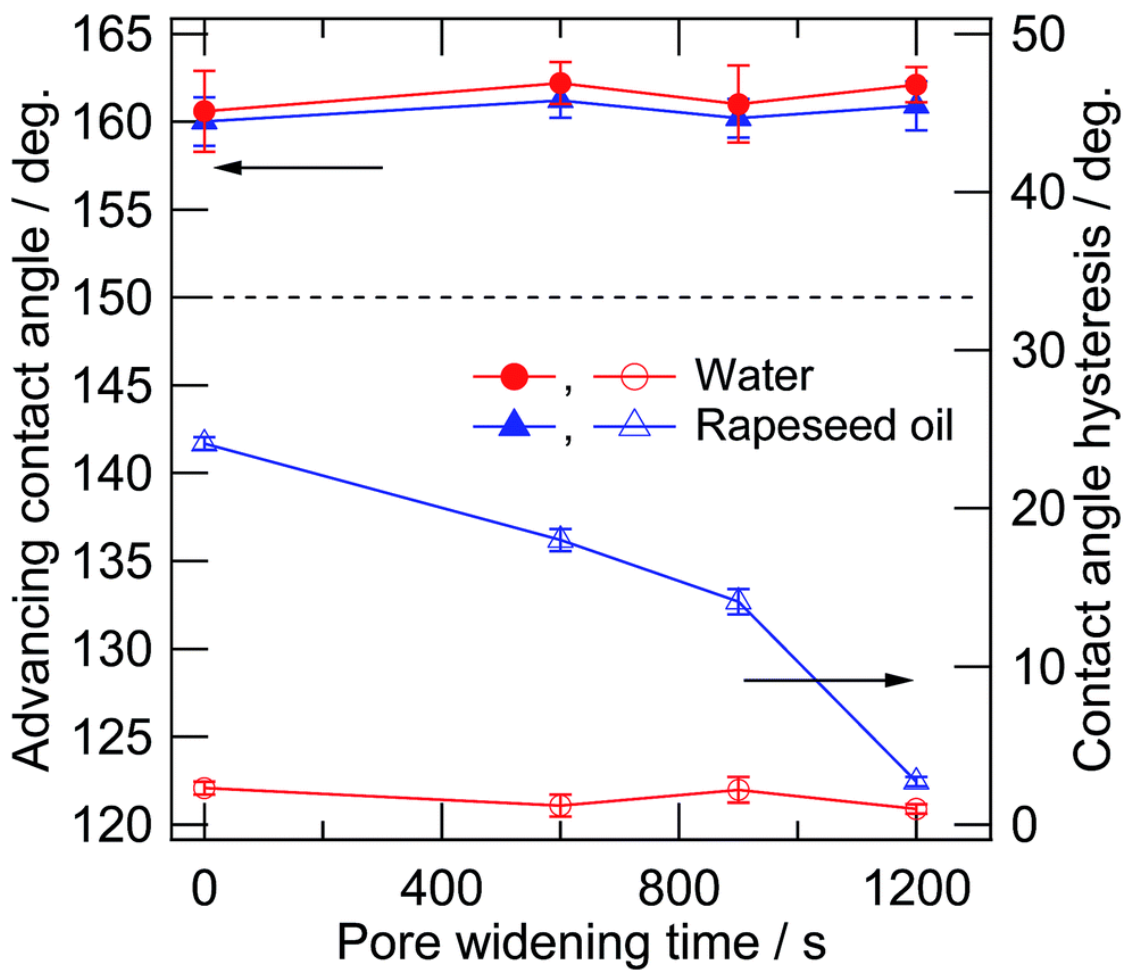


Figure 3.2 Dynamic contact angles for water and rapeseed oil on an etched and anodized surface as a function of pore widening time.

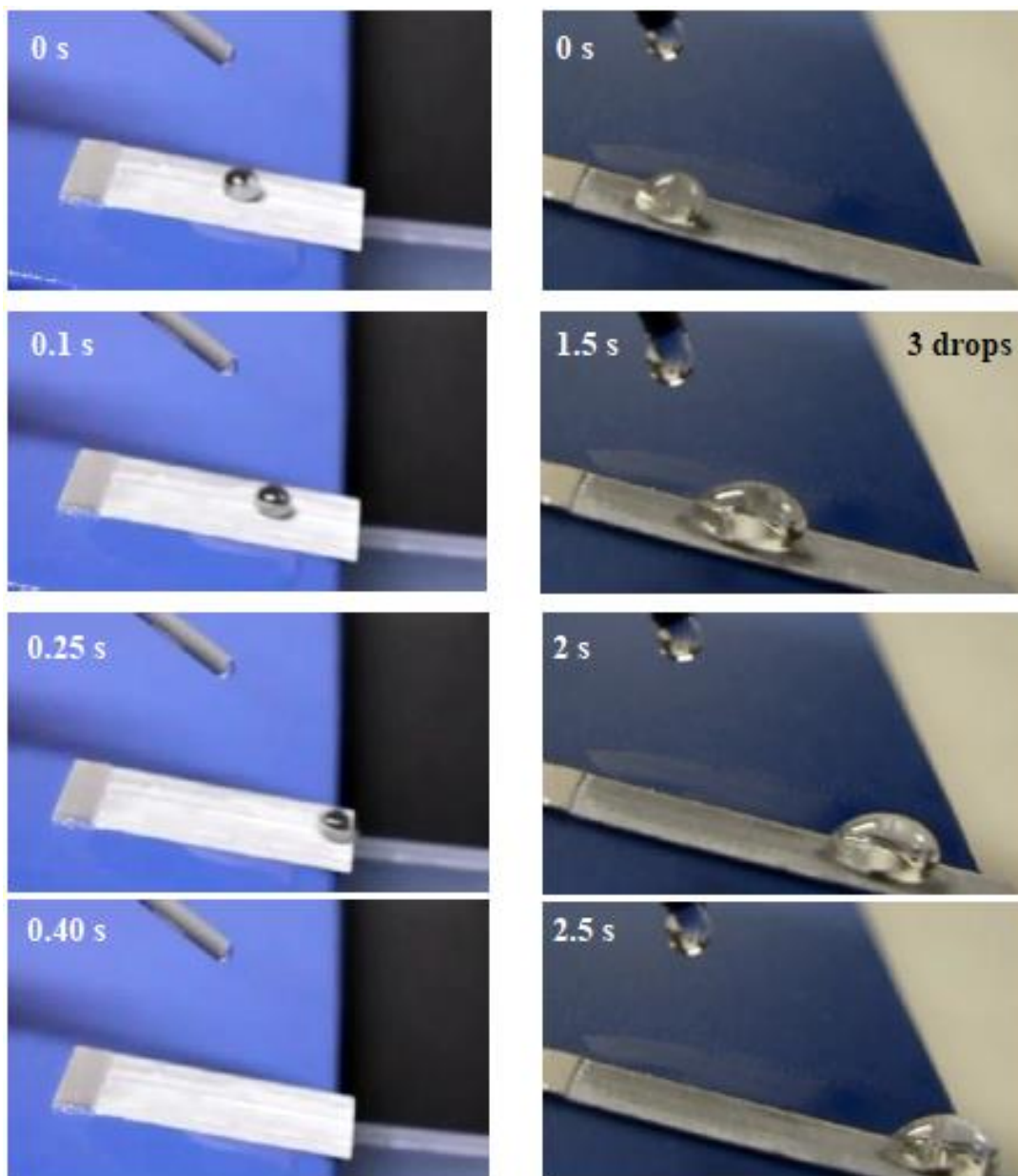


Figure 3.3 The rolling-off behavior of rapeseed oil on etched aluminum surfaces with and without pore widening for 1200 s.

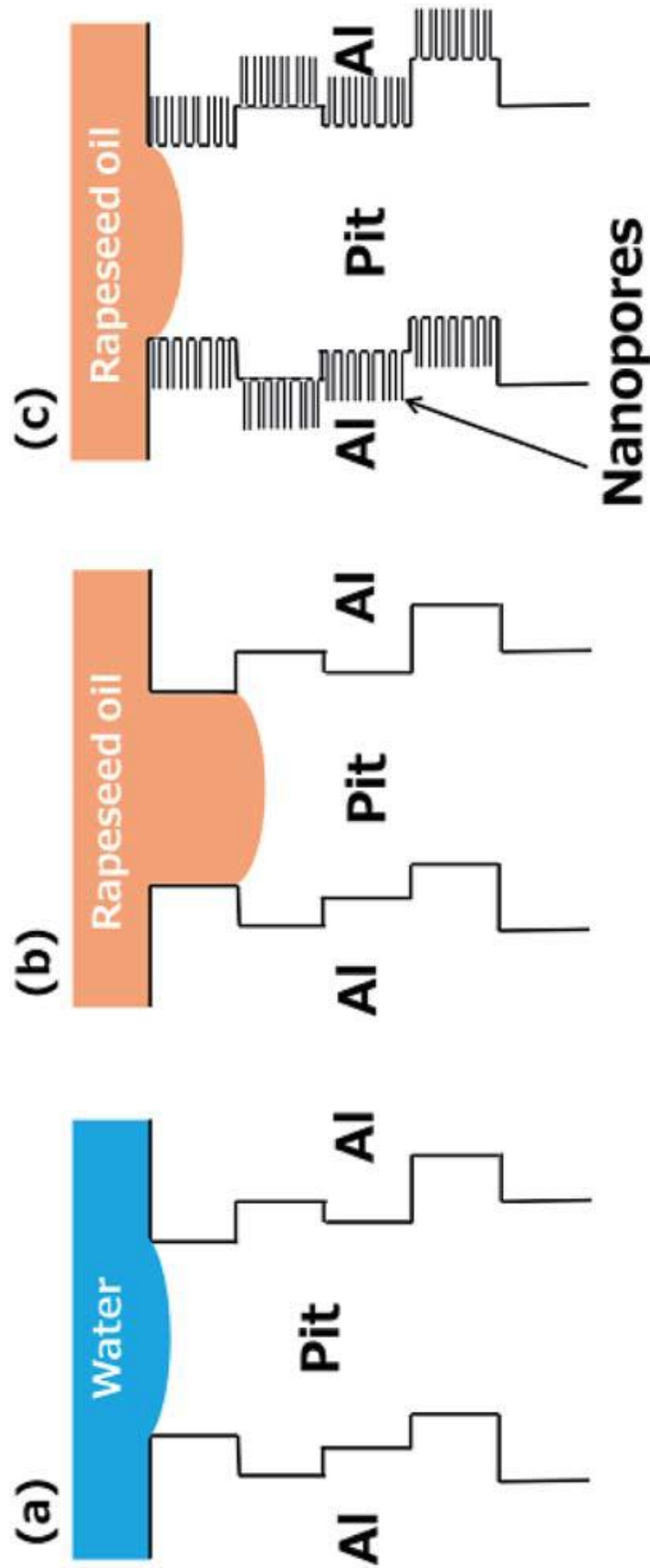


Figure 3.4 Schematic illustration showing the (a) water and (b and c) rapeseed oil penetration into micrometer-size pits (a and b) without and (c) with nanopores.

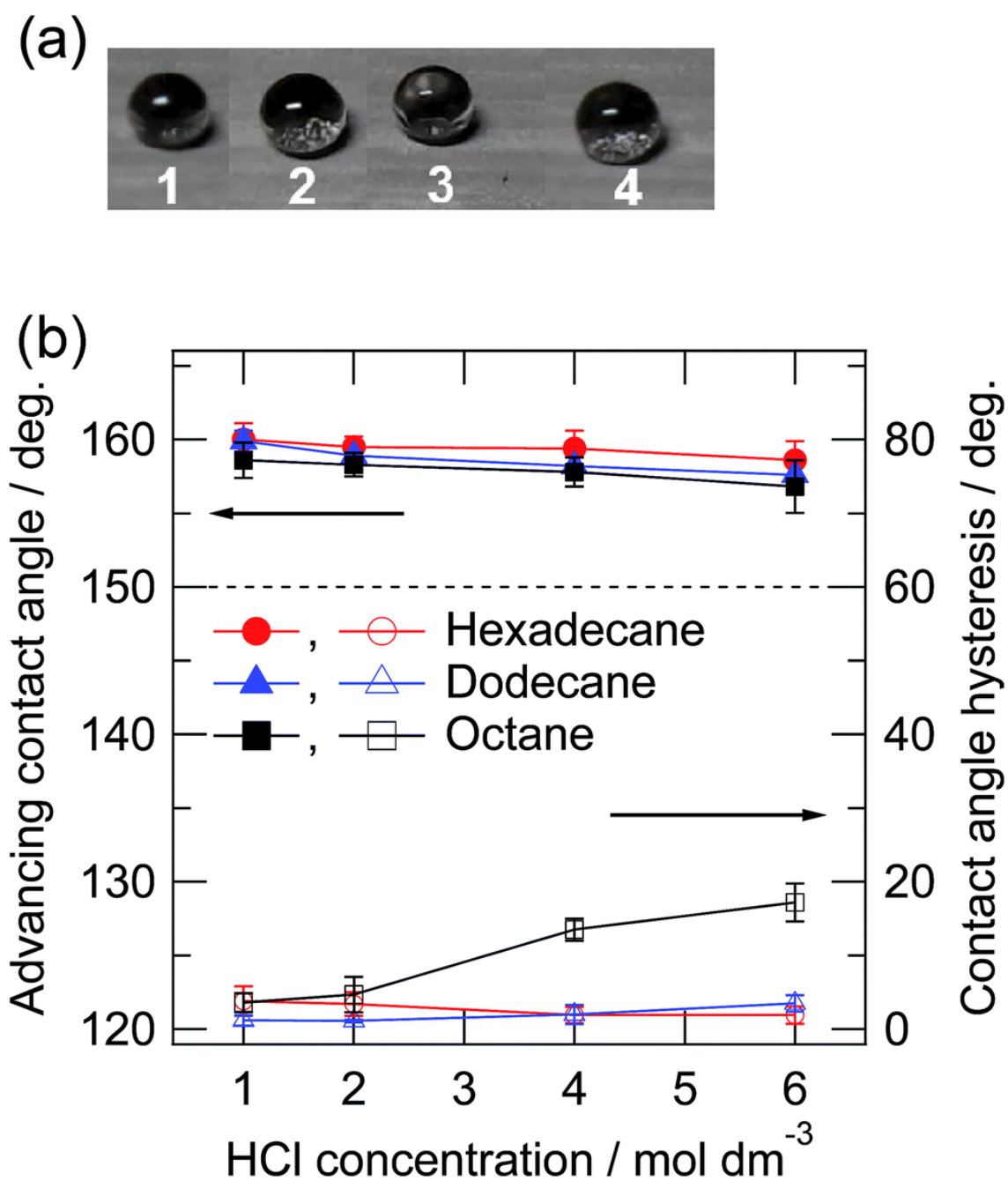


Figure 3.5 (a) Liquid droplets (2 mm diameter) on the fabricated super-oleophobic surface: (1) rapeseed oil, (2) hexadecane, (3) dodecane, and (4) octane. (b) Advancing contact angles and contact angle hysteresis for hexadecane, dodecane, and octane as a

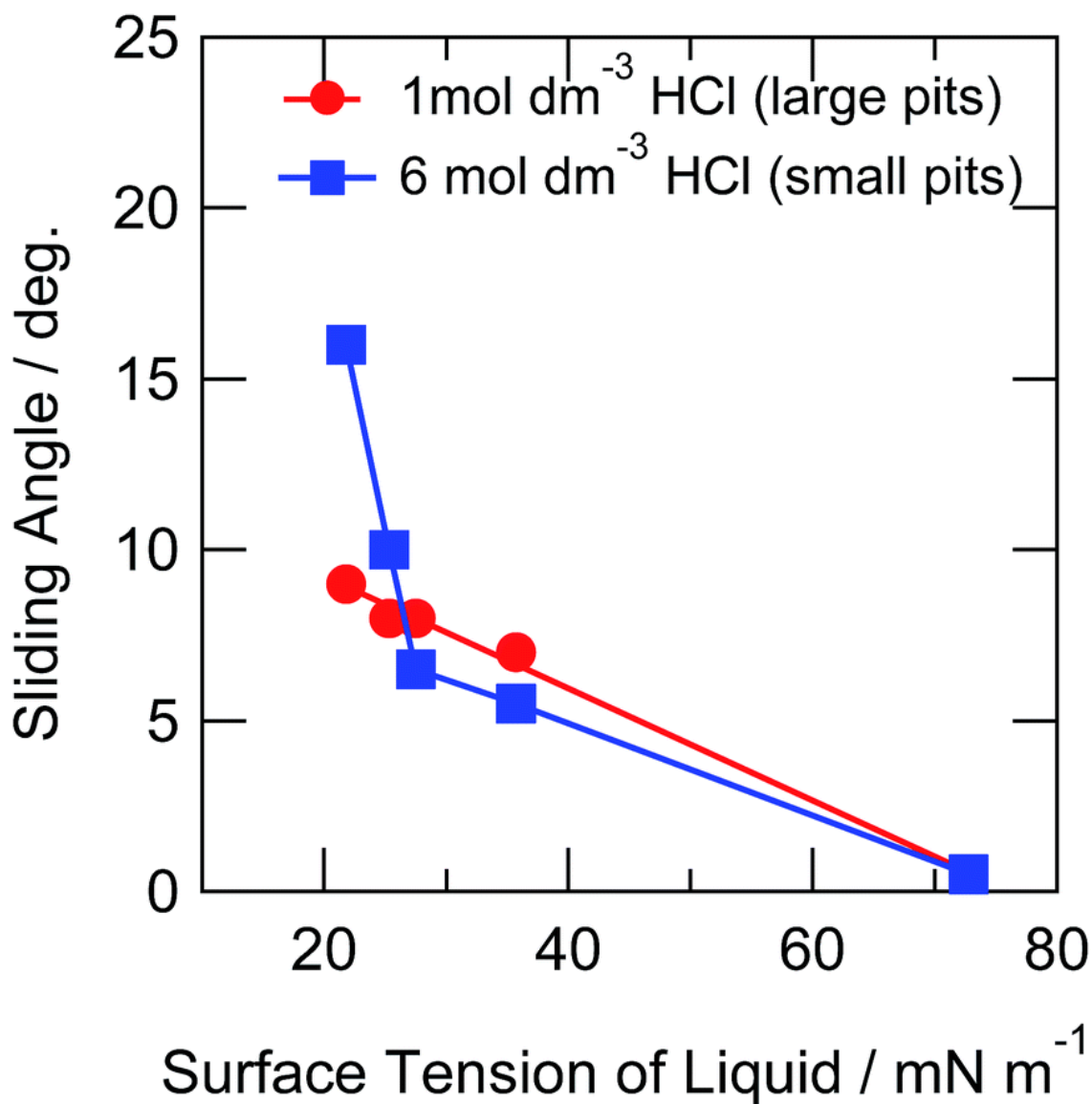


Figure 3.6 Sliding angle of various liquids on the FAP-coated dual-pore hierarchical surface, chemically etched in solutions containing 1 and 6 mol dm⁻³ HCl, as a function of surface tension of liquids.

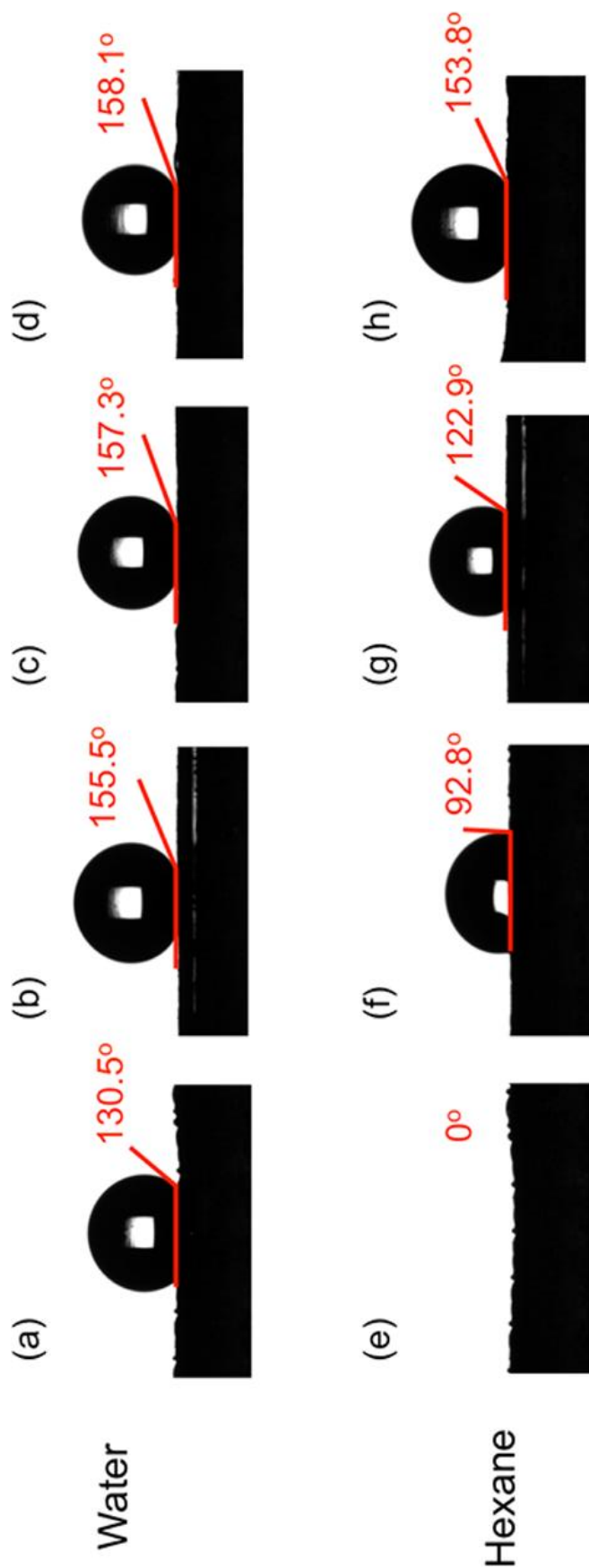


Figure 3.7 Optical images of (a-d) water and (e-f) hexane droplets on aluminum surfaces with hierarchical structures: aluminum mesh with (a, e) nanopores, (b, f) micrometer etch pits, and (d, h) nanopores and micrometer etch pits, and (c, g) an aluminum plate with nanopores and micrometer etch pits. All of the surfaces were coated with an FAP monolayer.

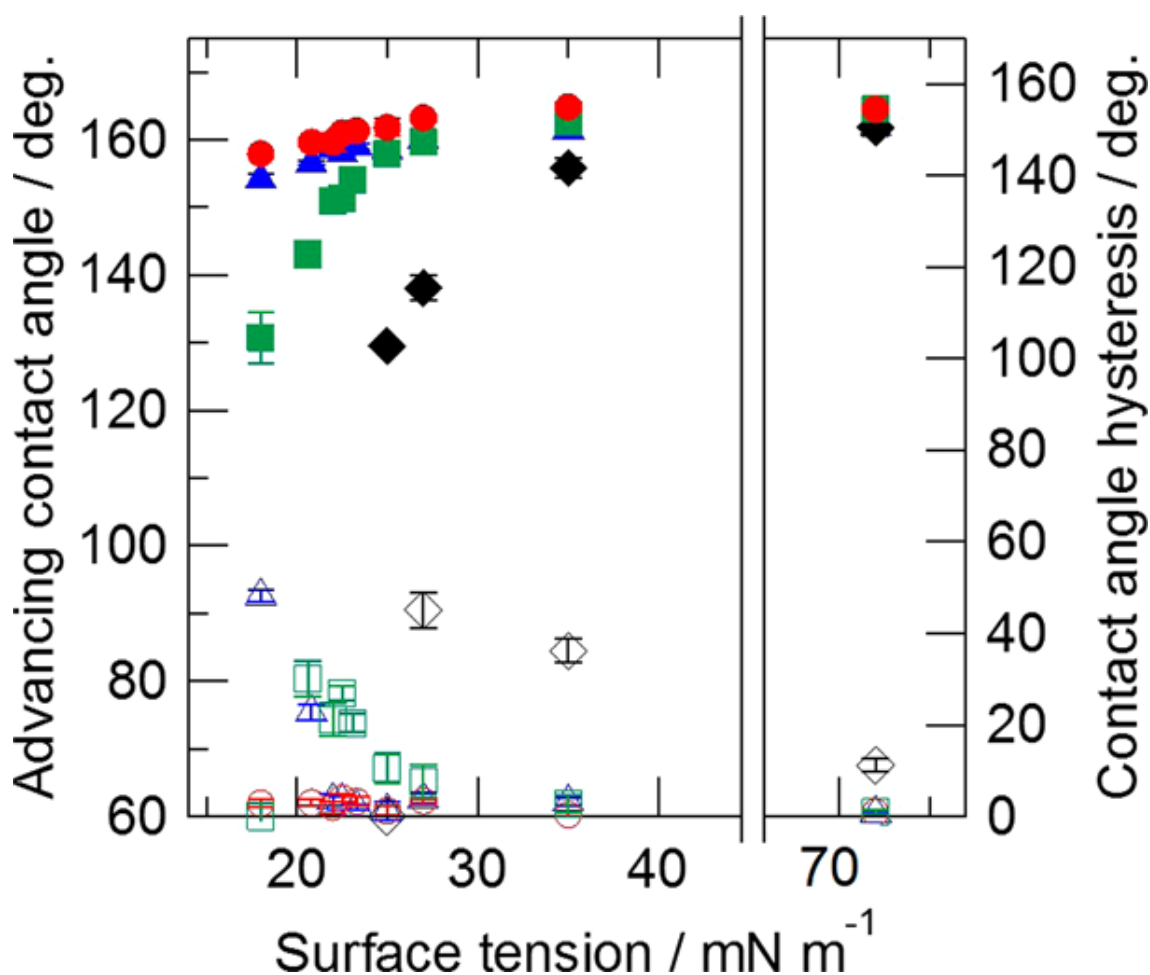


Figure 3.8 Advancing contact angles and contact angles for liquids with various surface tension on the FAP-coated aluminum mesh with (◆, ◇) nanopores, (■, □) micrometer etch pits, and (●, ○) nanopores and micrometer etch pits and (▲, △) FAP-coated aluminum plate with nanopores and micrometer etch pits.

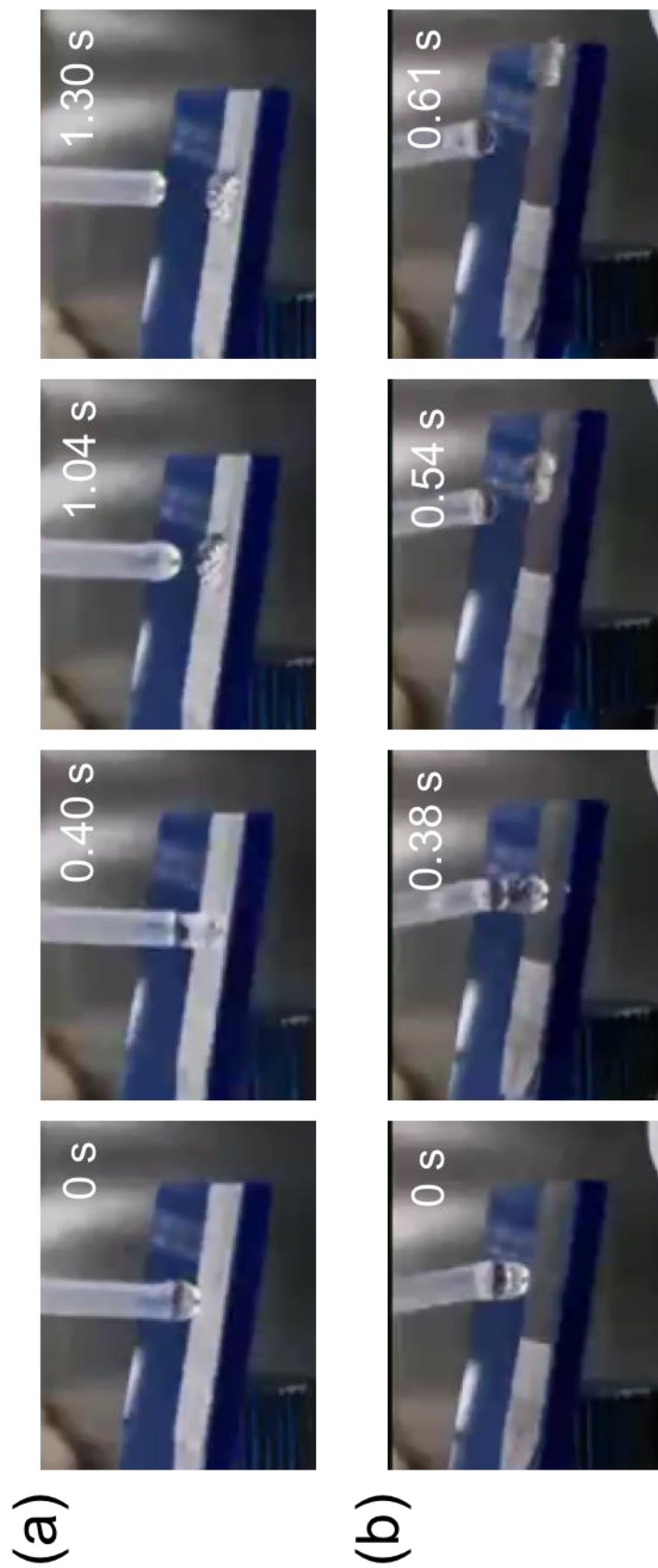


Figure 3.9 Rolling-off behaviors of hexane droplets on aluminum mesh surfaces with or without etch pits and oxide nanopores.

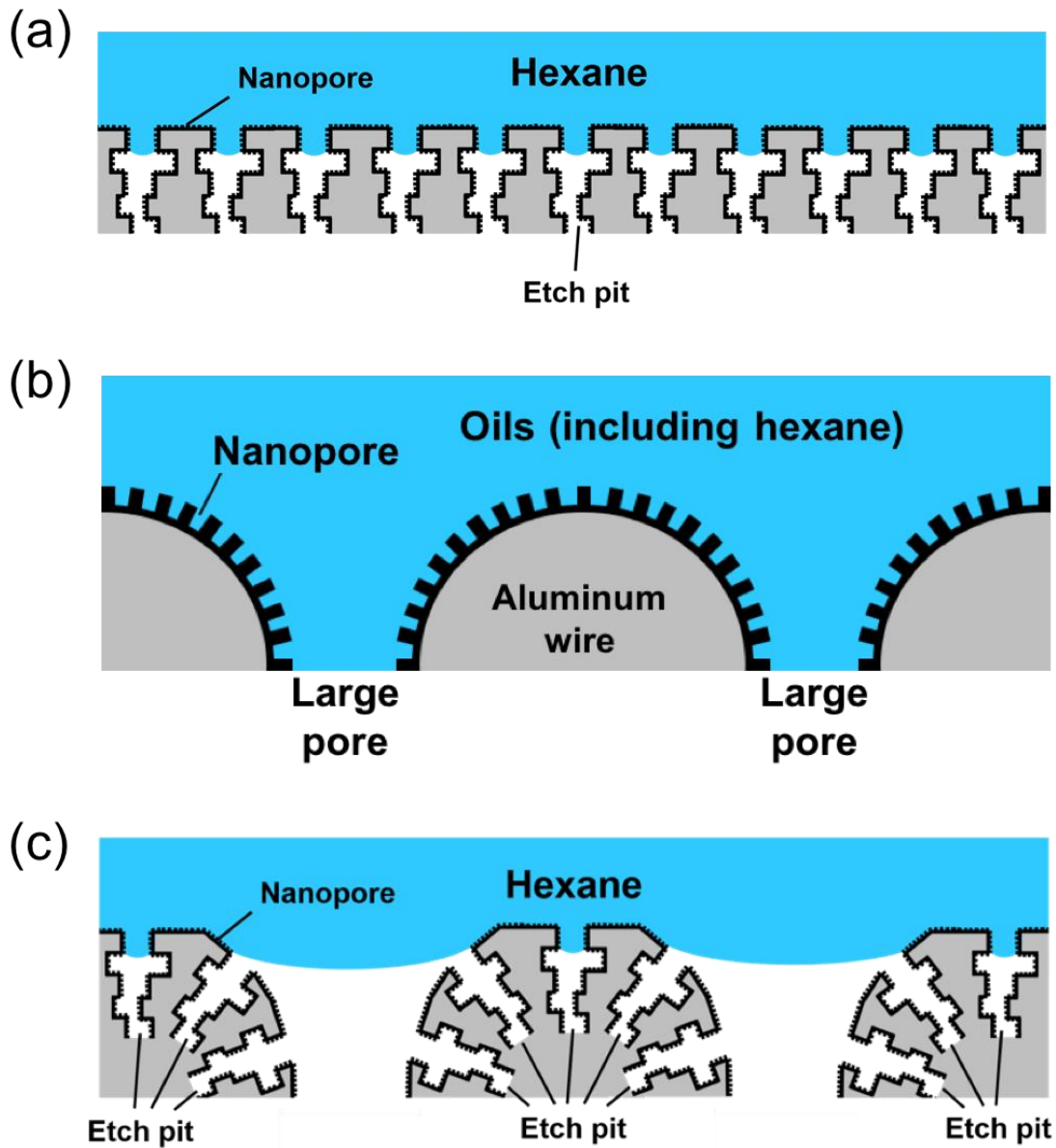


Figure 3.10 Schematic illustrations showing liquid (hexane) penetration into pores on aluminum plate (a) chemically etched and anodized and on aluminum mesh (b) anodized and (c) chemically etched and anodized.

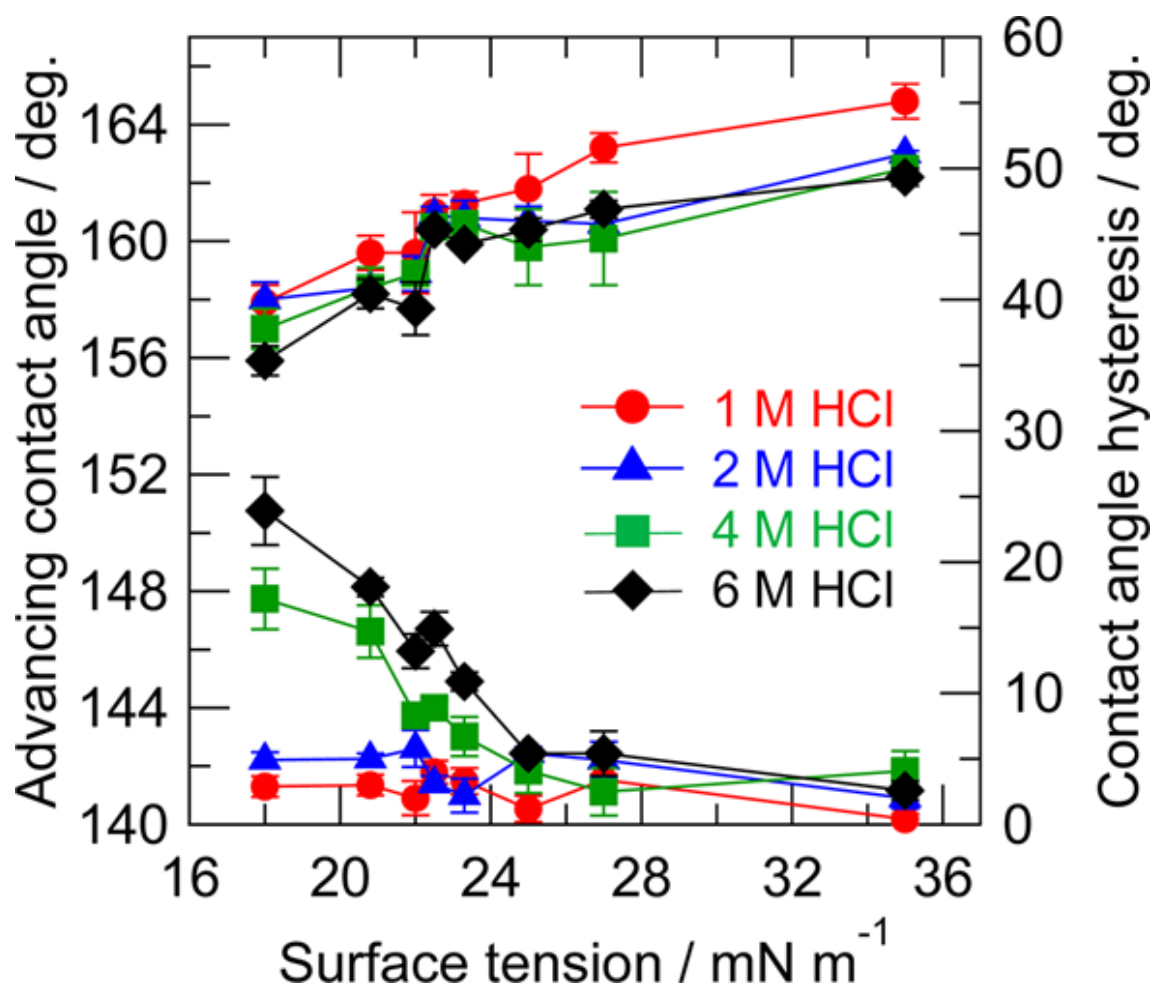


Figure 3.11 Advancing contact angles and CAH on the FAP-coated aluminum mesh surfaces with triple-pore morphologies as a function of surface tension of liquid.

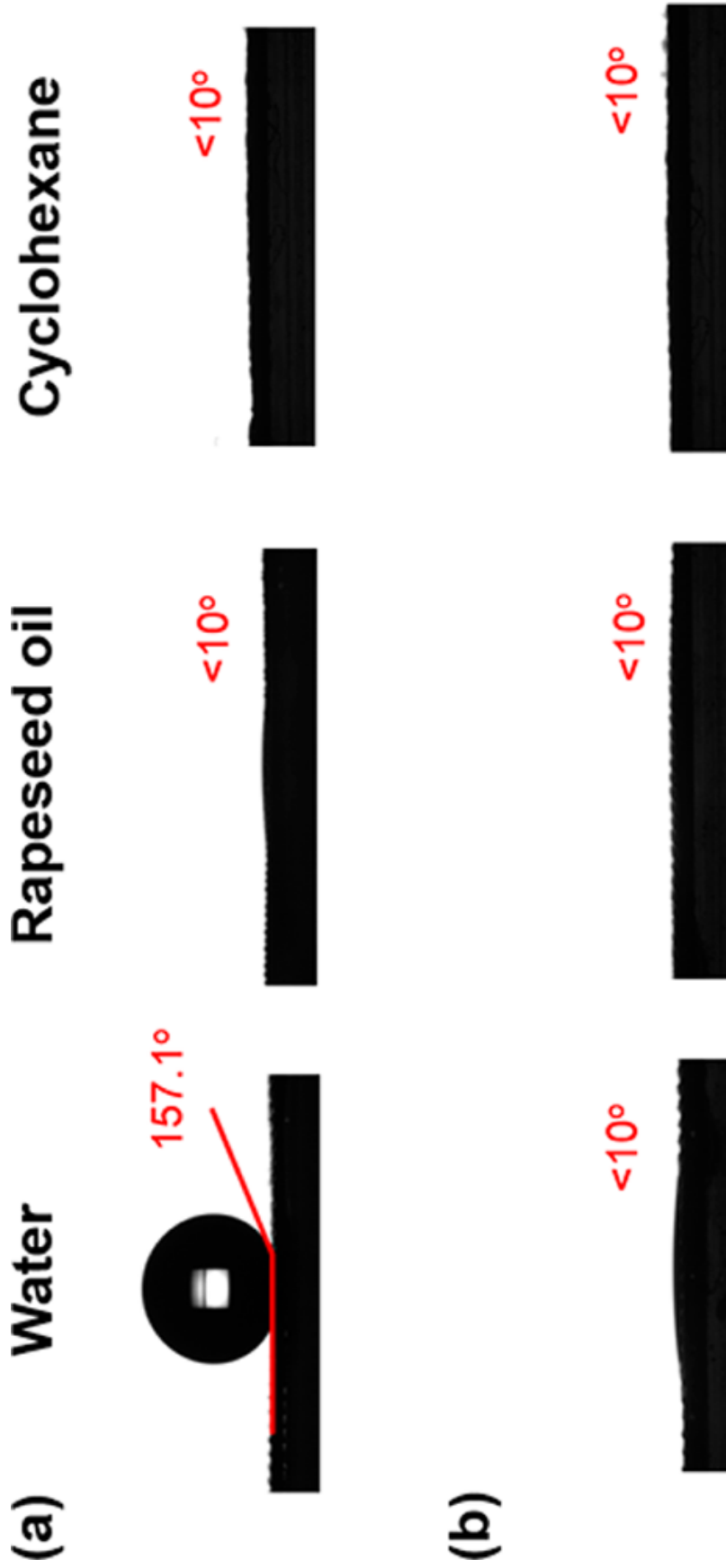


Figure 3.12 Optical images of water, rapeseed oil, and cyclohexane droplets on (a) TDP-coated and (b) noncoated aluminum mesh with triple-pore morphology.

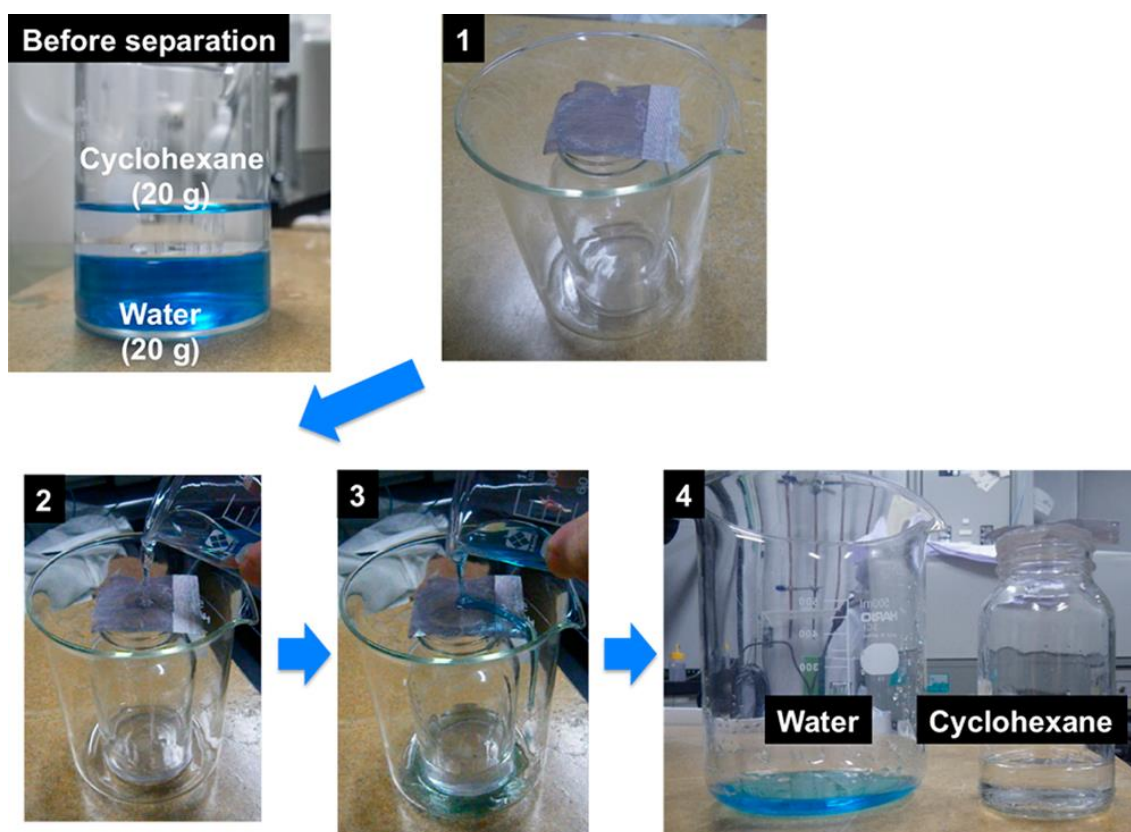


Figure 3.13 Optical images of oil/water separation test using TDP-coated aluminum mesh. Water was dyed with methylene blue.

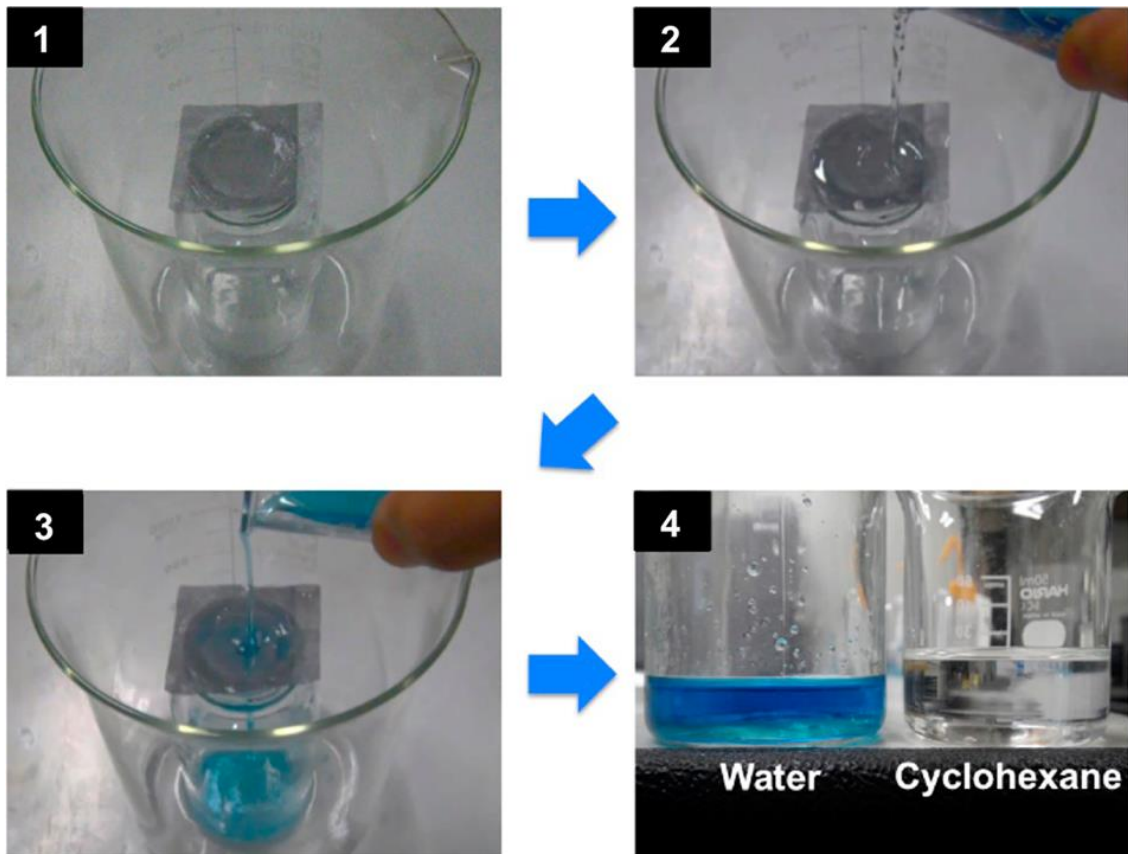


Figure 3.14 optical images of oil/water separation test using triple-pore hierarchical aluminum mesh wetted with water. Water in the mixture was dyed with methylene blue.

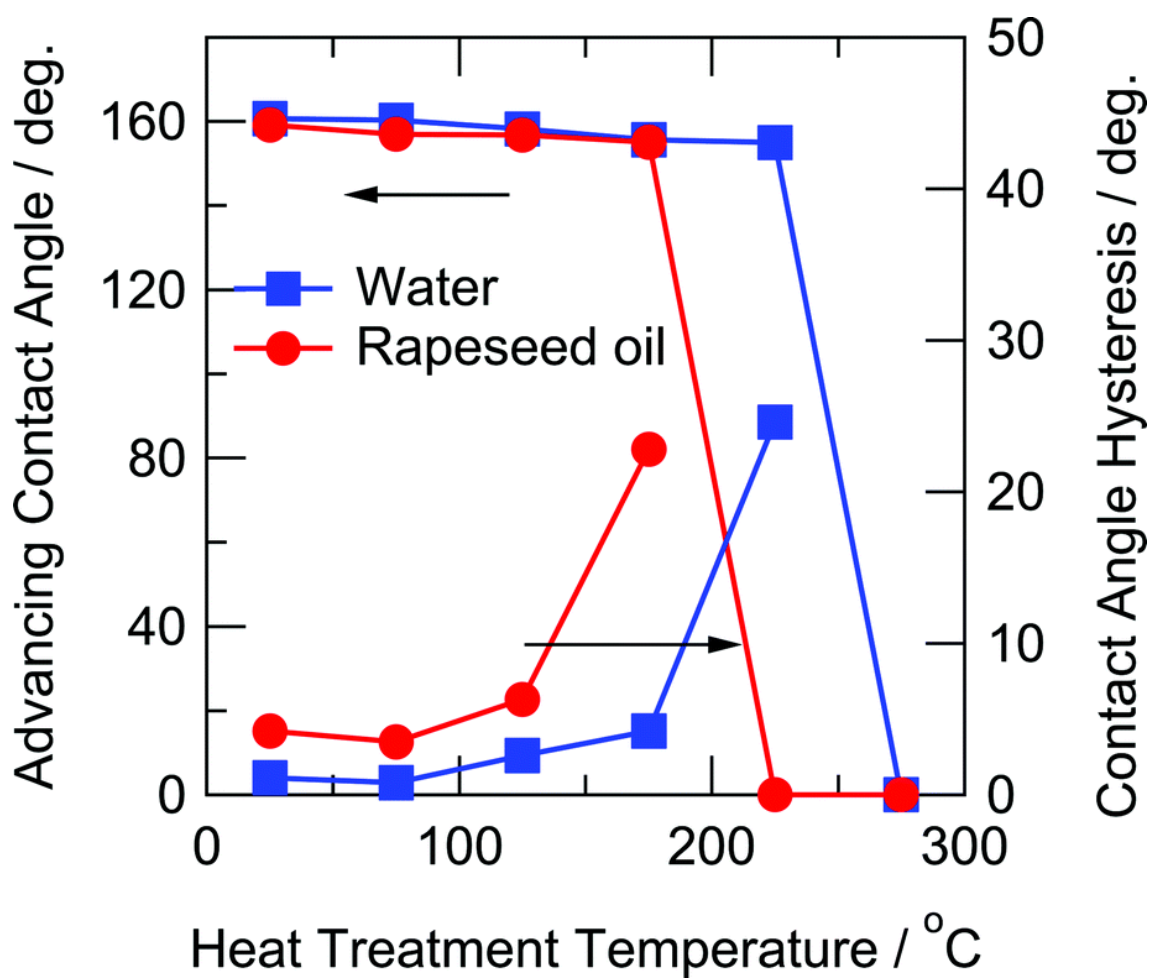


Figure 3.15 Change in the advancing contact angle and contact angle hysteresis for water and rapeseed oil of the FAP-coated dual-pore hierarchical surface, chemically etched in solution containing 1 mol dm^{-3} HCl, anodized and pore-widened for 1200 s, with heat treatment temperature.

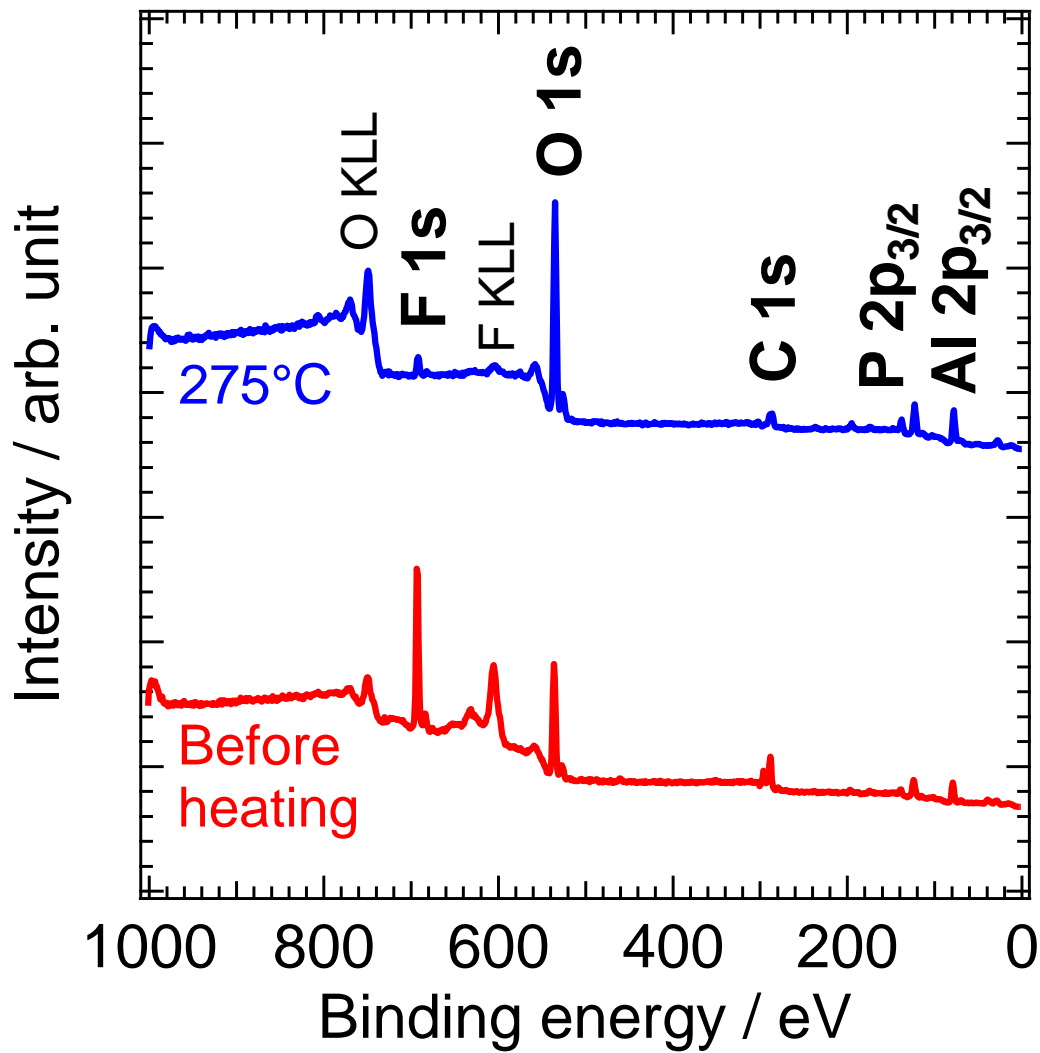


Figure 3.16 XPS wide scan spectra of superoleophobic hierarchical aluminum plate before and after heat treatment at 275°C.

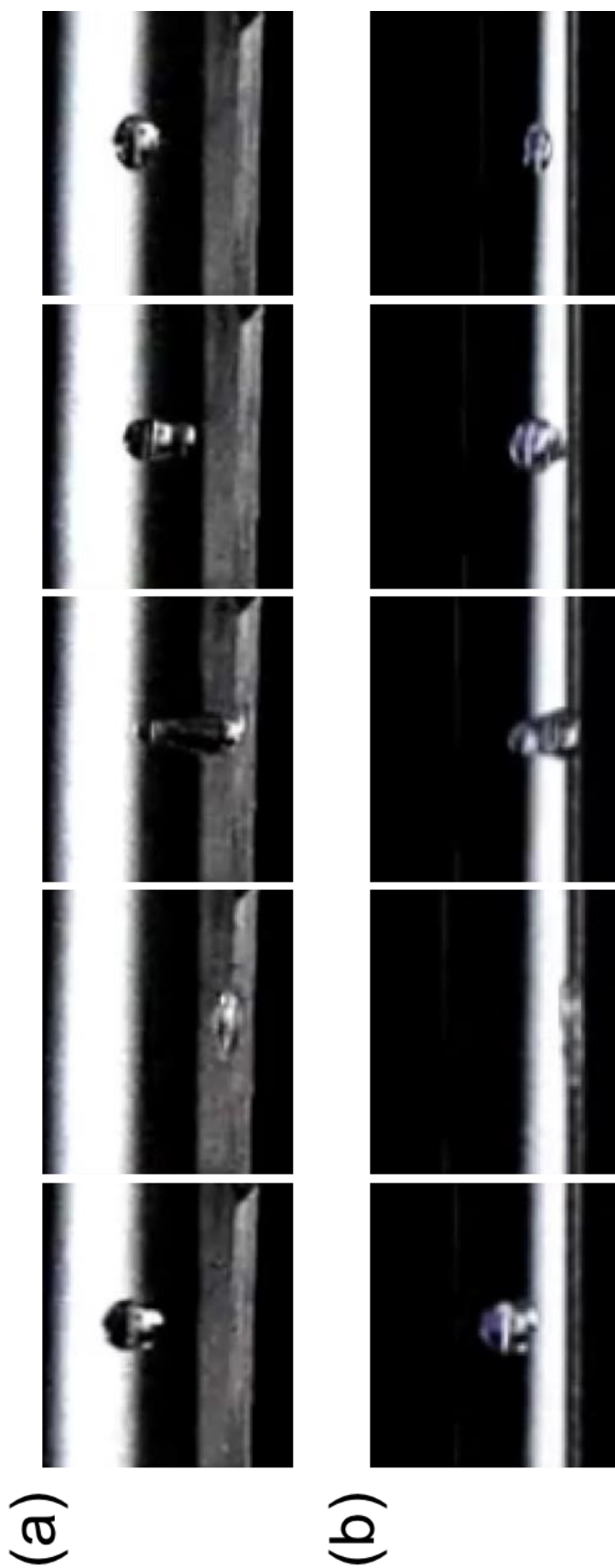


Figure 3.17 Digital photographs showing bouncing (a) water and (b) dodecane droplets falling on the super-repellent aluminum surface formed by etching in 0.2 mol dm⁻³ CuCl₂ and 1 mol dm⁻³ HCl, anodizing, and pore widening for 1200 s.

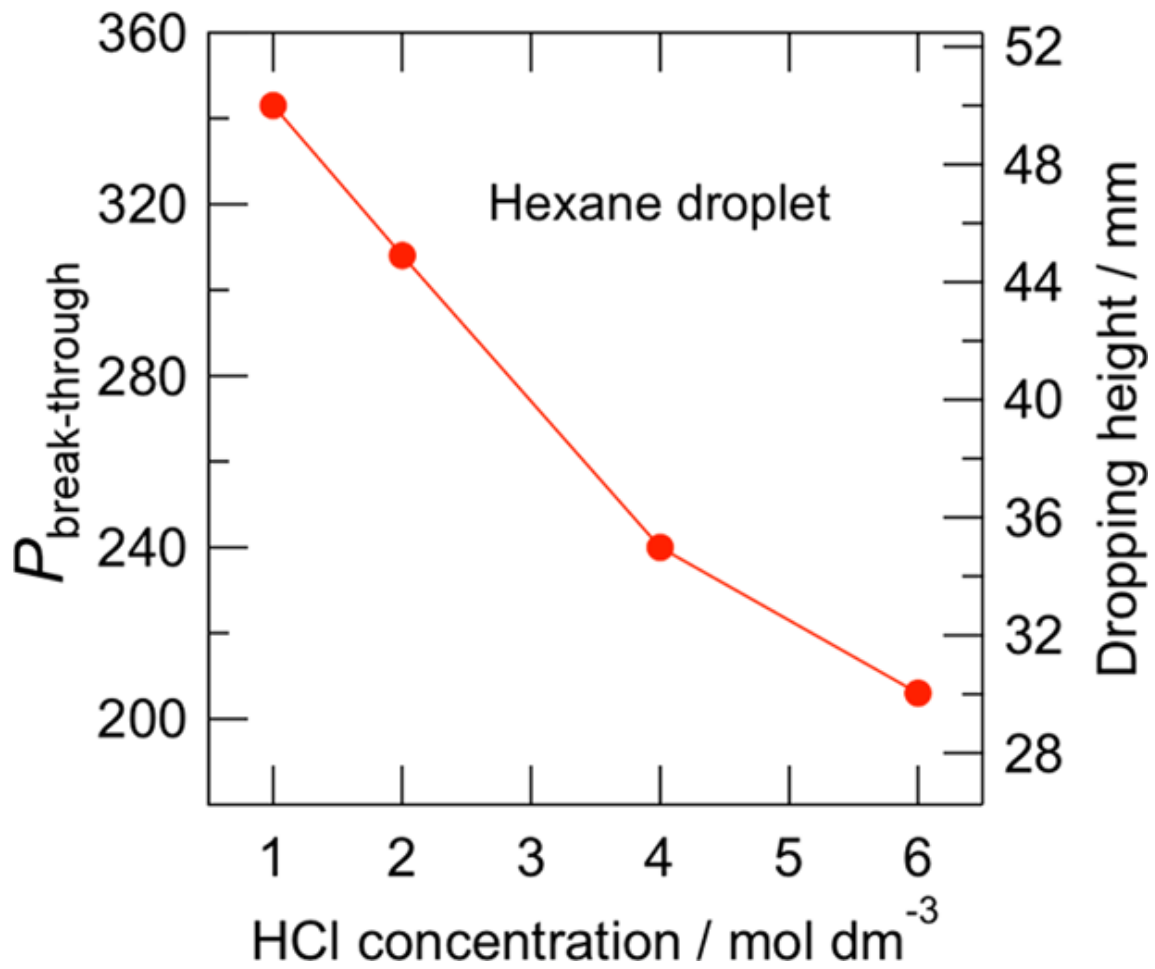


Figure 3.18 Breakthrough pressure for hexane on the FAP-coated aluminum mesh with triple-pore morphologies as a function of HCl concentration (the size of etch pits) in the chemical etching solution.

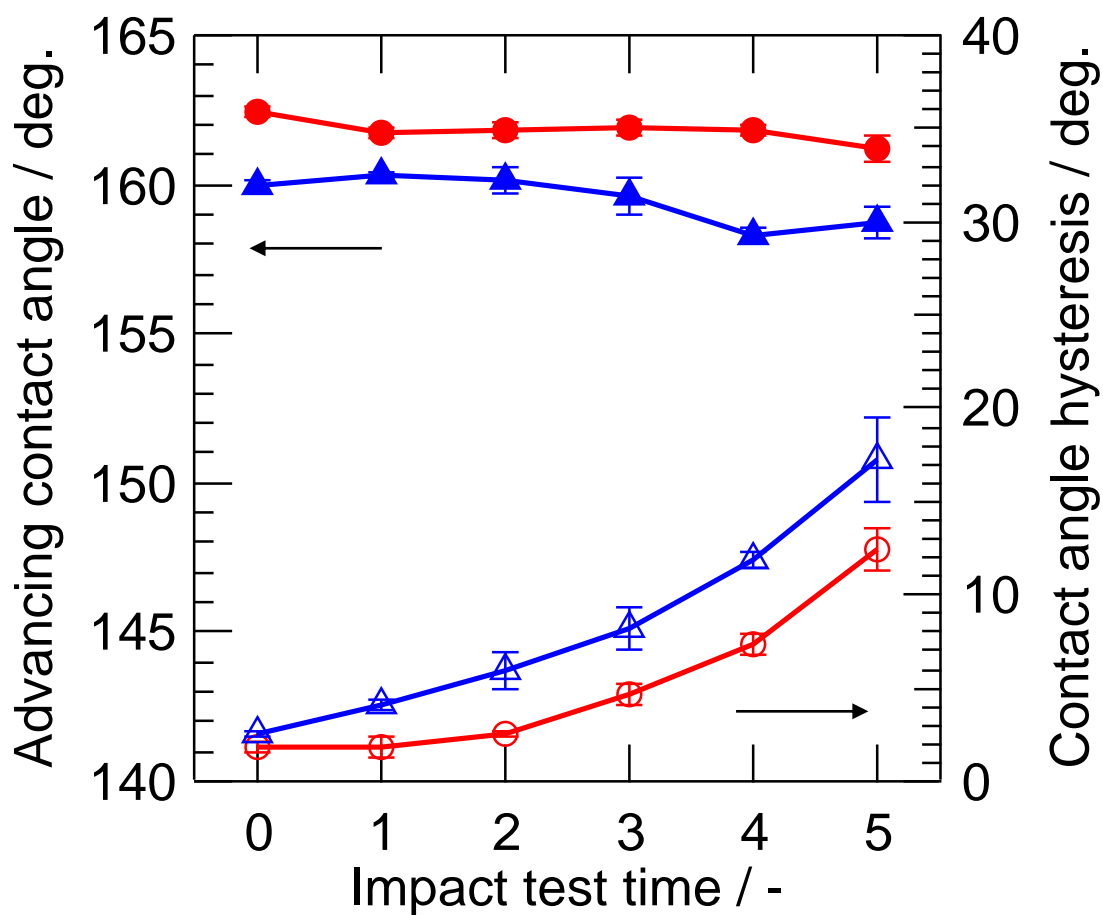


Figure 3.19 The change in the advancing contact angle and contact angle hysteresis for (●, ○) water and (▲, △) hexadecane as a function of dropping number of glass beads (50 g and ~20,000 beads per cycle) of the dual-pore hierarchically rough aluminum plate surface.

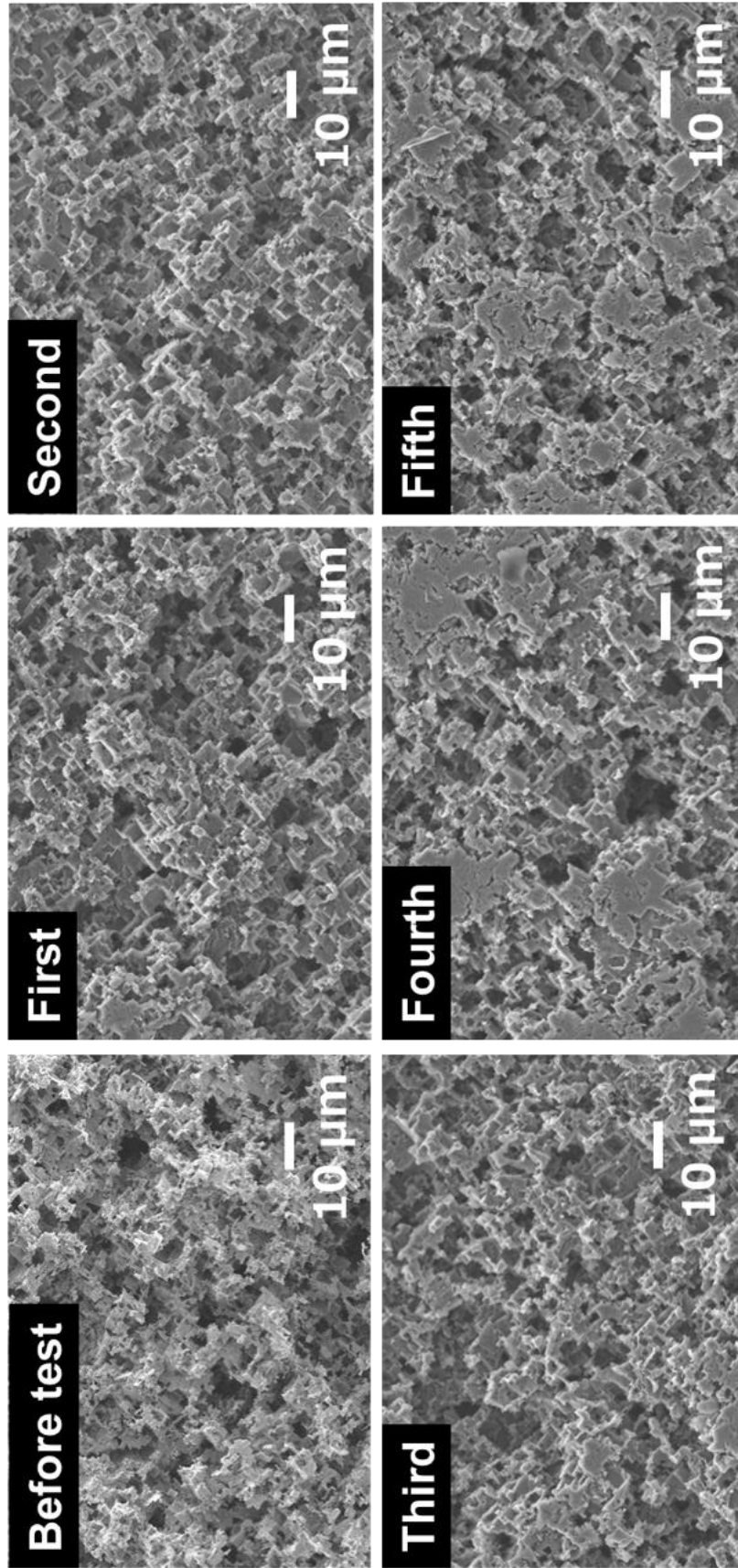


Figure 3.20 Scanning electron micrographs of hierarchical dual-pore aluminum surface after 0-5 times of glass beads dropping test (50 g).

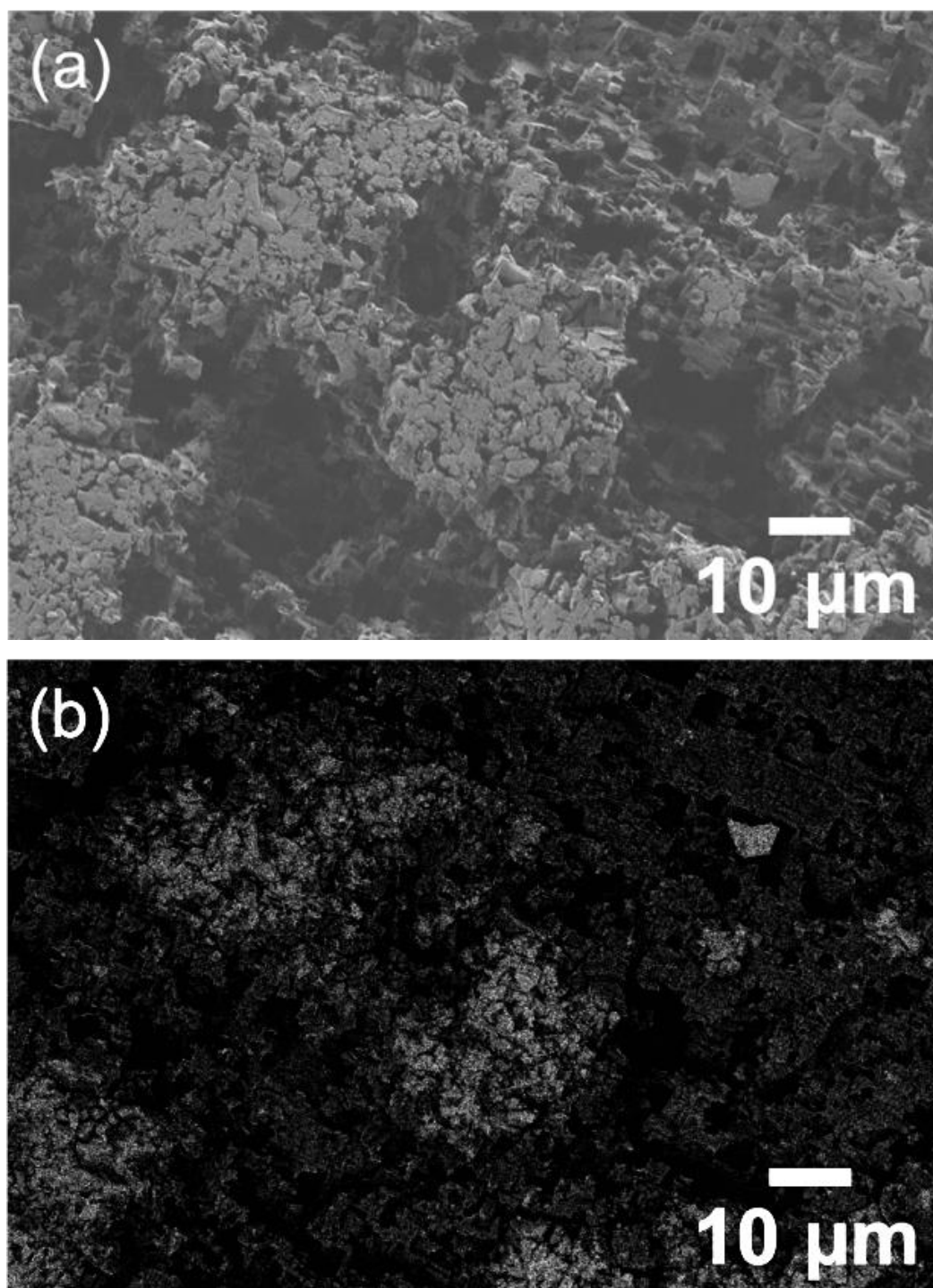


Figure 3.21 (a) Second-electron and (b) back-scattered electron SEM images of after dropping beads (50 g) 5 times.

Chapter 4

Self-healing Properties of Superoleophobic Hierarchically Rough Aluminum Surface

4.1 Introduction

As described in previous chapters, the author fabricated superoleophobic aluminum surface by a combination of chemical etching, anodizing, pore widening and fluoroalkyl monolayer coating. However, such super-liquid-repellent surfaces have low durability because of low mechanical stability of the thin organic coating and highly rough hierarchical surfaces. The degradation of organic coatings is critical issue for practical applications of super-liquid-repellent surfaces.

The introduction of self-healing nature to superoleophobic surface is of recent interest [1-5]. Wang et al. designed self-healing superoleophobic aluminum by utilizing the nanopores formed by anodizing of aluminum as a “nanoreservoirs” of healing agent [5]. The superoleophobicity was healed by the transportation/enrichment of low-surface-energy materials trapped in the nanoreservoirs to the outmost surface, which is thermodynamically driven by minimizing the surface tension. In accord with this report, it is important that how much low-surface-energy materials can be infiltrated into nanoreservoirs. In order to obtain the sufficient self-healing property, the factors influencing the self-healing behavior should be understood.

Herein, the author infiltrated a liquid healing agent into the nanoreservoirs for self-healing of damaged organic coating on the hierarchically rough aluminum surface, as schematically illustrated in Fig. 4.1. The effect of morphological factors, such as nanopore diameter and length, on the self-healing behavior was also discussed in this chapter.

4.2 Experimental

4.2.1 Formation of nanoporous surfaces

For fundamental understanding the role of the morphology of nanopores channels on self-healing ability, cylindrical nanopores channels of different diameters and lengths were formed by anodizing of electropolished aluminum under the different conditions. The nanoporous alumina films were formed on aluminum plate (99.999% purity) by anodizing in 0.3 mol dm^{-3} sulfuric or phosphoric acids at a constant voltage of 25 or 120 V, respectively, at 288 K for various periods of time. Prior to anodizing, the aluminum plate was electropolished in solution containing perchloric acid and ethanol (1:4, v/v) at a constant voltage of 20 V for 5 min below 278 K. As described in Chapter 1, the nanopore diameter proportionally increases with the anodizing voltage [6, 7], but high anodizing voltage exceeding 100 V cannot be applied in sulfuric acid electrolyte because of burning phenomenon. To form an anodic film with a large pore diameter, phosphoric acid was used as electrolyte in addition to sulfuric acid.

4.2.2 Formation of dual-pore hierarchically rough surface

High-purity aluminum plate (99.999%) of 0.5 mm thickness was used as a substrate. Prior to chemical etching, pre-treatment was carried out for the aluminum plate in 1 mol dm^{-3} NaOH solution at 333 K for 120 s and subsequently in 1 mol dm^{-3} HNO₃ at 333 K for 180 s to remove a native oxide layer. Chemical etching was carried out by immersing the plate in a mixture of 0.2 mol dm^{-3} CuCl₂ and 1 mol dm^{-3} of HCl at 298 K for a 6 min. After chemical etching, specimen was rinsed with concentrated HNO₃ to

remove the copper deposited on the surface. Then, the etched aluminum specimen was anodized in $0.3 \text{ mol dm}^{-3} \text{ H}_2\text{SO}_4$ at a constant voltage of 25 V for 1200 s at 288 K. Subsequently, the size of the nanopores in the anodic alumina layer was controlled by the subsequent pore widening treatment in 5 wt% H_3PO_4 at 303 K for suitable time.

4.2.3 Organic monolayer coating and infiltration of low-surface-tension molecules in nanopores

An organic self-assembled monolayer was coated on the specimens by immersing in ethanol containing 1 mmol dm^{-3} 1H,1H,2H,2H-perfluorodecyl phosphonic acid (FDPA) for 24-48 h at room temperature after cleaning the anodized specimens using a plasma cleaner (Harrick Plasma Co., PDC-32G), by which a contaminant hydrocarbon layer was removed from the surfaces. Then, in order to infiltrate the low-surface-tension molecules, specimens were immersed in hexane containing 20 vol% 1H,1H,2H,2H-perfluorodecyltriethoxysilane (FAS) for 1 min at room temperature. The FAS is liquid at room temperature.

4.2.4 Characterizations

Before and after infiltration of FAS, the elemental depth profile analysis of the specimens were performed by glow-discharge optical emission spectroscopy (GDOES) using a Jobin Yvon 5000 RF (HORIBA Ltd.) instrument in a neon atmosphere of 1100 Pa by applying a power of 35 W. Light emissions of characteristic wavelength were monitored throughout the analysis with a sampling time of 0.01 s to obtain depth profiles.

The wavelength of the spectral lines used were shown in Table 4.1. The signals were detected from a circular area of approximately 4 mm diameter. The morphological images were taken by field emission scanning electron microscope (FE-SEM, JEOL Ltd., JSM-6500F) operated at 10 kV.

Table 4.1 The wavelength of the spectral lines for GDOES analysis

Elements	H	C	O	F	Al	P	Si
Wavelength (nm)	121.567	165.701	130.217	685.601	396.152	178.287	288.158

4.2.5 Wettability evaluations

Surface wettability was evaluated by static contact angle measurements for water or hexadecane (4 μ L) using an optical contact angle meter (Kyowa Interface Science Co., DM-CE1). Self-healing property was evaluated by static and dynamic contact angle measurements immediately after irradiation of O₂ plasma for 2 min and also after subsequent air exposure in the atmosphere at room temperature for a suitable period of time.

4.3 Results and discussion

4.3.1 The effect of anodic nanopore diameter on the self-healing property

Fig. 4.2 shows the surface and cross-sectional SEM images of the aluminum plate anodized in sulfuric and phosphoric acids. Numbers of nanopores with diameters approximately 40 nm or 160 nm were formed on entire surfaces anodized in sulfuric and phosphoric acids, respectively. The thickness of the anodic films were both approximately 3 μm . Thus, the porous anodic alumina films with different diameters and same thickness were formed.

Fig. 4.3 shows the effect of nanopore diameter on the self-healing property. The static contact angle for a water droplet was approximately 130° after FDPA coating and subsequent infiltration of FAS in nanopores. This value is similar to that before FAS infiltration. The irradiation of O_2 plasma for 2 min changed the surface to hydrophilic with the contact angles less than 10° on both surfaces. However, the water contact angles increased during air exposure for longer than 1 h, when the FAS was infiltrated in the nanopores. In contrast, no recovering of the contact angle occurs without FAS infiltration. Thus, the recovering of the contact angle is associated with the FAS infiltration into the nanopores. Fig. 4.3 also shows that the recovering contact angle after air exposure is dependent upon the pore size. The contact angle increased to the original level ($\sim 130^\circ$) on the surface anodized in sulfuric acid (small nanopores) within 1 h, while the recovering only to 63° occurs for the specimen anodized in phosphoric acid (large nanopores) even after air exposure for 8 h.

To elucidate the pore-size-dependent self-healing properties, the amount of the infiltrated FAS was estimated from the GDOES depth profile analysis. Fig. 4.4a shows GDOES elemental depth profiles of FAP-coated hydrophobic porous alumina film with smaller nanopores before and after storage of FAS molecules in nanopores. After FAS infiltration, the intensities of carbon, fluorine and silicone derived from FAS increased, indicating the presence of FAS molecules in the nanopores. Similar depth profiles were obtained for the specimen with larger pores, but the intensities of elements (C, Si, P and F) derived from FDPA and FAS were rather low compared with those with the smaller pores (Fig. 4.4b). The reduced intensities for the specimen with the larger pores are associated with the lower surface area. From the number density of nanopores, the diameter and length of nanopores, obtained from the SEM observations (Figs. 4.2), the surface area was roughly estimated. The surface area estimated for the smaller-pore specimen is approximately 3.2 times that for the larger one. This value is close to the ratio of the integrated fluorine (3.6) and phosphorous (3.4) intensities of GDOES depth profiles for the smaller-pore specimen relative to those for the larger-pore one before FAS infiltration. Therefore, the amount of FAS infiltrated into the nanopores is almost proportional to the area of pore wall surface, not the pore volume, since the pore volumes of these two specimens are similar.

Fig. 4.5 illustrates the self-healing process. The FAS may be present by coating pore walls as well as storing at the pore bottom, from the GDOES depth profiles, with the former amount probably predominant. As a consequence, the healing durability is enhanced with an increase in the surface area of the pore walls. The liquid FAS is likely

transported to the damaged surface along with the pore wall because of a good affinity of FDPA surface and FAS, both of which have a fluoroalkyl moiety. The evaporation of FAS may also contribute to the healing of the damaged surface.

Fig. 4.6 shows the GDOES elemental depth profiles of the FAS-infiltrated specimens before and after O₂ plasma irradiation. Obviously, the intensities of fluorine and carbon at the outermost surface decreases after the plasma irradiation, contributing to the transition of the surface to hydrophilic. However, the intensities of all the elements examined remain almost unchanged by the plasma irradiation. The FAS in the nanopores appear not to be damaged by the plasma.

4.3.2 The effect of nanopore length on the self-healing behavior

Fig. 4.7 shows the surface and cross-sectional SEM images of porous anodic alumina with several film thicknesses (i.e. nanopore length) formed in 0.3 mol dm⁻³ sulfuric acid electrolyte at a constant voltage of 25 V. The surface image shown in Fig. 4.7a is an example of alumina surfaces after anodizing and pore widening, which displayed numbers of small nanopores with a diameter of 40 nm. The diameter was controlled to this value for all the specimens with different film thicknesses. The cross-sectional SEM images disclose the change in the film thickness from 0.5 to 9 μm with anodizing time (Figs. 4.7b-f). Thus, porous specimens with same nanopore diameter and different pore lengths were fabricated.

Fig. 4.8a shows the effect of nanopore length (porous film thickness) on the self-healing behavior. All the FAS-infiltrated specimens are hydrophobic with a contact angle

of approximately 130°. Again, the O₂ plasma irradiation for 2 min decreased the water contact angle to lower than 10°, but all the FAS-infiltrated specimens showed self-healing behavior; the water contact angles increased within 1 h. There was little dependence of nanopore length on the self-healing property for the specimens with pore length of 1.5-9 µm and the contact angles were almost completely recovered to the original value. Only the specimens with a pore length of 0.5 µm showed limited recovering of the contact angle (~110°). The lower amount of FAS infiltrated in the shorter nanopores may be the reason for the limited recovering. The recovering of the contact angle for the specimen with the nanopores of 160 nm in diameter and 3 µm thickness is lower than that of 40 nm in diameter and 0.5 µm thickness. Since the surface area of the former specimen is 1.7 times that of the latter specimen, it is likely that the former larger surface area of the nanopores contributes to the better recovering.

The repeatability of self-healing hydrophobicity was also examined. The results are shown in Fig. 4.8b. When the cycle of 1) O₂ plasma irradiation for 2 min and 2) air exposure in the laboratory atmosphere at room temperature for longer than 1 h was repeated, all the specimens with different pore lengths showed similar recovering of the contact angle to >120°. However, lower recovering contact angles are obtained for the specimens with shorter nanopore lengths at cycles higher than 3. Thus, longer nanopores, which can infiltrate larger amounts of FAS, are preferable for better self-healing durability.

4.3.3 The self-healing superoleophobicity using dual-pore hierarchically rough aluminum surface

The author also examined the self-healing property of the dual-pore hierarchically rough superoleophobic aluminum surface. Compared with the specimens used in Chapter 3, the etched aluminum was anodized for 1200 s to form longer nanopores to ensure the longer healing cycles in accord to the results obtained above. Figs. 4.9 shows SEM images of the hierarchical dual-pore aluminum surface fabricated by wet processes including chemical etching, anodizing and pore widening. It was confirmed that numbers of micrometer-scale etch pits and nanopores were formed on the surface. As described in the previous chapters, the surface with this morphology can be superoleophobic after fluoroalkyl organic coating. Fig. 4.10 shows the self-healing property of the superoleophobic dual-pore hierarchical aluminum specimen. After O₂ plasma irradiation, the superoleophobic surface changed to superoleophilic as well as Fig. 4.3 and 4.7a. However, the contact angle and contact angle hysteresis were recovered to the original level (~160° and ~5°), respectively, during air exposure for 1 h at room temperature. A hexadecane droplet (5 μL) was readily rolled off the surface with a sliding angle of <5° after FDPA coating, as displayed in Fig. 4.11a. However, a hexadecane droplet quickly spread on the surface as soon as contact, changed from superoleophobic to oleophilic after O₂ plasma irradiation for 2 min due to FDPA decomposition (Fig. 4.11b). After subsequent air exposure for >1 h, the superoleophobicity regenerated with a sliding angle of <5°, which is the original level, resulting in the self-healing property (Fig. 4.11c). In

addition, the cycle of this wettability transition can be repeatable even eight times, as shown in Fig. 4.12.

As discussed in 4.1, self-healing superoleophobicity using hierarchically rough anodized aluminum surface was reported by Wang et al [5]. They used infiltrated perfluorooctanoic acid for healing agent and self-healing was confirmed by heating the damaged specimen at room temperature, but healing time of nearly 40 h was required. The healing was accelerated by heating at 70°C and the healing time was reduced to 6 h. Much shorter healing time of ~1 h is obtained even at room temperature in the present study using the infiltrated FAS as a healing agent. In addition to the morphology, the selection of healing agent is of importance for self-healing of the superoleophobicity under the exposed conditions of the materials.

4.4 Conclusions

In this chapter, the effect of geometrical factors on the self-healing property of the FDPA-coated rough aluminum surfaces with infiltrated FAS molecules for liquid repellency was examined. The self-healing behavior is influenced by the diameter and length of cylindrical nanopores; smaller and longer nanopores are suitable for durable self-healing. The nanopores surface area, not pore volume, appears to be a controlling factor of the self-healing properties. The FAS-infiltrated superoleophobic hierarchically rough aluminum surface shows completely self-healing superoleophobicity. The O₂ plasma treatment changes the surface from superoleophobic to superoleophilic with a

contact angle close to 0° for hexadecane as well as water. The simple air exposure for >1 h is sufficient to recover the superoleophobicity. Thus, the FAS infiltration is a suitable method to provide self-healing nature to the superoleophobic dual-porous hierarchical surfaces.

References

- [1] Y. Li, L. Li, J. Sun, *Angew. Chem. Int. Ed.* **122**, 6265 (2010).
- [2] H. Wang, Y. Xue, J. Ding, L. Feng, X. Wang, T. Lin, *Angew. Chem. Int. Ed.* **50**, 11433 (2011).
- [3] H. Zhou, H. Wang, H. Niu, A. Gestos, T. Lin, *Adv. Funct. Mater.* **23**, 1664 (2013).
- [4] K. Golovin, M. Boban, J. M. Mabry, A. Tuteja, *ACS Appl. Mater. Interfaces* **9**, 11212 (2017).
- [5] X. Wang, X. Liu, F. Zhou, W. Liu, *Chem. Commun.* **47**, 2324 (2011).
- [6] S. Ono, *J. Vac. Soc. Jpn.* **52**, 637 (2009).
- [7] W. Lee, S. Park, *Chem. Rev.* **114**, 7487 (2014).

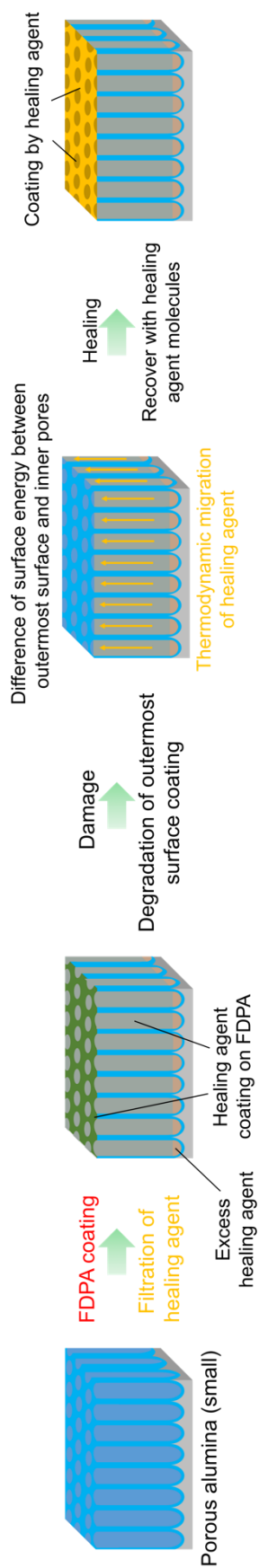


Figure 4.1 Schematic illustration showing the self-healing property by infiltration the low-surface-energy material in anodized nanopores.

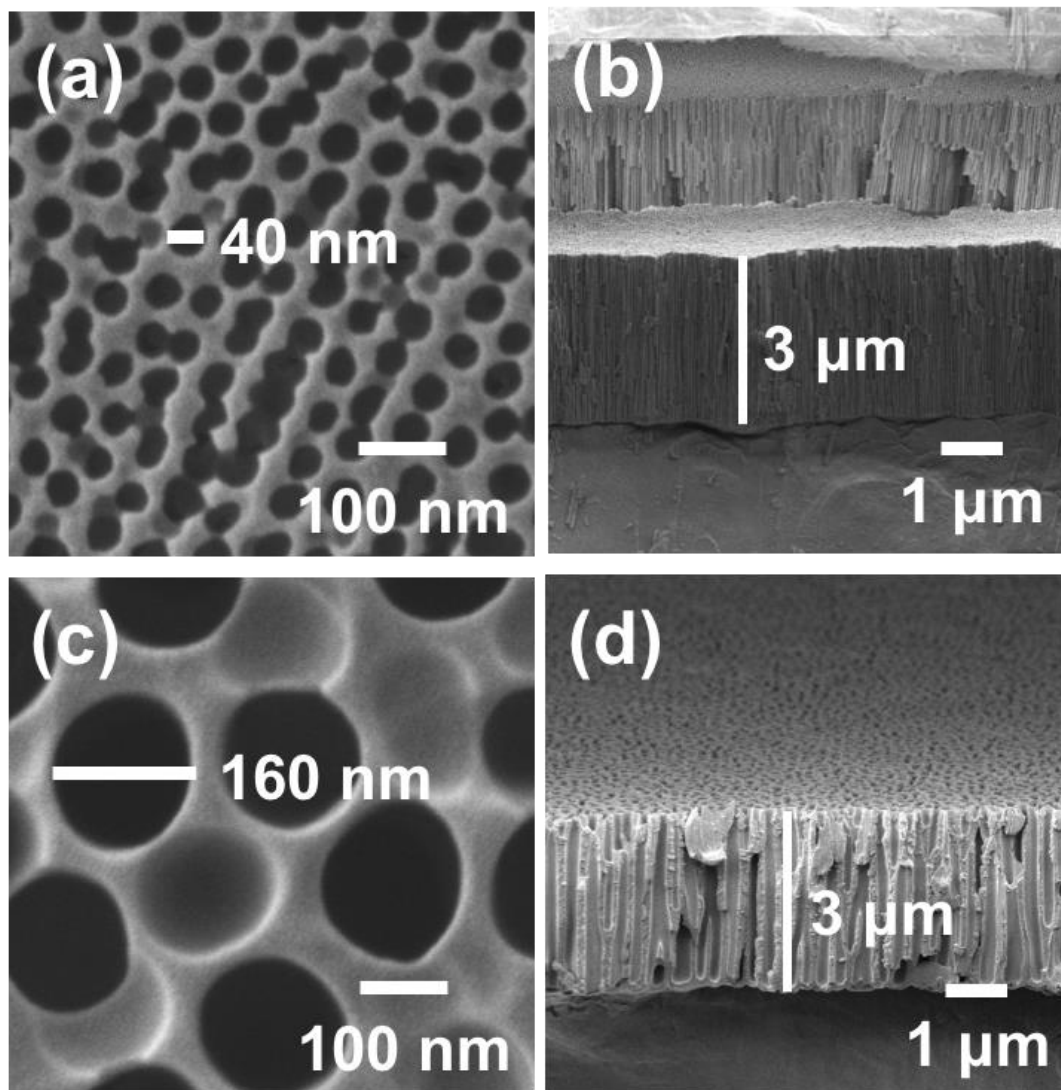


Figure 4.2 (a, c) Surface and (b, d) cross-sectional SEM images of porous alumina films anodized in 0.3 mol dm^{-3} (a, b) sulfuric or (c, d) phosphoric acids at constant voltages of 25 or 120 V for 20 or 60 min and then pore-widened in 5 wt% phosphoric acid for 20 or 60 min at 303 K, respectively.

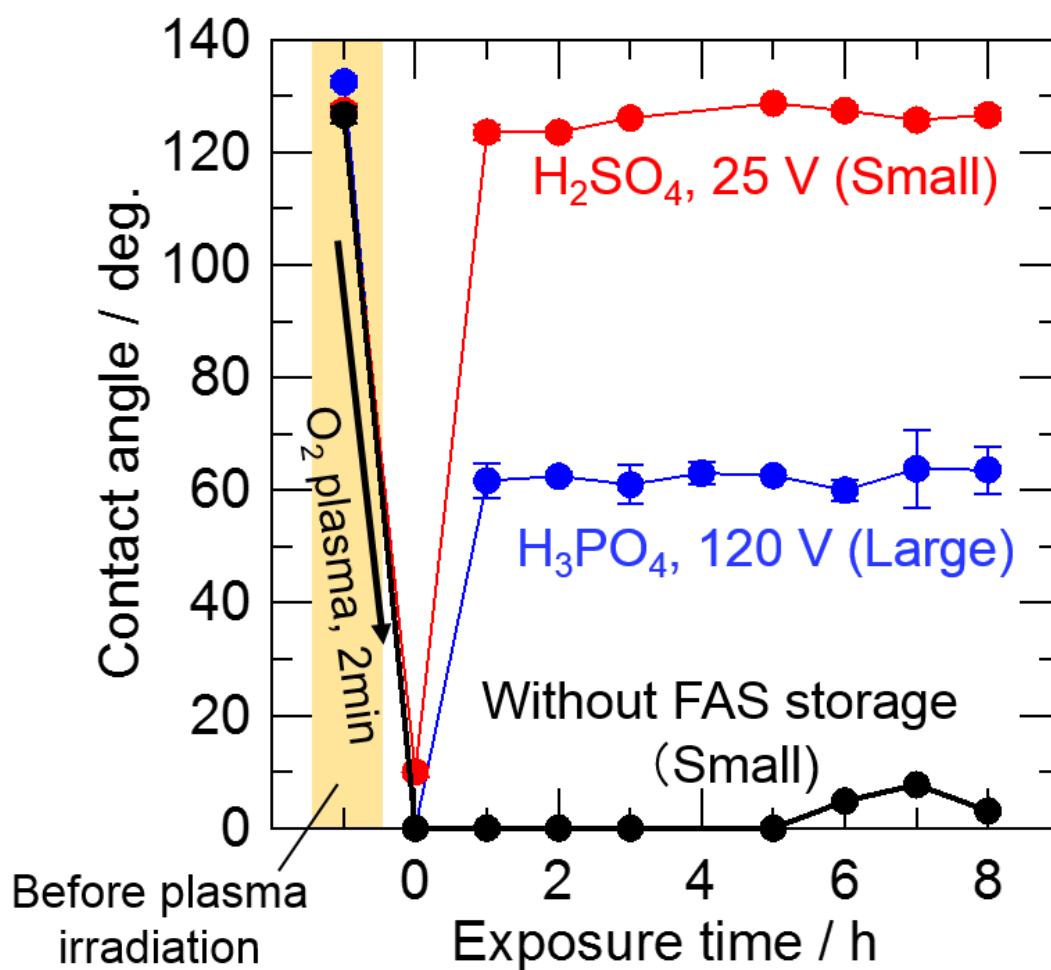


Figure 4.3 Self-healing behavior on porous alumina surfaces anodized in (red) sulfuric (small) or (blue) phosphoric acids (large). (black) Change in the water contact angle on the surface with small nanopores after O₂ plasma irradiation and air exposure without infiltration excess FAS molecules in nanopores.

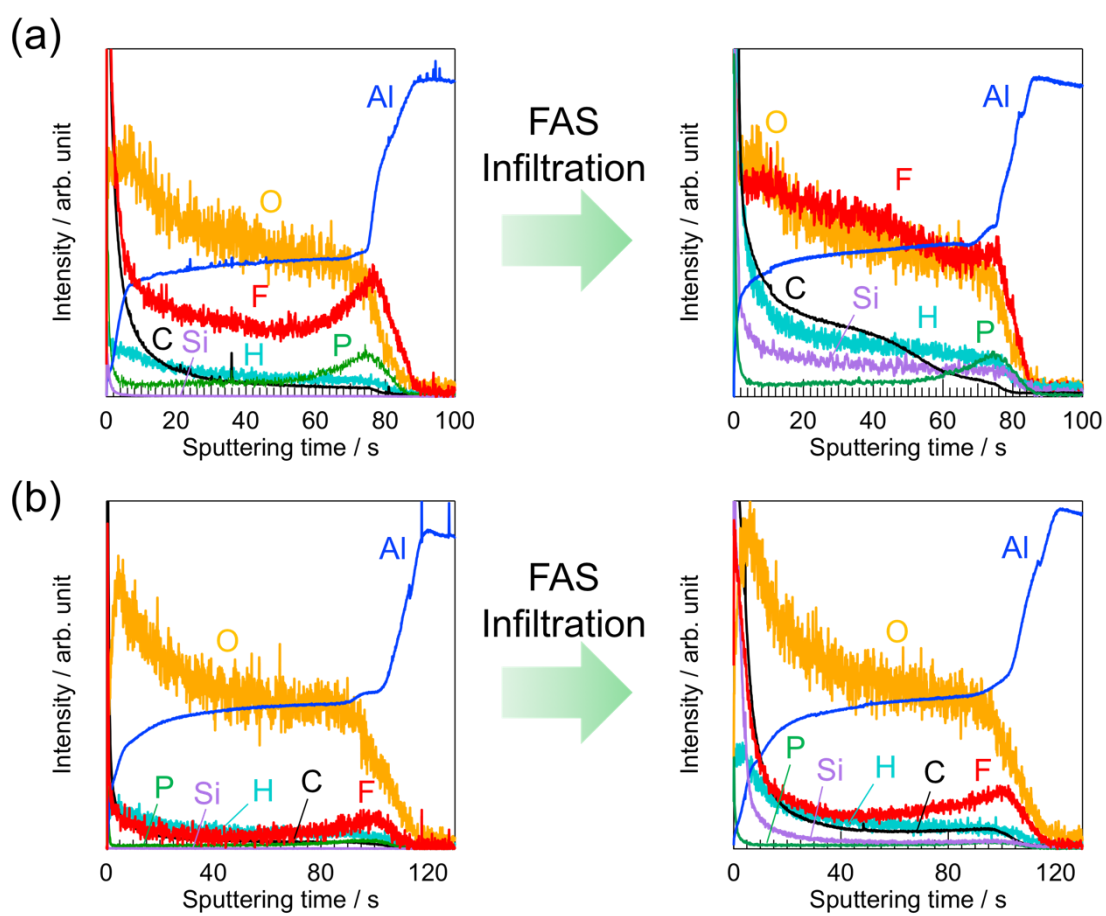


Figure 4.4 GDOES elemental depth profiles before and after infiltration excess FAS for porous alumina with (a) small and (b) large nanopores.

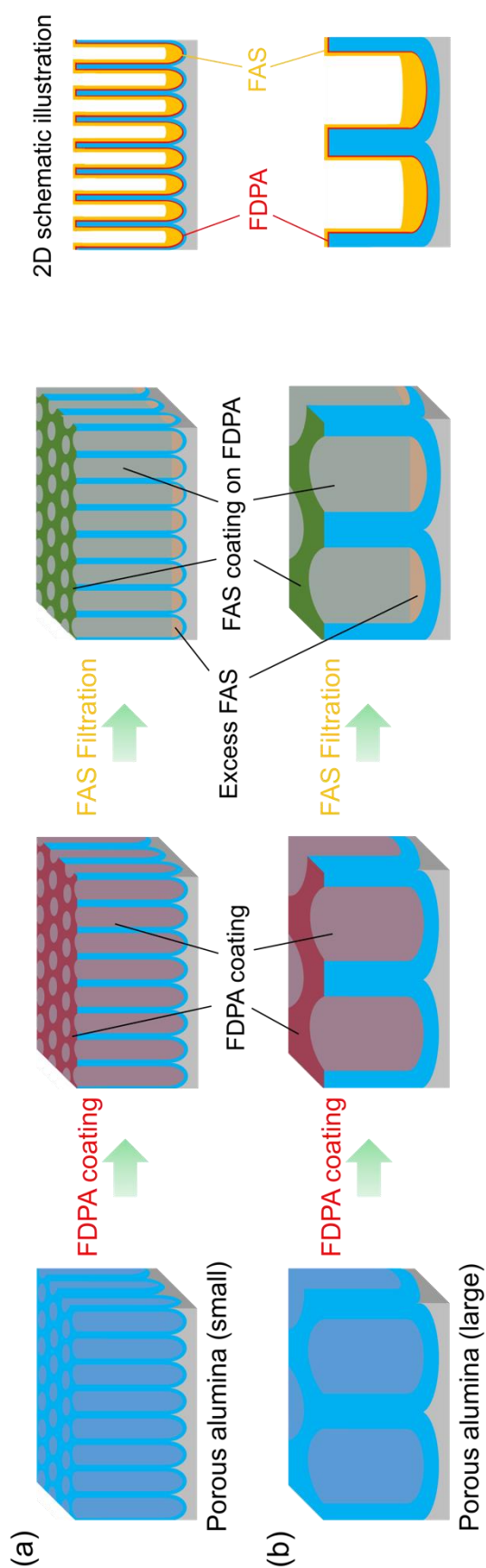


Figure 4.5 Schematic illustration showing FDPA-coated porous surfaces with (a) small or (b) large nanopores before and after infiltration of FAS along nanopore walls.

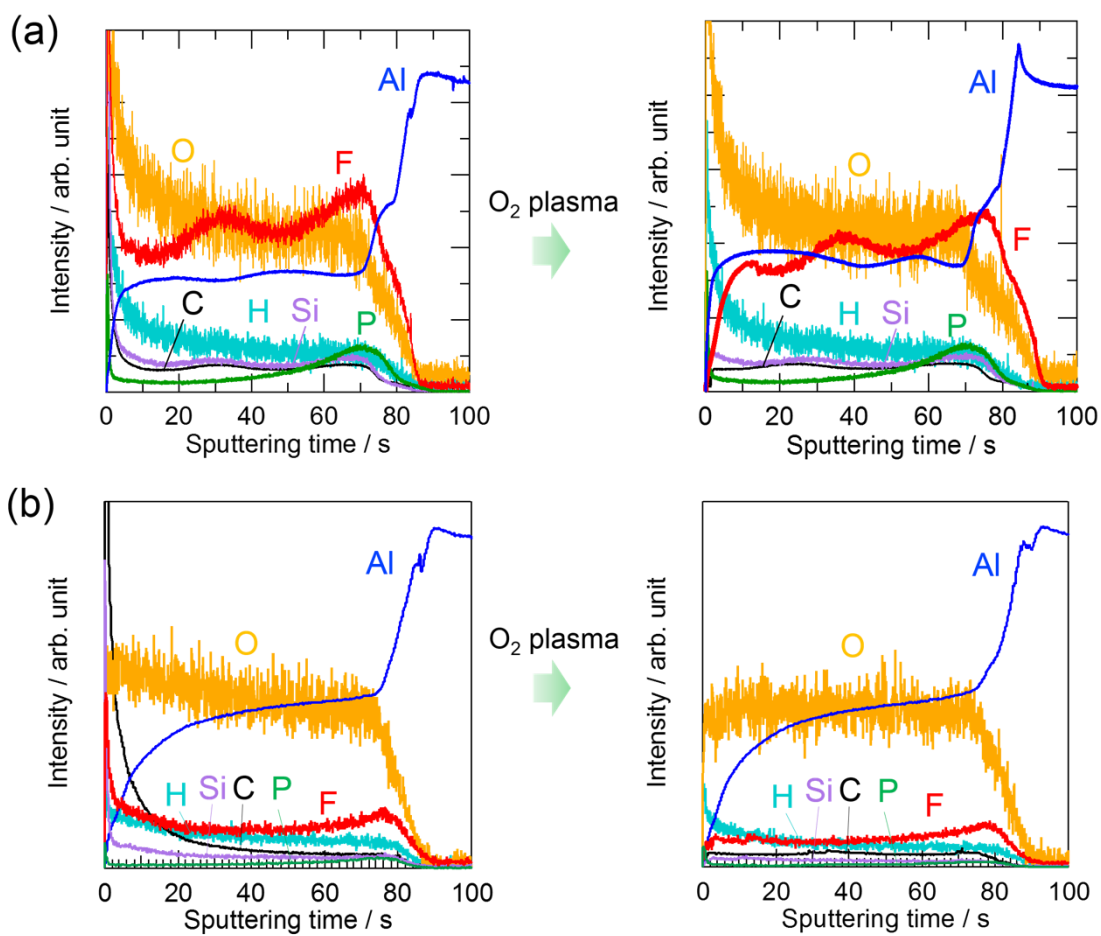


Figure 4.6 GDOES elemental depth profiles of porous alumina specimens with (a) small and (b) large nanopores infiltrated excess FAS before and after O₂ plasma irradiation.

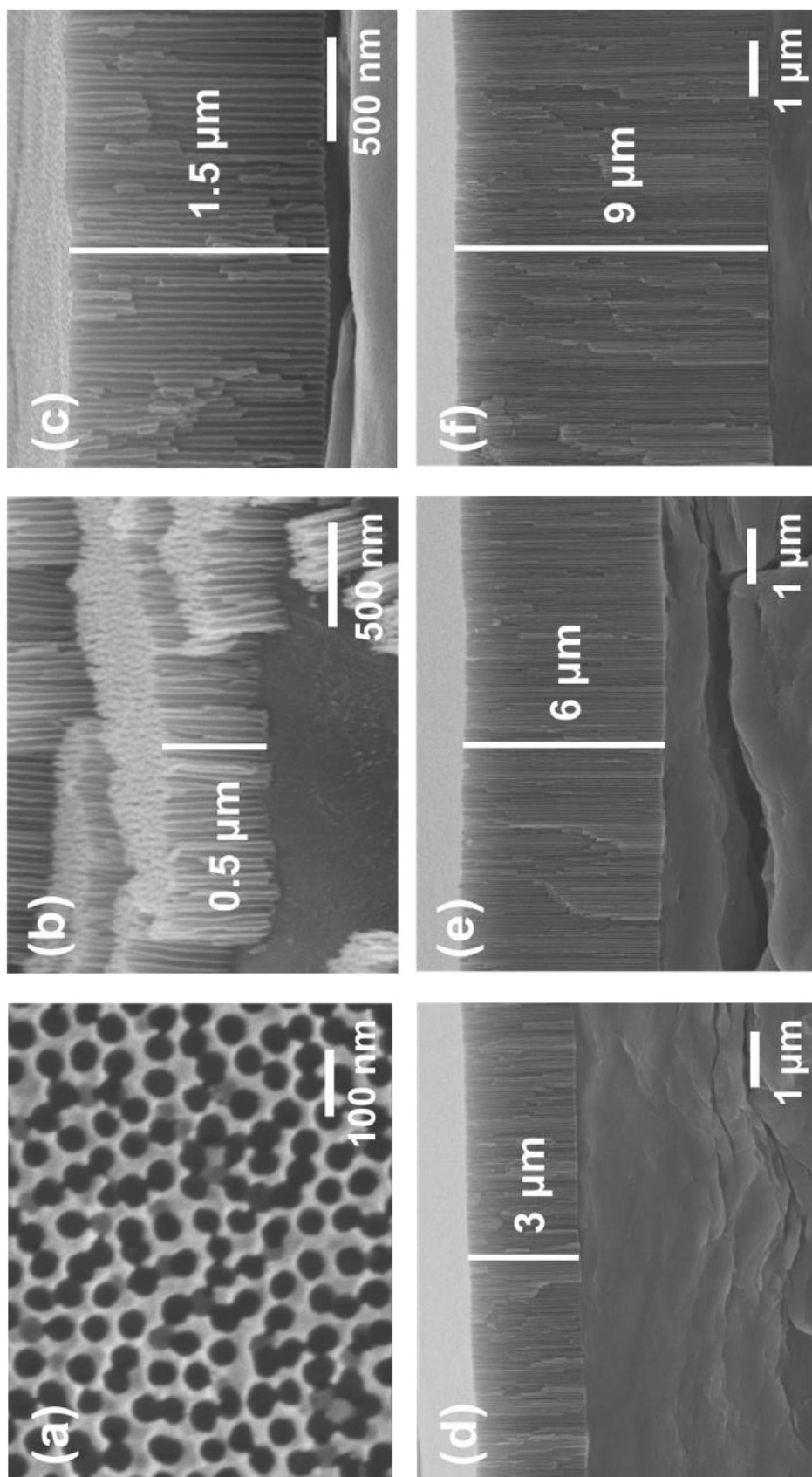


Figure 4.7 (a) surface and cross-sectional SEM micrographs of porous alumina films formed by anodizing in 0.3 mol dm^{-3} sulfuric acid electrolyte at a constant voltage of 25 V for (b) 3, (c) 10, (d) 20, (e) 40 and (f) 60 min at 288 K and then pore-widened in 5 wt% phosphoric acid for 20 min at 303 K.

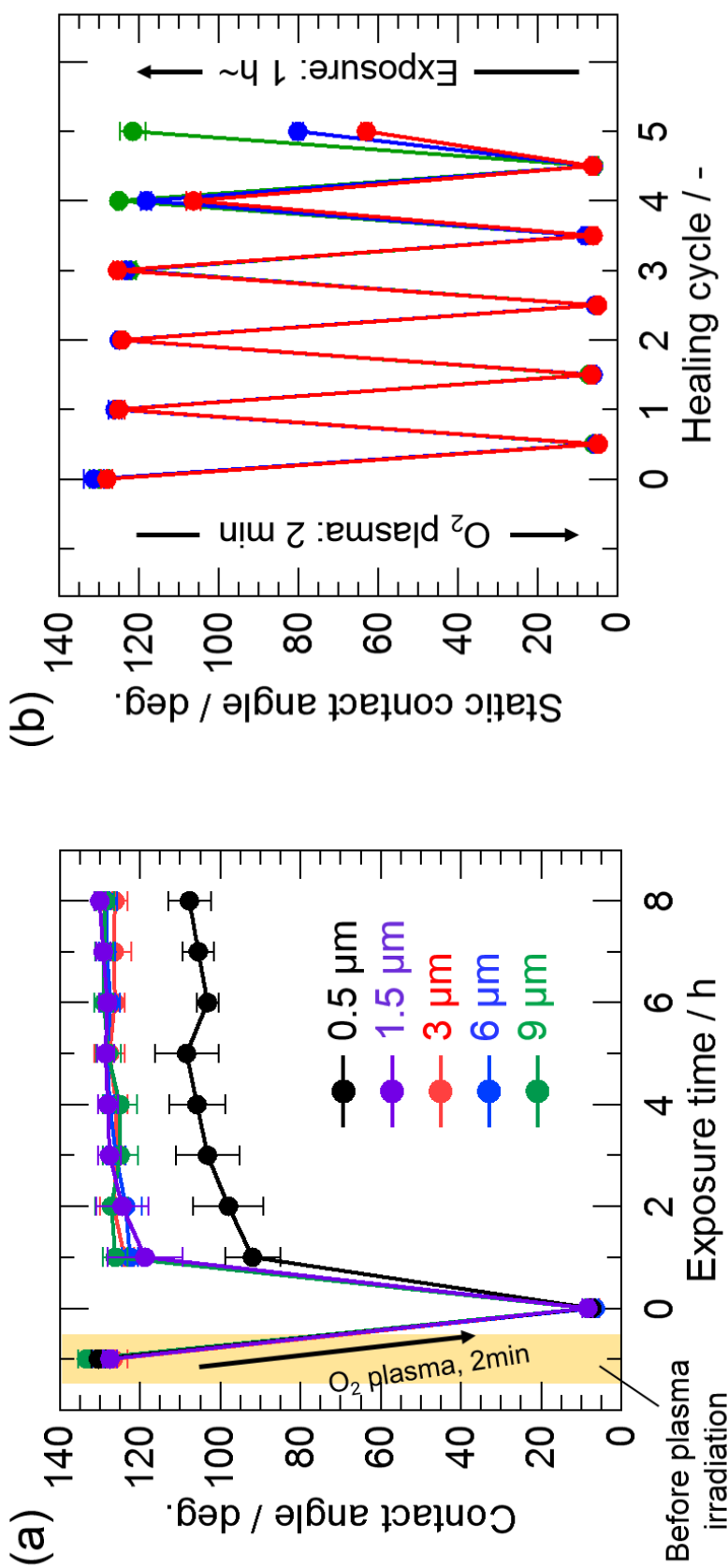


Figure 4.8 Dependence of nanopore length on (a) self-healing behavior with exposure in an atmosphere for 1-8 h and (b) repeatability of the self-healing property on the porous alumina specimens formed in 0.3 mol dm⁻³ sulfuric acid at a constant voltage of 25 V at 288 K; then pore-widened in 5 wt% phosphoric acid for 20 min at 303 K.

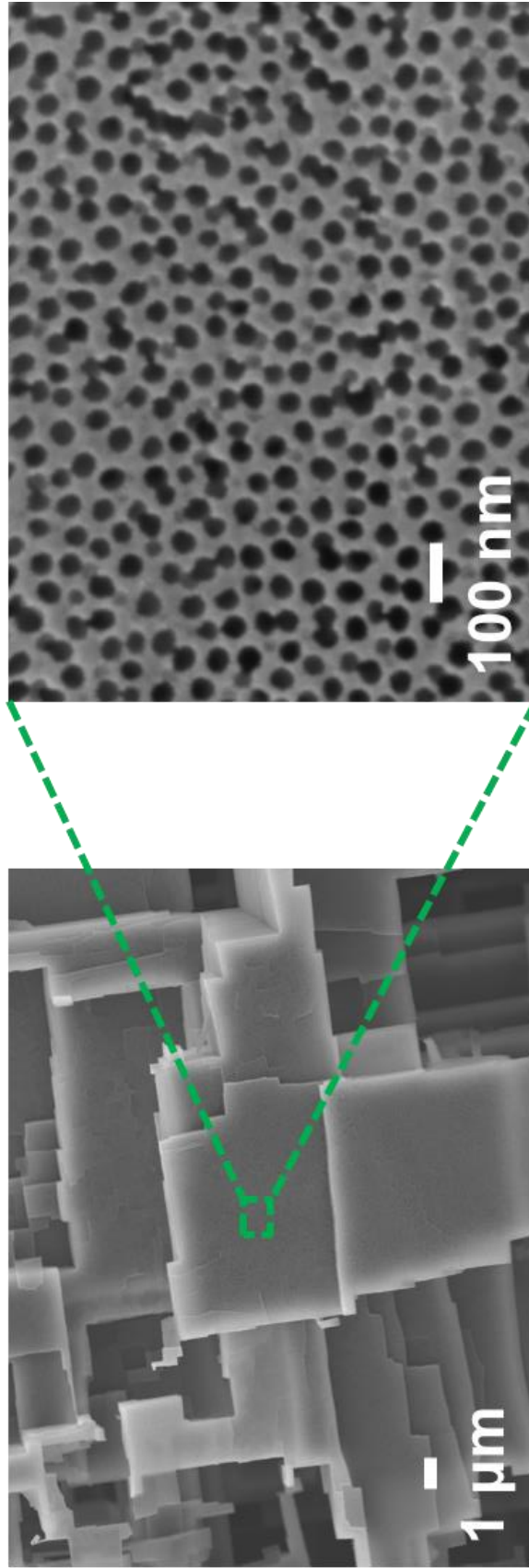


Figure 4.9 SEM micrographs of the aluminum surface chemically etched in solution containing $0.2 \text{ mol dm}^{-3} \text{ CuCl}_2$ and $1 \text{ mol dm}^{-3} \text{ HCl}$ for 360 s; then anodized in 0.3 mol dm^{-3} sulfuric acid at a constant voltage of 25 V for 180 s at 288 K; and finally immersed in 5 wt% phosphoric acid for 1200 s at 303 K.

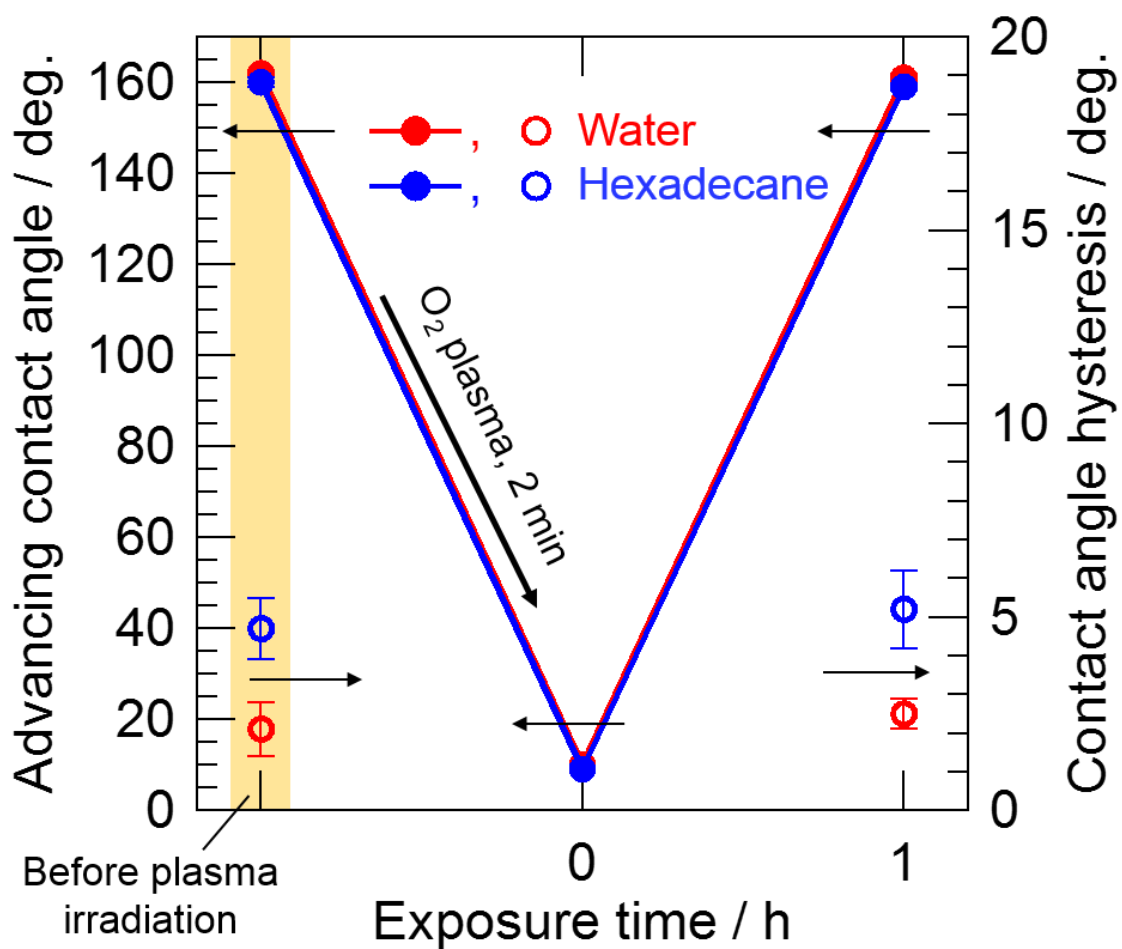


Figure 4.10 Self-healing behavior on superoleophobic dual-pore hierarchically rough aluminum surfaces for water (red) and hexadecane (blue).

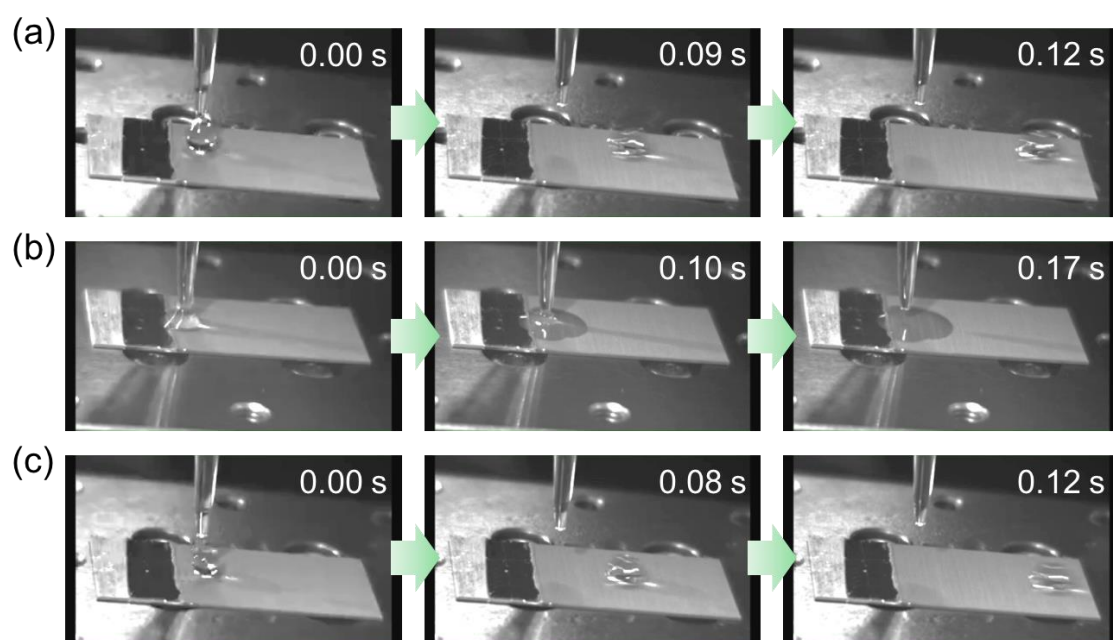


Figure 4.11 Optical images showing the sliding behavior of a hexadecane droplet (5 μL) on the hierarchical dual-pore aluminum surface coated FDPA (a) immediately fabricated, (b) after O_2 plasma irradiation for 2 min, and (c) exposed in an atmosphere for >1 h after O_2 plasma irradiation.

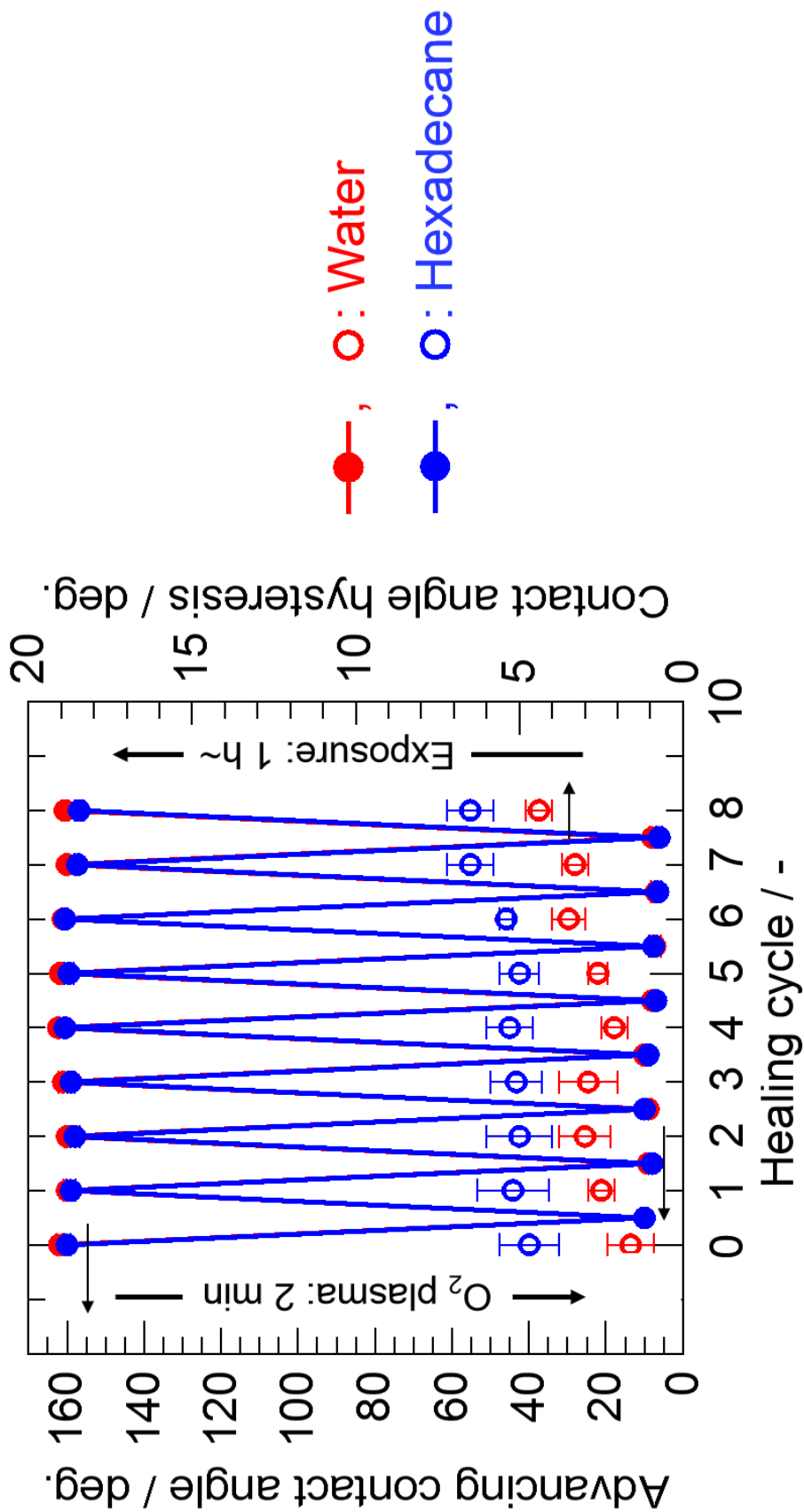


Figure 4.12 Repeatability of the self-healing property for (red) water and (blue) hexadecane droplets on the hierarchical dual-pore aluminum surface coated FDPA.

Chapter 5

*Fabrication of Self-Healing
Superhydrophobic CeO₂ Surface by
Practical Electrochemical Processes*

5.1 Introduction

Thin organic coatings, including self-assembled fluoroalkyl monolayers, have been often introduced on rough metallic or inorganic substrates for superoleophobicity, as also discussed in the previous chapters. However, such thin organic layers are readily damaged chemically and mechanically. Thus, improving the durability is the most important and challenging issue for superoleophobic surfaces. In the previous chapter the author demonstrates the self-healing of superoleophobicity by infiltration of a healing organic agent into the pores. In this chapter, an attempt has been made to obtain superhydrophobicity without using organic coatings.

As introduced in Chapter 1, Azimi et al. reported that rare-earth oxide (REO) surfaces show stable hydrophobicity after heat treatment up to 1000°C without any organic coating due to their unique electronic structure [1]. They demonstrated that water droplets could bounce on the surface of REO films formed by magnetron sputtering on silicon wafer. Moreover, they also revealed that REOs become superhydrophobic with textured morphology. These inorganic REOs are thermally and mechanically more stable compared to organic materials, promising as a novel durable hydrophobic coating. Therefore, hydrophobic REOs are of recent interest [2-5]. Most of the reports preparing hydrophobic REO coatings utilized dry processes such as sputtering [2] or atomic layer deposition [5]. Electrochemical deposition process is a simple, cost-effective and more practical method for oxide coatings [6]. This process also allows us to form a uniform oxide layer on rough and even porous substrates, suitable for fabrication of hierarchically rough superhydrophobic surfaces.

In this chapter, the CeO₂ coating was prepared by anodic deposition on flat and hierarchically rough stainless steel surface. The rough stainless steel surface was prepared by electrochemical etching, such that only electrochemical processes were used for surface preparation. Then, the surface wettability for water was evaluated by measuring static and dynamic contact angles. The self-healing properties of the hydrophobic surface was also examined.

5.2 Experimental

5.2.1 Specimen preparation

Type 304 stainless steel plates or meshes (with 300, 500, 640 and 795 mesh) composed of 17–19 wt.% Cr, 8–11 wt.% Ni, < 2 wt.% Mn, < 1 wt.% Si and Fe balance were used as substrate in this study. Prior to electrochemical etching and anodic deposition, the plate substrate was electropolished in solution containing HClO₄ and ethylene glycol (1:9 v/v) at 20 V for 5 min below 283 K. Electrochemical etching of the plate was performed in solution containing 1.2 wt% HNO₃ and 3.6 wt% HCl at a constant current density of 1 A cm⁻² for 200 s at 313 K [7]. For mesh specimens, etching was conducted at 1 A cm⁻² for 1 min in order to prevent excess etching of specimens. Anodic deposition was carried out at a constant current density of 1 A cm⁻² in solution containing 0.01 mol dm⁻³ Ce(NO₃)₃ and 0.05 mol dm⁻³ hexamethylenetetramine (pH 6.7) for 60 min at 333 K. The rather low concentration of Ce(NO₃)₃ was selected to form a thin coating to maintain the textured morphology developed by electrochemical etching. A two-

electrode cell with a Type 304 stainless steel counter electrode was used for anodic deposition. For comparison, we also prepared a barrier-type anodic alumina film on aluminum plate (99.999% purity). Prior to anodizing, an aluminum plate was electropolished in solution containing HClO₄ and ethanol (1:4, v/v) at a constant voltage of 20 V for 5 min below 278 K. Then, the specimen was anodized in 0.1 mol dm⁻³ ammonium pentaborate ((NH₄)₂B₁₀O₁₆) at a constant current density of 5 mA cm⁻² up to 200 V at 293 K, using a two-electrode cell with a platinum counter electrode. The alumina surface thus prepared was smooth and flat, as reported previously [8].

5.2.2 Characterizations

The surface and cross-section of the specimens were observed by a JEOL JSM-6500F field emission scanning electron microscope (SEM) and a JEOL JEM-2000FX transmission electron microscope (TEM) with EDS facilities, respectively. The cross-sectional specimen was prepared by focused gallium ion beam processing with a JEOL JIB-4600F/HKD multibeam system. Surface roughness was also evaluated using a KEYENCE VK09700 laser microscope. Phases in the anodically deposited CeO₂ layer formed on the stainless steel surface were identified by X-ray diffraction using a Rigaku RINT-2000 diffractometer with Cu K α radiation ($\lambda = 0.15418$ nm). An α - 2θ scan mode with $\alpha = 1^\circ$ was used in this study. Elemental depth profile analysis was carried out by glow discharge optical emission spectroscopy (GDOES) using a Jobin-Yvon 5000 RF instrument in an argon atmosphere of 700 Pa by applying a power of 30 W. Light emissions of characteristic wavelength were monitored throughout the analysis with a

sampling time of 0.01 s to obtain a depth profile. The wavelength of the spectral lines used were 413.717 nm for cerium, 130.217 nm for oxygen, 385.991 nm for iron, 425.433 nm for chromium, 341.477 nm for nickel and 165.701 nm for carbon. The signals were detected from a circular area of approximately 4 mm diameter. The X-ray photoelectron spectra of the anodically deposited CeO₂ and anodic alumina surfaces after air exposure for 1, 7 and 12 h in a laboratory atmosphere were measured using a JEOL JPS-9200 spectroscope with Mg K α excitation ($h\nu = 1253.6$ eV). Binding energies of the photoelectrons were calibrated with a contaminant carbon peak energy (285.0 eV).

5.2.3 Wettability evaluation

Surface wettability was evaluated by static and dynamic contact angle measurements for water droplet (4 μ L) on specimen surfaces by a Kyowa Interface Science DM-CE1 contact angle measurement system after air exposure for various periods of time in a laboratory atmosphere. Dynamic contact angle measurements were performed by an expansion and contraction method. Contact angle values used in this study were average data of five different points on each specimen.=

For examination of the self-healing hydrophobicity, oxygen plasma was irradiated for 4 min using a Harrick Plasma PDC-32G air plasma cleaner to the hydrophobic CeO₂ surface specimen in order to decompose organic contaminants on the surface. Then, water contact angle (WCA) was monitored during subsequent air exposure. This process was repeated several times.

5.3 Results and discussion

5.3.1 CeO₂ coating on stainless steel plate

Figs. 5.1a and 1b show SEM micrographs of the surface of the electropolished stainless steel plate after anodic deposition of CeO₂. The surface appears rather smooth at low magnification (Fig. 5.1a), while high magnification micrograph (Fig. 5.1b) discloses that the coating consists of densely packed nanoparticles with 10-15 nm in diameter. In Fig. 1a, microcracks are also found in the coating, probably associated with the shrinkage of the coating, which is caused by dehydration of the anodically deposited coating during drying [9]. Kulp et al. deposited anodically CeO₂ at 0.5 and 1.1 V vs Ag/AgCl in Ce(III) acetate solution, and obtained a smooth and crack-free film at 0.5 V vs Ag/AgCl, while a film consisting of nanoparticles was formed at 1.1 V vs Ag/AgCl [10]. They reported that the nanoparticles were formed because of indirect oxidation of Ce(III) with O₂ by electrochemical oxidation of water. The presence of nanoparticles in the present coating suggests such indirect mechanism of the formation of CeO₂. TEM observation of the coating cross-section (Fig. 5.1c) reveals that the coating is approximately 60 nm thick and uniform in thickness. EDX analysis of the marked region in Fig. 5.1c indicated the atomic ratio of Ce:O close to 1:2, corresponding to the composition of CeO₂. Figs. 5.2 shows the X-ray diffraction pattern and GDOES elemental depth profile of the anodically deposited CeO₂ on the electropolished stainless steel plate. Only a CeO₂ phase (JCPDS card 34-0394) is identified from the X-ray diffraction pattern, apart from the reflections from the stainless steel substrate (Fig. 5.2a). The species (Fe, Ni and Cr) derived from the stainless steel substrate are not detected within the coating

in the GDOES elemental depth profile analysis (Fig. 5.2b). Thus, rather pure CeO₂ is deposited on the stainless steel, although, from the depth profile, hydrogen and carbon impurity species appear to be slightly incorporated in the coating. The incorporated carbon species may be derived from hexamethylenetetramine added in the coating solution.

Then, the wettability of the CeO₂-coated specimen was examined by static contact angle measurements. Figs. 5.3 shows the WCAs and optical photographs of water droplets on the surfaces of the CeO₂ coating on electropolished stainless steel and the flat alumina film formed by anodizing of aluminum as a function of air exposure time. The WCA of the CeO₂ coating on the flat stainless steel is only 20° immediately after deposition; the anodically deposited CeO₂ is hydrophilic. This is contrast to the hydrophobicity of the magnetron-sputtered CeO₂ surface [1]. However, the WCA gradually increases with time of air exposure and reaches ~104° after three days. This means that the CeO₂ surface changes from hydrophilic to hydrophobic during air exposure. On the other hand, the WCA on the alumina surface remained hydrophilic even after three days.

In order to examine the change in composition of the CeO₂ and Al₂O₃ surface during air exposure, XPS surface analysis was performed. Figs. 5.4a-c show the Ce 3d, O 1s and C 1s photoelectron spectra of the CeO₂ surface. The Ce 3d spectra in Fig. 5.4a are composed of two multiplets (i.e., v and u), which correspond to the spin orbit split 3d_{5/2} and 3d_{3/2}, respectively. In accord with previous reports [11-15], the v, v'', v''', u, u'' and u''' peaks are attributed to Ce⁴⁺ state, while the v' and u' peaks are assigned to Ce³⁺

state. The intensity of all the Ce 3d peaks slightly decreases with time of air exposure. This is because of covering coating surface by hydrocarbon contaminants, as described below.

The O 1s spectra reveal two peaks at 529.5 eV and 531.4 eV; the former is assigned to Ce-O-Ce and the latter to -OH/H₂O oxygen, defective oxide or carbonate oxygen, respectively [11, 16, 17]. The presence of surface -OH/H₂O species probably make the surface hydrophilic. During air exposure, the intensity of -OH/H₂O peak decreases slightly. The most significant change in the spectra was found in C 1s spectra during air exposure. The contaminant hydrocarbon peak at 285.0 eV becomes intense largely during air exposure, indicating the accumulation of hydrocarbon layer on the CeO₂ surface. A small peak at 289.0 eV is assigned to carboxyl or carbonate species [18, 19], whose intensity remains almost unchanged.

The change in the XPS spectra of the Al₂O₃ surface during air exposure was also examined (Figs. 5.4d-f). The Al 2p spectra shows a peak at 74.3 eV, corresponding to Al³⁺ state [20]. A broad O 1s peak is owing to overlapping of Al-O-Al (530.9 eV) and OH/H₂O (531.8 eV) peaks. The intensity of the C 1s hydrocarbon peak (285.0 eV) increases with air exposure, but the increase in the intensity for Al₂O₃ surface is much less than that on the CeO₂ surface. As a consequence, only CeO₂ surface changes from hydrophilic to hydrophobic during air exposure.

Preston et al. reported the hydrophobicity of a CeO₂ pellet after air exposure for long time, similar to this study [4]. According to their report, a hydrophilic CeO₂ pellet surface conversed to hydrophobic due to adsorption of hydrocarbon contaminants

compared to silica or gold surfaces; the WCA reaches 90° after air exposure for 96 h. In addition, this trend has been shown for a variety of non-noble metal oxide materials including zirconia and titania, and occurs due to physisorption of hydrocarbons to –OH groups and other energetically favorable sites present on the surface, where physical or chemical interactions are possible. In other words, hydrocarbon in the atmosphere can be adsorbed on the surface with high density of –OH groups [4, 21]. Thus, it is likely that the difference of wettability behavior between CeO₂-coated stainless steel and flat anodized alumina is owing to the difference of the amount of –OH groups on the surfaces. The anodically deposited CeO₂ surface may contain a high density of surface –OH group, promoting the accumulation of hydrocarbon contaminants from air. As a consequence, the surface becomes hydrophilic in air exposure. In fact, the deconvolution of O 1s spectra showed that approximately 40% of oxygen was –OH/H₂O-type on the as-deposited CeO₂ and that on the as-formed Al₂O₃ was only ~10%.

5.3.2 Introduction of surface roughness of CeO₂ for superhydrophobicity

Since the WCA as high as ~104° is obtained by anodic deposition of CeO₂ on the flat stainless steel surface, we tried to introduce surface roughness to make the surface superhydrophobic [22]. The rough surface was developed in this study by electrochemical etching of stainless steel prior to CeO₂ deposition. Figs. 5.5 shows SEM micrographs of the electrochemically etched stainless steel surface before and after CeO₂ deposition. Numbers of semi-spherical large etch pits with several sizes of 50-100 μm (Fig. 5.5a), ~5

μm and $0.1\text{-}0.5\ \mu\text{m}$ (Fig. 5.5b) are formed by the etching. Such surface morphology was remained even after deposition of CeO_2 , and from the comparison of the high magnification images obtained before and after deposition (Figs 5.5c and 5.5f), $10\ \text{nm}$ scale roughness is further introduced after the deposition because of the formation of nano-particular CeO_2 .

Fig. 5.6 shows the change in WCA on CeO_2 -coated flat and etched stainless steel surface with air exposure time. Immediately after deposition, the CeO_2 surface on the etched stainless steel is again hydrophilic, and the WCA is as low as 13° , which is lower than that on flat stainless steel (20°). The lower WCA on the etched specimen is explained from the Wenzel equation [22]:

$$\cos\theta_R = R\cos\theta_F \quad (1)$$

in which θ_R and θ_F are the WCAs on rough and flat surfaces and R is the roughness factor ($R > 1$). This equation indicates that θ_R decreases with surface roughening when the θ_F is less than 90° . Thus, the reduced WCA of the CeO_2 coating on the etched stainless steel in comparison with that on the flat stainless steel is qualitatively explained by surface roughening. After air exposure for 3 days, the WCA reaches 130° on the etched specimen, being higher than that on the flat specimen (104°). The R value estimated from the equation 1 is 2.66. The roughness was also estimated using a laser microscope, which indicated the roughness factor of 2.57. These two values are close to each other, suggesting that the water droplet on the CeO_2 coating on the etched stainless steel is in the Wenzel state. The roughness is not high enough for superhydrophobicity.

On the superhydrophobic surface, on which a water droplet is readily rolling off, a

Cassie-Baxter state must be achieved. In this case, air pockets are present between the water droplet and the rough solid surface. Because of the reduced liquid/solid contact area, the water is rolling off more readily in comparison with the Wenzel state, in which all the rough solid surface is contacted with liquid. To obtain a superhydrophobic CeO₂ surface by further enhancing the surface roughness, we utilized stainless steel mesh (mesh opening of 15 μm and wire diameter also of 15 μm) as substrate. Figs. 5.7 shows scanning electron micrographs of the etched and non-etched stainless steel mesh with and without CeO₂ coating. The electrochemically etched mesh (Figs. 5.7a-c) discloses surface roughness and the grooves developed by the etching extends along with the wire direction (Fig. 5.7b). The roughness is remained even after CeO₂ deposition (Figs. 5.7d-f) and further nanoscale roughness is introduced by nanoparticle nature of CeO₂. High roughness of the etched mesh with CeO₂ is obvious from the comparison with the non-etched counterpart (Figs. 5.7g-i).

Fig. 5.8a shows the WCAs on the CeO₂-coatings on various stainless steel morphologies after air exposure for 3 days. The WCA on the CeO₂-coated stainless steel mesh without etching is only 121.3°, which is lower than that on the etched stainless steel plate. The electrochemical etching of the stainless steel mesh increases the WCA remarkably and the WCA reaches 155.7°. The dynamic WCA was also measured for the CeO₂ coated on the etched stainless steel mesh. The advancing and receding contact angles were 159.4° and 157.4°, respectively and the contact angle hysteresis is as low as 2.0° (Fig. 5.8b); the surface is superhydrophobic.

Fig. 5.9 shows the schematic illustration showing the wetting behavior of the CeO₂

surface coated on etched stainless steel plate and mesh. The coating on the etched stainless steel plate was hydrophobic but not superhydrophobic. As discussed above, the surface is in the Wenzel state (Fig. 5.9a) [22]. Similarly, the CeO₂ coating on the stainless steel mesh without electrochemical etching is hydrophobic from the WCA shown in Fig. 5.8a, but not superhydrophobic. Rather smooth wire surface of the mesh allows water to penetrate through the mesh.

On the other hand, it is most likely that the CeO₂ coating on the etched stainless steel mesh surface was in the Cassie-Baxter state due to superhydrophobicity, as shown in Fig. 5.9c. Assuming the Cassie-Baxter state, the f value in the equation (2) is estimated to be as low as 0.12 from the θ_R and θ_F values of 155.7 and 104.1, respectively [23].

$$\cos \theta_R = f(1 + \cos \theta_F) - 1 \quad (2)$$

This f value suggests that only a limited part of the mesh wires, roughly 4 μm width of the top part of the mesh wire, may be in contact with water droplet. Pinning of the water droplet by surface roughness of the mesh introduced by electrochemical etching is effective in achieving the superhydrophobic state.

5.3.3 Self-healing property of superhydrophobic CeO₂ surface

Since the superhydrophobic CeO₂ surface was obtained by accumulation of a carbon contaminant layer from the atmosphere, superhydrophobicity will be self-healed even after removing the hydrocarbon surface layer. In this study, we examined the self-healing behavior after oxygen plasma treatment of the superhydrophobic CeO₂ surface. As shown in Fig. 5.10, the high WCA of $>150^\circ$ changes to $\sim 0^\circ$ after oxygen plasma

treatment, probably because of the decomposition of the contaminant hydrocarbon layer and the introduction of surface –OH group by oxygen plasma [24, 25]. However, the WCA recovers again to >150° during air exposure for 72 h, and the superhydrophilic to superhydrophobic transition due to re-accumulation of contaminant hydrocarbons occurs repeatedly as shown in this figure. Findings demonstrate that the present CeO₂ coating possess the self-healing nature of superhydrophobicity.

Low durability is one of the critical issues for the practical use of superhydrophobic materials. Self-healing property is, therefore, of crucial importance to enhance the durability [26-30]. The present superhydrophobic CeO₂ surface on the stainless steel mesh showed the self-healing property because hydrophobic surface layer is derived from hydrocarbon in the atmosphere. In addition, rough CeO₂ surface is readily prepared by a combination of simple electrochemical processes. The hierarchical CeO₂ surface formed by the electrochemical approach is, therefore, promising as a practical self-healing superhydrophobic material.

5.3.4 Application to oil/water separation

Since the etched stainless steel mesh with CeO₂ coating is superhydrophobic and superoleophilic as shown in Figs. 5.11a and 11b, we attempt to apply the CeO₂-coated stainless steel mesh for oil/water separation. When a mixture of oil (cyclohexane: surface tension, $\gamma = 25.3 \text{ mN m}^{-1}$) and water ($\gamma = 72.8 \text{ mN m}^{-1}$) was poured onto the etched stainless steel mesh coated with CeO₂, only cyclohexane penetrated through the mesh, but no penetration of water occurred, resulting in almost complete oil/water separation

(Fig. 5.11c). Thus, we succeeded in separating an oil/water mixture by electrochemical etching and CeO₂ coating without low-surface-tension treatment by another coating such as organic self-assembled monolayers.

5.4 Conclusions

In summary, CeO₂ coating anodically deposited on a flat stainless steel surface was hydrophilic immediately after deposition, while converted to hydrophobic after exposure to the atmosphere. This wettability transition is due to accumulation of hydrocarbon contaminant in air. Superhydrophobic CeO₂ surface is obtained by the deposition of CeO₂ on the electrochemically etched stainless steel mesh with sufficiently high roughness after air exposure. The superhydrophobic CeO₂ surface also exhibits self-healing property.

References

- [1] G. Azimi, R. Dhiman, H. Kwon, A. T. Paxson, K. K. Varanasi, *Nat. Mater.* **12**, 315 (2013).
- [2] I. Oh, K. Kim, Z. Lee, K. Y. Ko, C. Lee, S. J. Lee, J. M. Myung, C. Lansalot-Matras, W. Noh, C. Dussarrat, H. Kim, H. Lee, *Chem. Mater.* **27**, 148 (2015).
- [3] F. Pedraza, S. A. Mahadik, B. Bouchaud, *Phys. Chem. Chem. Phys.* **17**, 31750 (2015).
- [4] D. J. Preston, N. Miljkovic, J. Sack, R. Enright, J. Queemey, E. N. Wang, *Appl. Phys. Lett.* **105**, 011601 (2014).

- [5] S. Khan, G. Azimi, B. Yildiz, K. K. Varanasi, *Appl. Phys. Lett.* **106**, 061601 (2015).
- [6] J. Tam, G. Palumbo, U. Erb, *Materials* **9**, 151 (2016).
- [7] C. Lee, A. Kim, J. Kim, *Surf. Coat. Technol.* **264**, 127 (2015).
- [8] K. Shimizu, H. Habazaki, P. Skeldon, G.E. Thompson, R.K. Marcus, *Spectroscopy* **17**, 14 (2002).
- [9] L. Arurault, P. Monsang, J. Salley, R. S. Bes, *Thin Solid Films* **466**, 75 (2004).
- [10] E. A. Kulp, S. J. Limmer, E. W. Bohanman, J. A. Switzer, *Solid State Ionics* **178**, 749 (2007).
- [11] J. Xu, S. S. Xin, P. H. Han, R. Y. Ma, M. C. Li, *Mater. Corros.* **64**, 619 (2013).
- [12] H. Ardelean, I. Frateur, P. Marcus, *Corros. Sci.* **50**, 1907 (2008).
- [13] S. Yang, W. Zhu, Z. Jiang, Z. Chen, J. Wang, *Appl. Surf. Sci.* **252**, 8499 (2006).
- [14] X. Gao, Y. Jiang, Y. Zhong, Z. Y. Luo, K. F. Cen, *J. Hazard Mater.* **174**, 734 (2010).
- [15] A. Q. Wang, P. Panchaietch, R. M. Wallace, T. D. Goldenb, *J. Vac. Sci. Technol. B* **21**, 1169 (2003).
- [16] M. Kang, E. D. Park, J. M. Kim, J. E. Yie, *Appl. Catal. A* **327**, 261 (2007).
- [17] L. Martinez, E. Roman, J. L. de Segovia, S. Poupard, J. Creus, F. Pedraza, *Appl. Surf. Sci.* **257**, 6202 (2011).
- [18] W. Tseng, C. Tseng, C. Kuo, *Nanoscale Res Lett.* **4**, 234 (2009).
- [19] D. Zhang, Y. Ma, H. Feng, Y. Hao, *J. Chil. Chem. Soc.* **57**, 964 (2012).
- [20] T. Sugama, N. Carciello, *J. Non-Cryst. Solids* **134**, 58 (1991).
- [21] S. Takeda, M. Fukawa, Y. Hayashi, K. Matsumoto, *Thin Solid Films* **339**, 220 (1999).
- [22] R. N. Wenzel, *Ind. Eng. Chem.* **28**, 988 (1936).

- [23] A. B. D. Cassie, S. Baxter, *Trans. Faraday Soc.* **40**, 546 (1944).
- [24] A. L. Summer, E. J. Menke, Y. Dubowski, J. T. Newberg, R. M. Penner, J. C. Hemminger, L. M. Wingen, T. Brauers, B. J. Finlayson-Pitts, *Phys. Chem. Chem. Phys.* **6**, 604 (2004).
- [25] S. B. Habib, E. Gonzalez II, R. F. Hicks, *Appl. Vac. Sci. Technol. A* **28**, 476 (2010).
- [26] Y. Li, L. Li, J. Sun, *Angew. Chem.* **122**, 6265 (2010).
- [27] X. Wang, X. Lu, F. Zhou, W. Liu, *Chem. Commun.* **47**, 2324 (2011).
- [28] C. Xue, Z. Zhang, J. Zhang, S. Jia, *J. Mater. Chem. A* **2**, 15001 (2014).
- [29] D. Zhu, X. Lu, Q. Lu, *Langmuir* **30**, 4671 (2014).
- [30] M. Wu, B. Ma, T. Pan, S. Chen, J. Sun, *Adv. Funct. Mater.* **26**, 569 (2016).

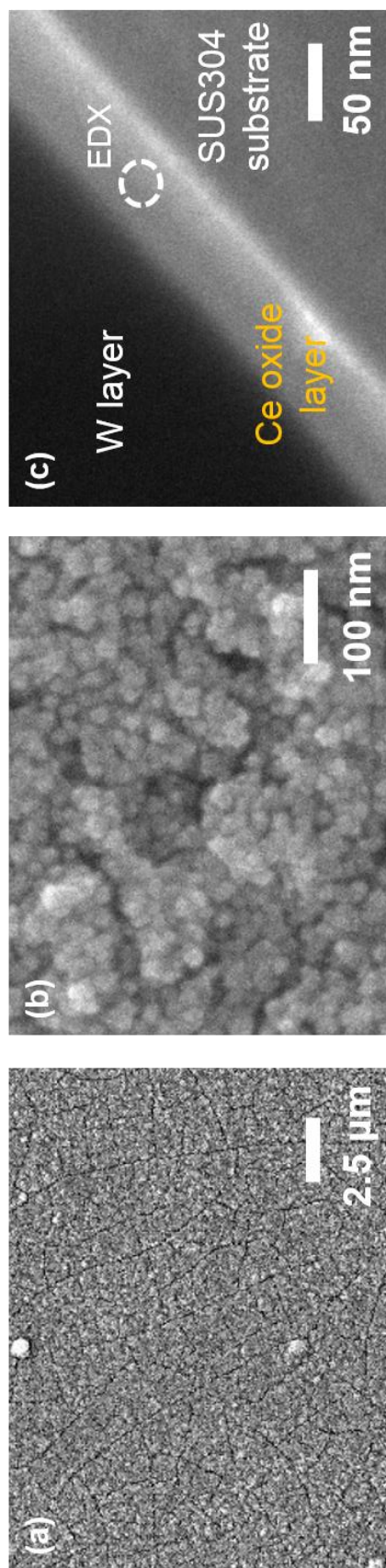


Figure 5.1 Surface SEM images with (a) low and (b) high magnification and (c) a cross-sectional TEM image of Type 304 stainless steel plate after anodic deposition in solution containing $0.01 \text{ mol dm}^{-3} \text{ Ce(NO}_3)_3$ and 0.05 mol dm^{-3} hexamethylenetetramine at a constant current density of 10 A m^{-2} for 60 min at 333 K.

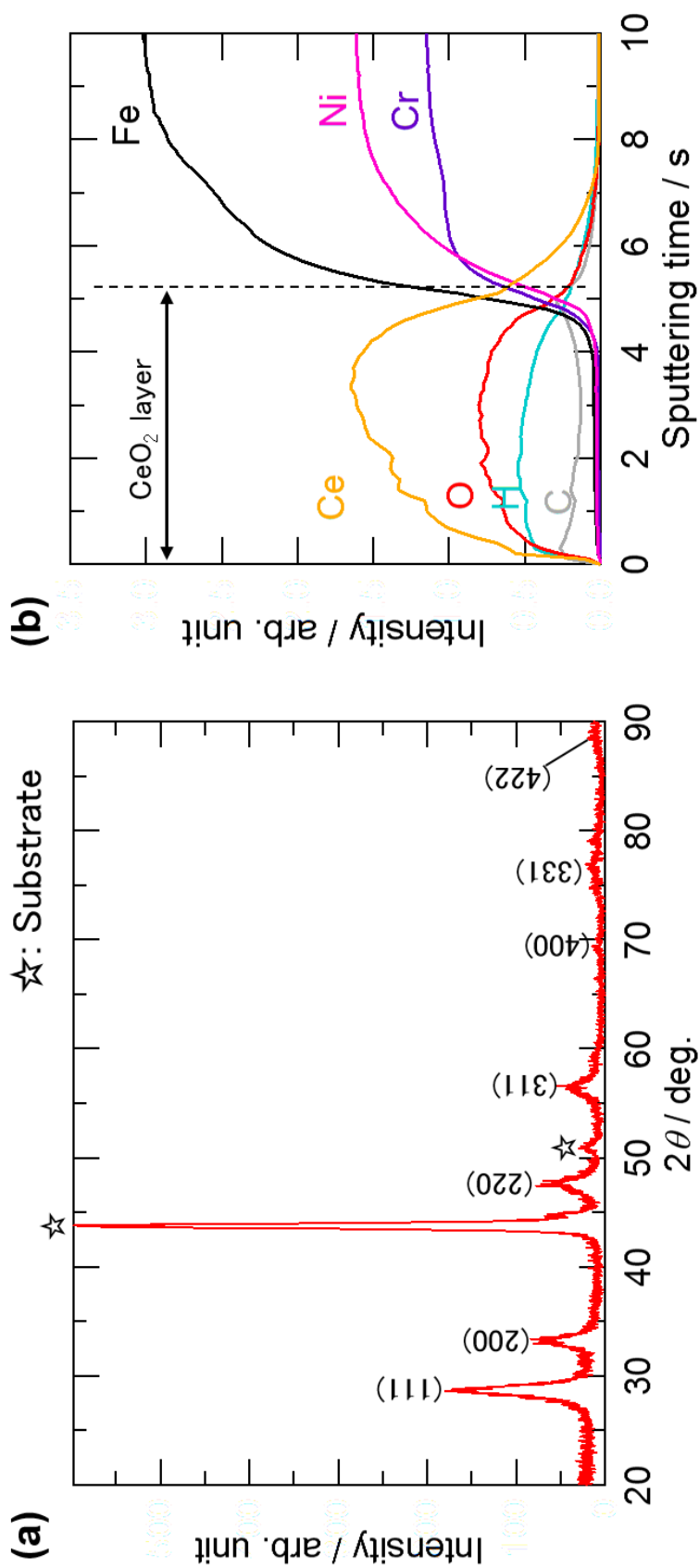


Figure 5.2 (a) XRD pattern and (b) GDOES elemental depth profile of the anodically deposited coating on Type 304 stainless steel plate in solution containing $0.01 \text{ mol dm}^{-3} \text{ Ce(NO}_3)_3$ and 0.05 mol dm^{-3} hexamethylenetetramine at a constant current density of 10 A m^{-2} for 60 min at 333 K.

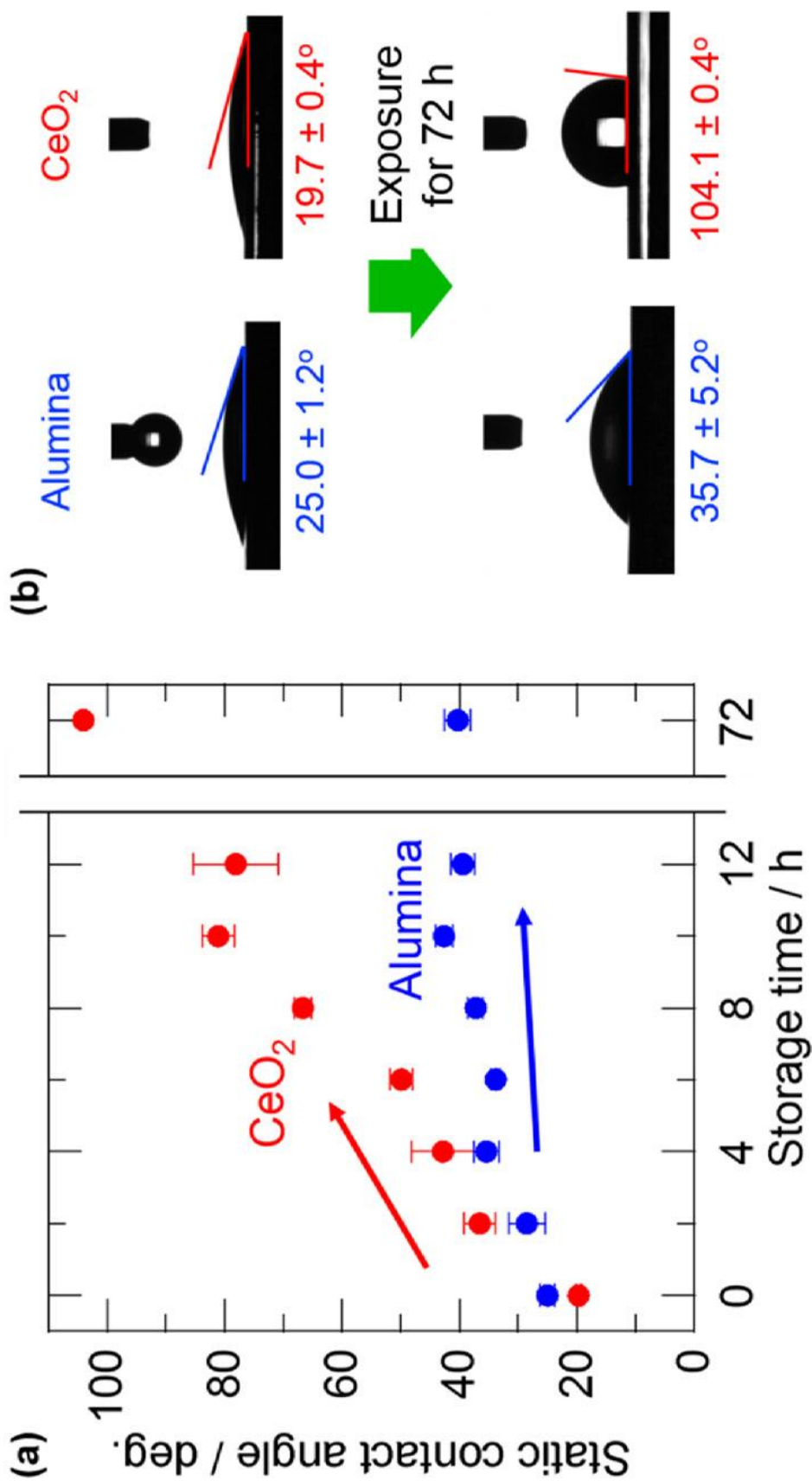


Figure 5.3 (a) The WCAs as a function of air exposure time and (b) optical images of water droplets on Type 304 stainless steel plate surface with CeO₂ coating and aluminum plate surface anodized in 0.1 mol dm⁻³ ammonium pentaborate aqueous solution up to 200

V at 293 K.

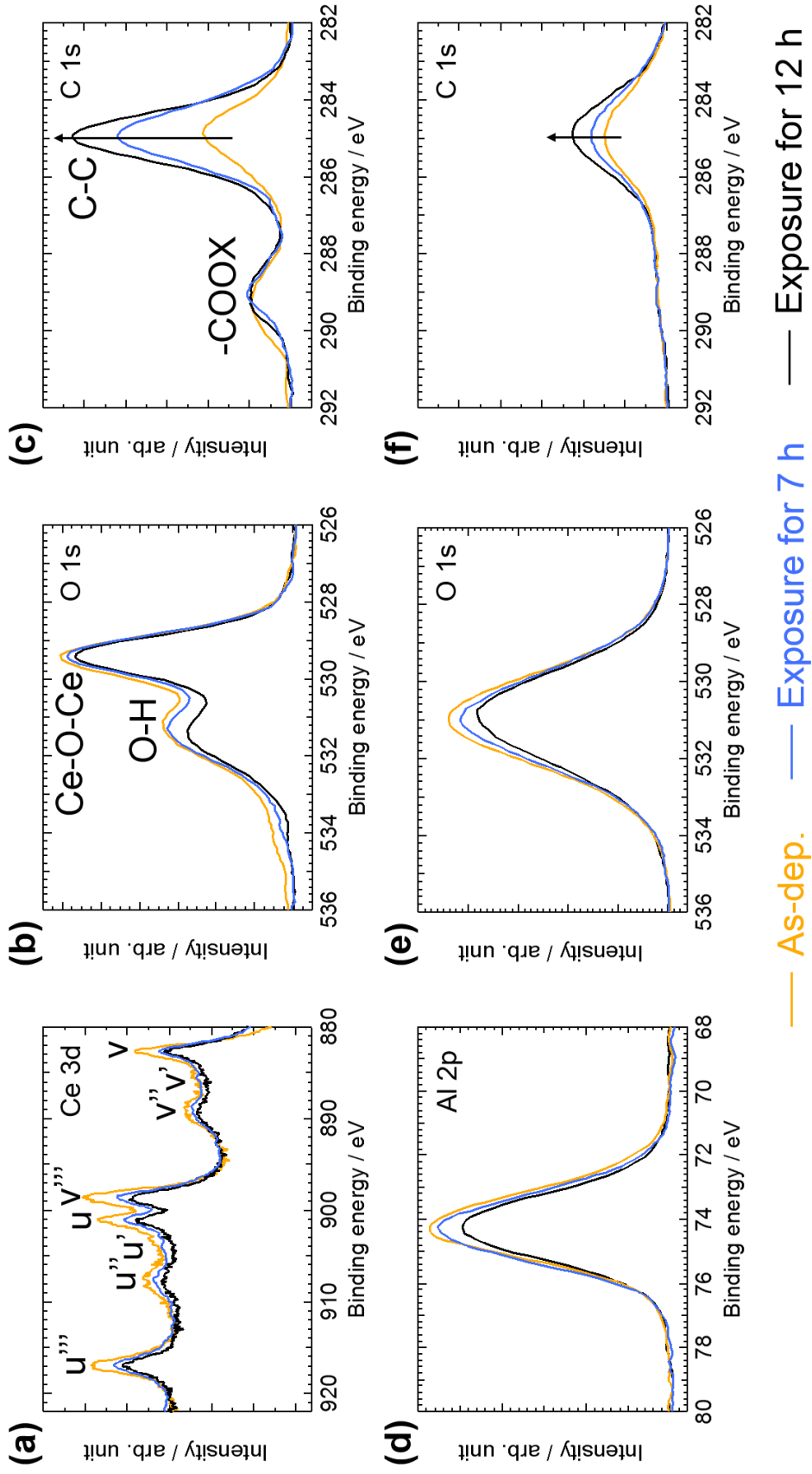


Figure 5.4 XPS narrow scan spectra of (a-c) CeO₂ coating surface anodically deposited on Type 304 stainless steel plate and (b-f) anodized alumina surface after air exposure for 0, 7 and 12 h.

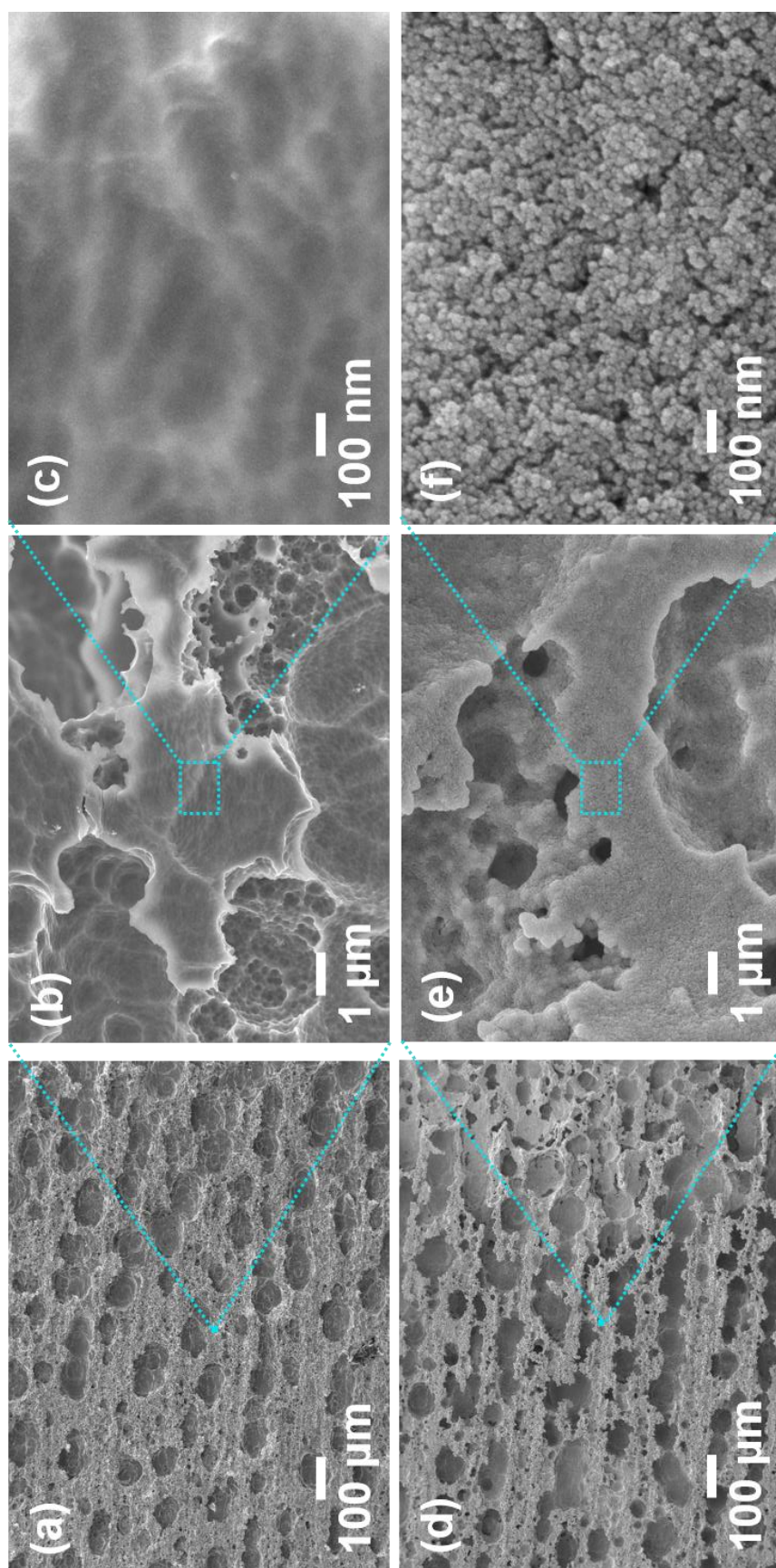


Figure 5.5 SEM images with magnifications of (a, d) $\times 100$, (b, e) $\times 10000$ and (c, f) $\times 100000$ of Type 304 stainless steel plate surface electrochemically etched in solution containing 1.2 wt.% HNO₃ and 3.6 wt.% HCl at a constant current density of 10 kA m⁻² up to 4×10^6 C m⁻² at 313 K (a-c); then anodically deposited CeO₂ coating in solution containing 0.01 mol dm⁻³ Ce(NO₃)₃ and 0.05 mol dm⁻³ hexamethylenetetramine at a constant current density of 10 A m⁻² for 60 min at 333 K (c-f).

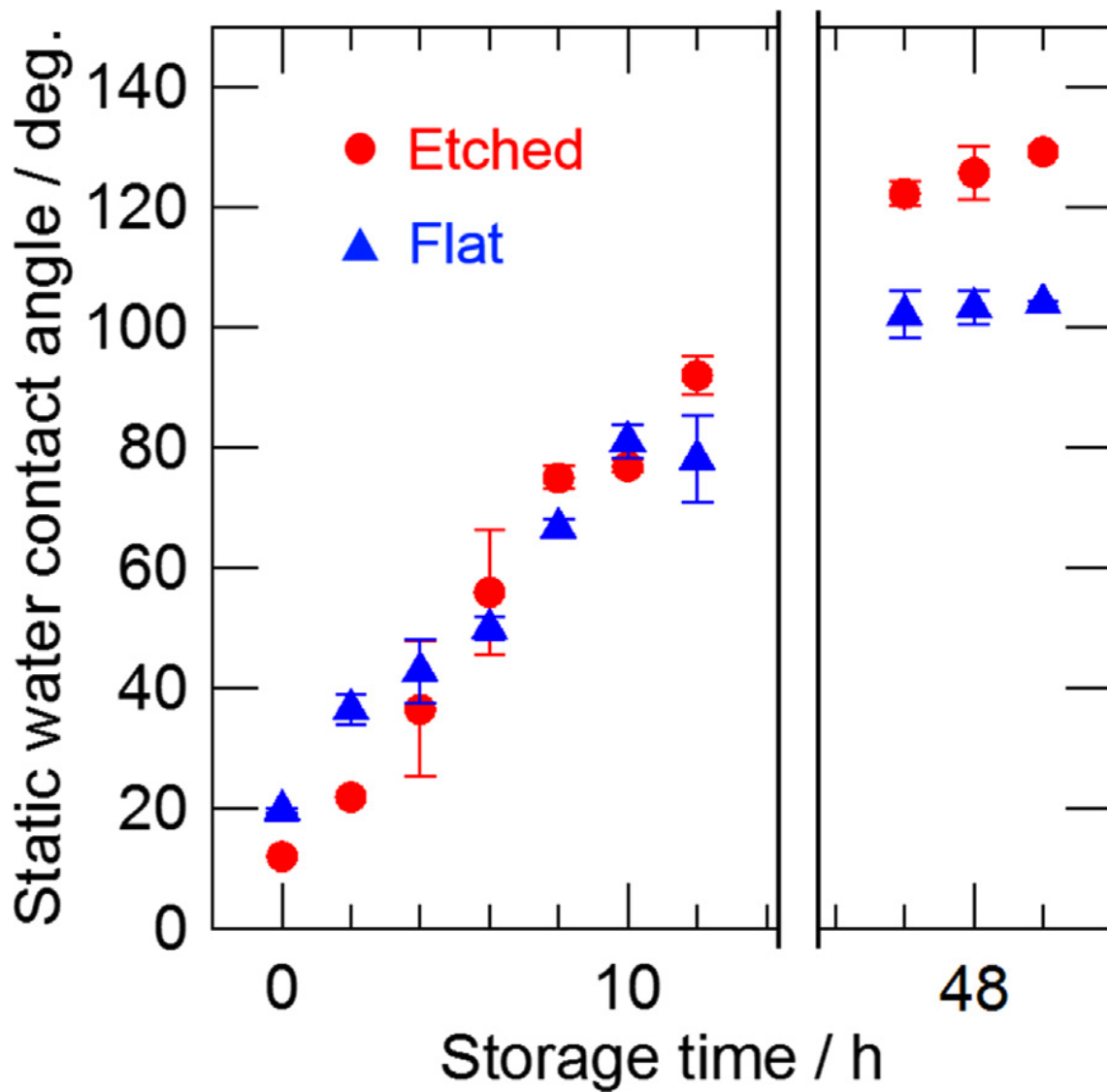


Figure 5.6 The WCAs on stainless steel plate with or without electrochemical etching after anodic deposition of CeO_2 coating as a function of air exposure time.

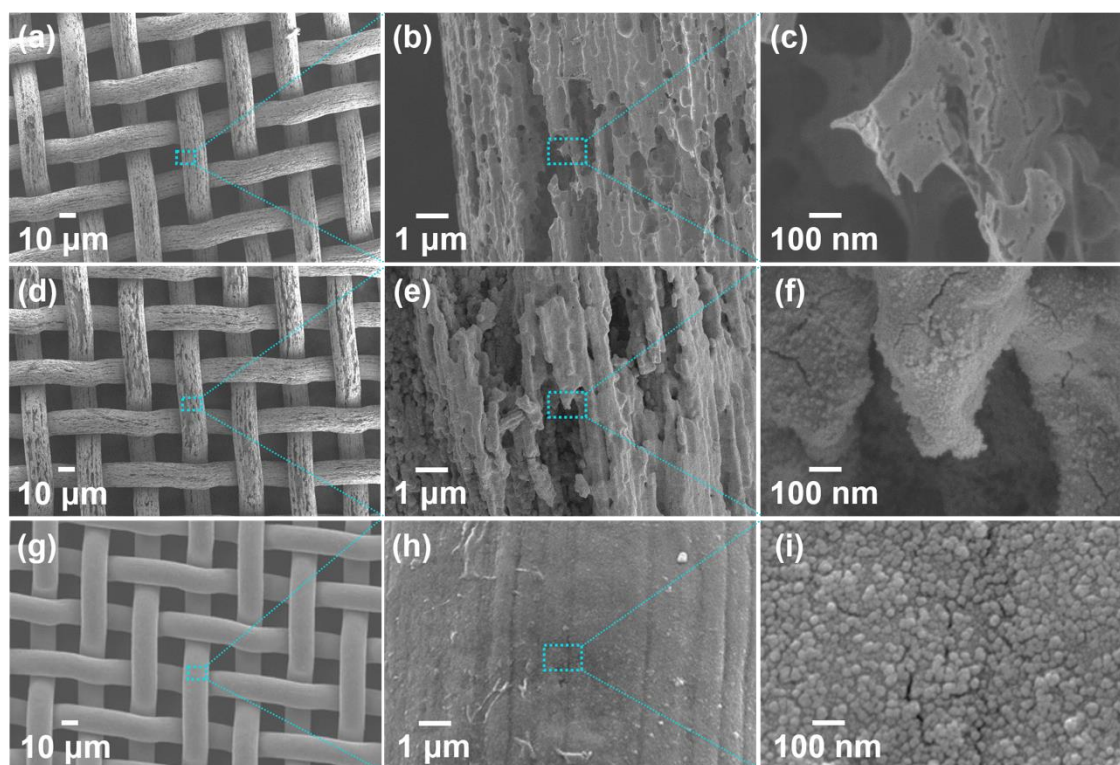


Figure 5.7 SEM images of Type 304 stainless steel mesh surfaces (a-f) electrochemically etched in solution containing 1.2 wt.% HNO₃ and 3.6 wt.% HCl at a constant current density of 100 A m⁻² for 60 s at 313 K (a-c) before and (d-f) after CeO₂ anodic deposition in solution containing 0.01 mol dm⁻³ Ce(NO₃)₃ and 0.05 mol dm⁻³ hexamethylenetetramine at a constant current density of 10 A m⁻² for 60 min at 333 K. (g-i) Surface micrographs of CeO₂-coated stainless steel mesh without etching. The magnifications are (a, d) ×500, (b, e) ×10000 and (c, f) ×100000, respectively.

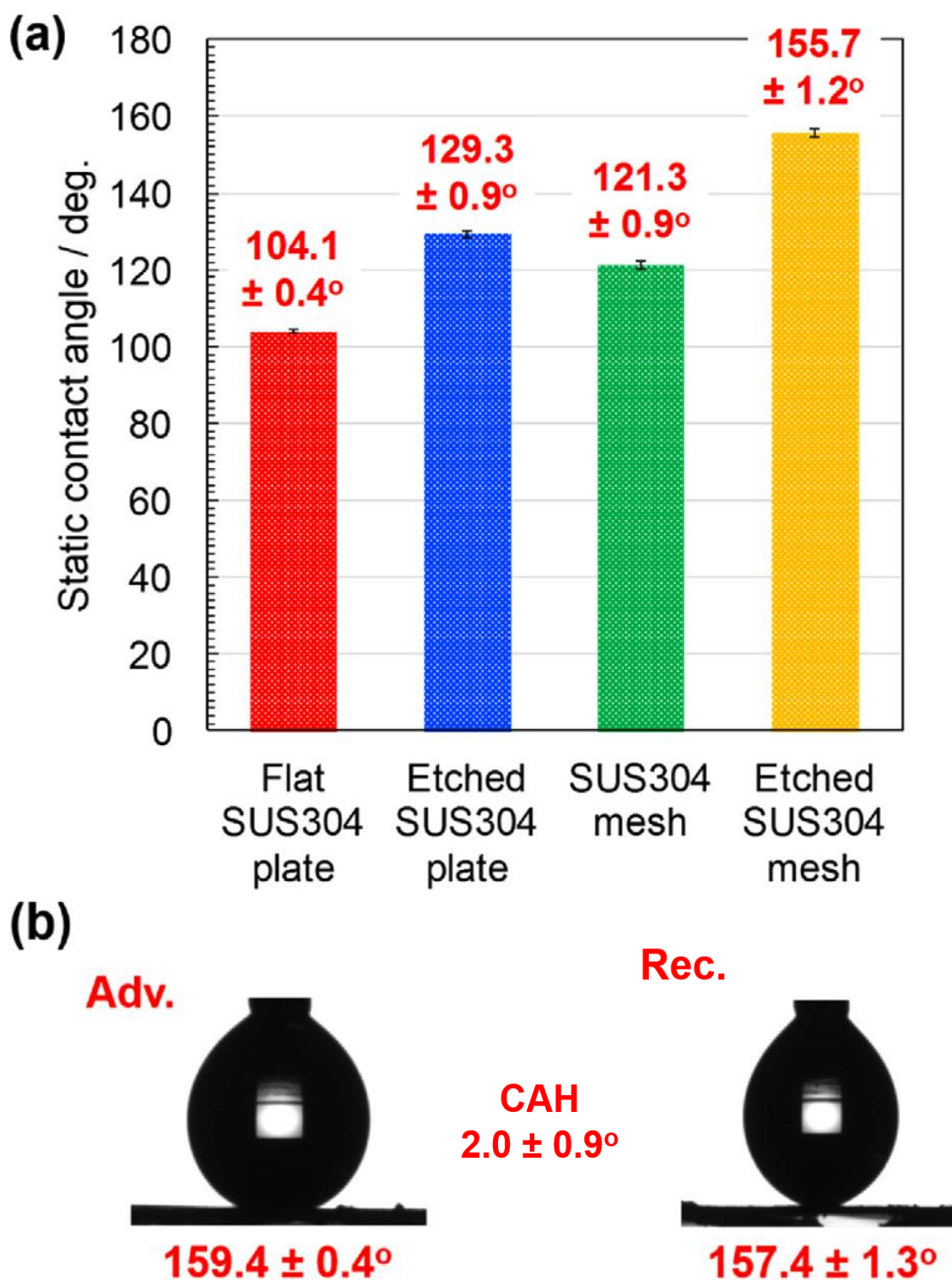


Figure 5.8 (a) The static WCAs on Type 304 stainless steel plate and mesh surfaces with or without electrochemical etching and CeO_2 anodic deposition after air exposure for three days. (b) Optical images of the water droplets during dynamic contact angle measurement for etched stainless steel mesh with CeO_2 coating.

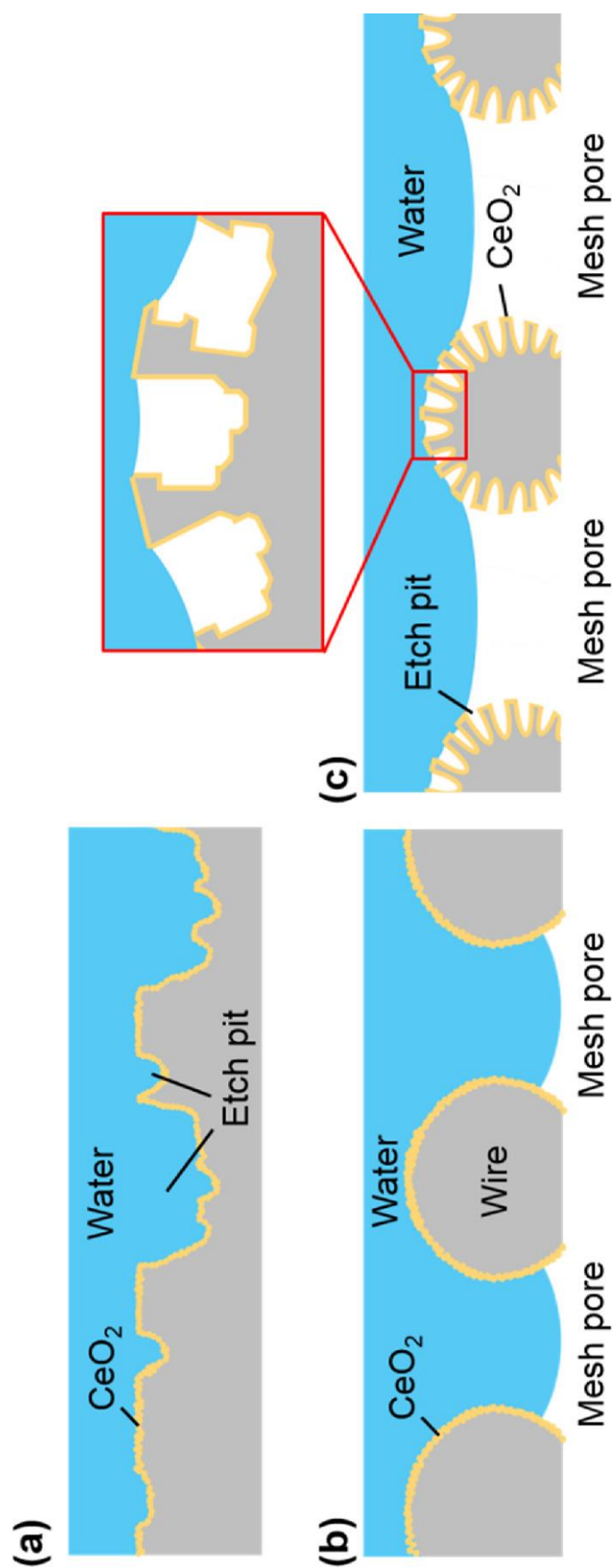


Figure 5.9 Schematic illustrations showing water penetration into pores on (a) electrochemically etched stainless steel plate, (b) without and (c) with electrochemical etching after CeO_2 anodic deposition.

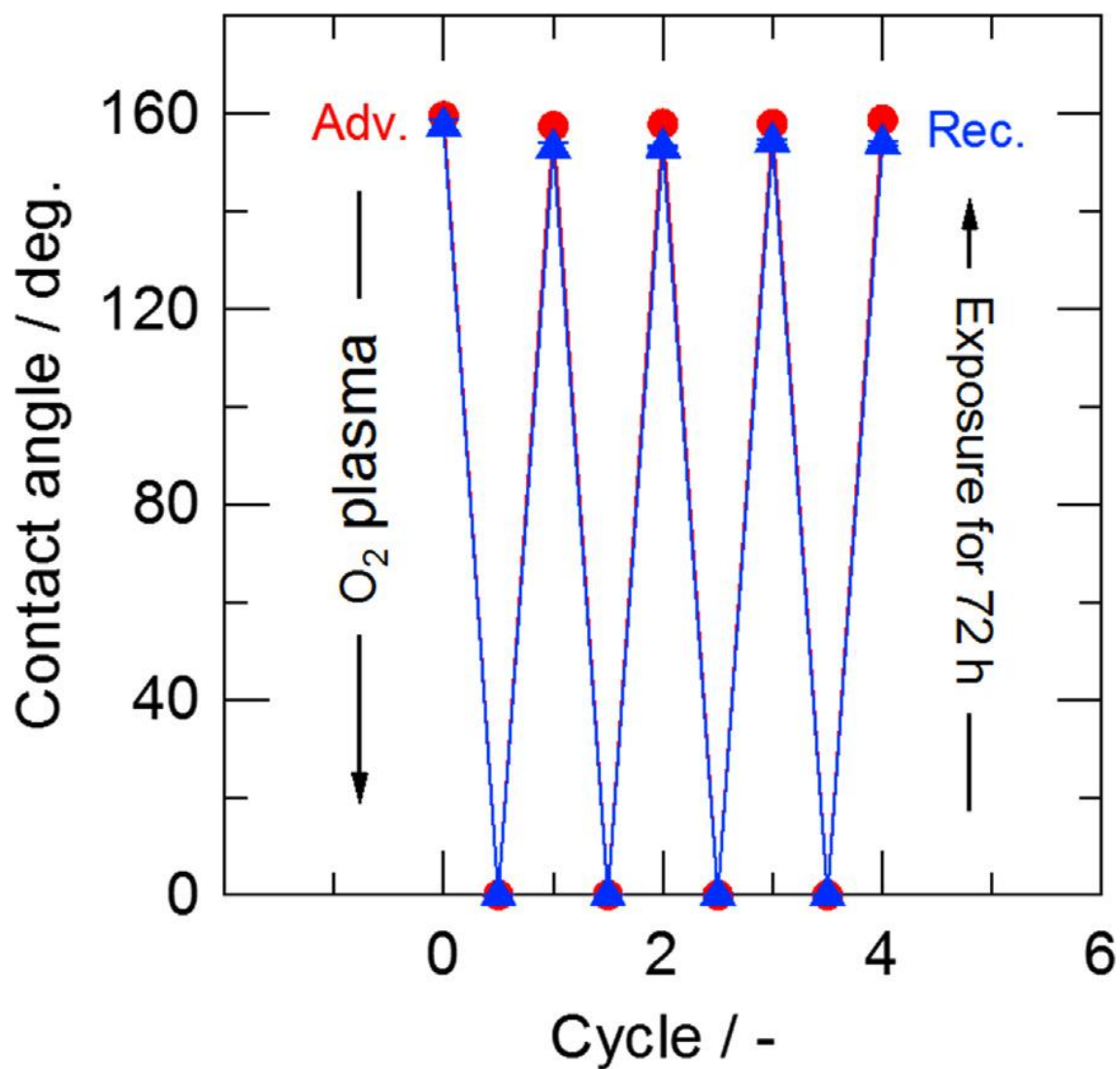


Figure 5.10 The advancing and receding contact angles for water on Type 304 stainless steel mesh electrochemically etched and deposited CeO₂ coating after several consecutive O₂ plasma treatment for 2 min and air exposure for 72 h.

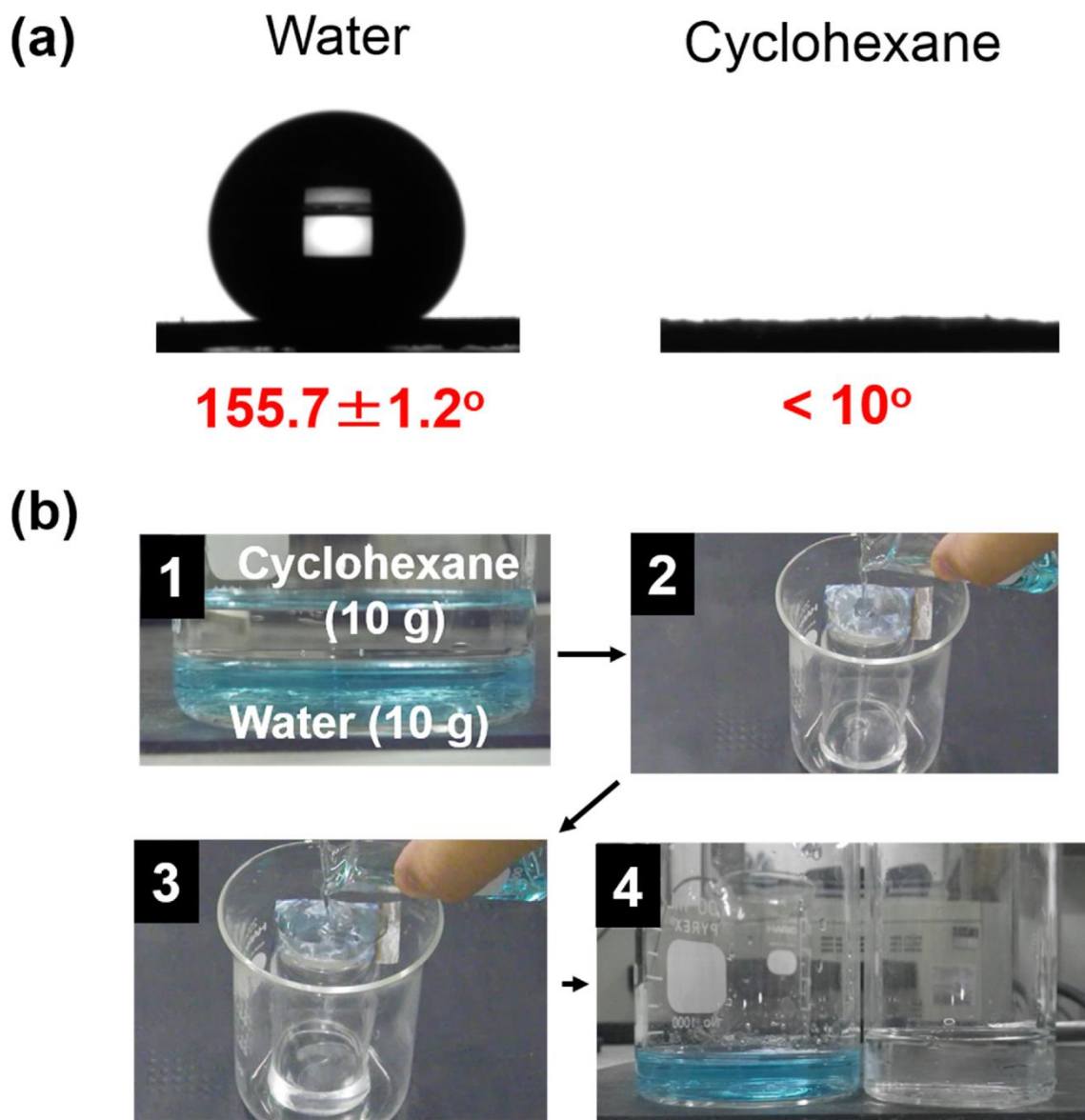


Figure 5.11 Optical images of (a) water and cyclohexane droplets on superhydrophobic Type 304 stainless steel electrochemically etched and anodically deposited CeO₂ and (b) oil/water separation test.

Chapter 6

General Conclusions

This thesis was aimed to design and fabricate the super-liquid-repellent solid surfaces even for low-surface-tension liquids less than 20 mN m^{-1} by a practical multi-step wet process and propose the self-healing design to improve the durability super-liquid-repellency. Based on the observations of morphological structure, the analysis of surface composition and the evaluation of surface wettability by contact angle measurement for several liquids, general conclusions are summarized in this chapter.

The author proposed micro/nano dual-porous surface morphology to design the super-liquid-repellency. The nanopores channels, which were developed to normal to the surface of micropores, were used to introduce a pinning effect for avoiding the penetration of liquids into the pores. The dual-porous hierarchical morphology was fabricated by chemical etching of aluminum, followed by anodizing in sulfuric acid and pore-widening treatment in phosphoric acid. The advantage of the processes was that the size of micropits developed by chemical etching and also the size of nanopores are controllable by process conditions including the solution composition.

The micropits were formed by chemical etching in $\text{HCl} + \text{CuCl}_2$ mixed solution. The pits size decreased with an increase in the HCl concentration from several micrometers to submicrometers. The nanopores were introduced by anodizing of the etched aluminum in sulfuric acid. The nano-pore size was controlled by the following pore widening treatment in phosphoric acid from less than 5 nm to $\sim 30 \text{ nm}$. The porosity of the pit surface was then increased to more than 30%. In this manner, the micro-/nano-dual pore surface morphology of controlled pore sizes were readily formed by the wet

processes. The use of aluminum mesh with mesh opening of 150 μm , instead of aluminum plate, allowed to form triple porous morphology (Chapter 2).

After coating with fluoroalkylphosphate self-assembled monolayer (FAP) to reduce the surface free energy, the wettability was examined. The coating converted the surfaces from hydrophilic and oleophilic to hydrophobic and oleophobic. The etched surfaces with the FAP coating is superhydrophobic regardless of the etch pit size and even without nanopores. However, the presence of nanopores is of importance to superoleophobicity for liquids less than 40 mN m^{-1} . The contact angle hysteresis for rapeseed oil decreased to $\sim 3^\circ$ with an increase in the pore widening time, while the high advancing contact angle of $\sim 160^\circ$ remained unchanged. The size of etch pits influenced the liquids with the surface tension close to 20 mN m^{-1} , such as octane (21.8 mN m^{-1}); larger pit size was preferable to reduce the contact angle hysteresis. For liquids with higher surface tensions the contact angle and contact angle hysteresis were little influenced by the micro-pit size.

On the aluminum mesh surface with triple-pore hierarchical geometry, even hexane with a surface tension as small as 18.4 mN m^{-1} was repelled, compared with the lower repellency on the dual-pore hierarchical aluminum plate surface. The higher degree of hierarchy of the roughness is better for liquid repellency. The triple-pore hierarchical aluminum mesh became superhydrophobic and superoleophilic by changing the coating materials from fluoroalkylphosphate to alkylphosphate. This superhydrophobic/superoleophilic mesh is useful for oil/water separation.

The author also examined thermal and mechanical degradation of the

superoleophobic surface. The degradation was mainly associated with the damage of the organic coating layer (Chapter 3).

In order to obtain the durable superoleophobic surfaces, an attempt was made to introduce self-healing nature of the organic coating by infiltration of a coating agent, which was fluoroalkylsilane (FAS) in this study. The FAS-infiltrated dual-pore superoleophobic aluminum plate changed to superoleophilic after O₂ plasma treatment because of the damage of the organic coating. However, the superoleophobicity was completely recovered simply exposing the plasma-treated specimen in the laboratory air for >1 h. Repeated self-healing superoleophobicity was confirmed at least for eight times. Through a separate experiment using nanoporous alumina films without etching, the author has found that the recovering of the liquid repellency was better for smaller and longer nanopore channels. The surface area of the nanopores, not the pore volume, appears to be a controlling factor of the self-healing ability (Chapter 4).

Following the recent report by Azimi et al. showing the hydrophobicity of rare earth oxides without any organic coating, uniform thin CeO₂ layer was coated on stainless steel substrate by anodic deposition in this study. In contrast to the reported CeO₂ prepared by high temperature sintering or PVD, the present anodically deposited CeO₂ was hydrophilic immediately after deposition. However, the contact angle increased during air exposure and finally became hydrophobic. XPS analysis indicated that the hydrophilic-to-hydrophobic transition was associated with accumulation of contaminant hydrocarbon on the CeO₂ surface from the air atmosphere. When surface roughness was introduced on substrate, the hydrophobicity was enhanced. In particular, the etched and

CeO₂-coated stainless steel mesh became superhydrophobic. Since hydrophobicity was due to accumulation of hydrocarbon contaminants during air exposure, this surface showed the self-healing property (Chapter 5).

The present thesis study demonstrates that the multiscale porous surface morphology is useful for super-repellency for liquids even for low surface tensions. Such surfaces are produced by chemical etching, anodizing of aluminum and wet organic coating. All these processes are low-cost and practical. The self-healing superoleophobic surfaces have many potential applications including self-cleaning, anti-fouling, anti-corrosion, anti-ice/snow sticking and fluid drag reduction. Thus, it is expected that the results in this study will contribute to large-scale practical applications of super-liquid-repellent surfaces.

Acknowledgements

I first would like to express my deepest gratitude for Professor Hiroki Habazaki for his supervision and advices through my five and a half years at laboratory of Interfacial Electrochemistry. Without his kind guidance, sincere encouragement, continuous and great patient and deep and precise consideration, my thesis would never have reached to submit. Although I probably was the worst student among all his students and cause nothing but trouble for him, I was writing this composition thanks to him. Thank goodness I did returned to this laboratory and studied under him. I believe his future success and health.

I also would like to express my gratitude for Professor Kuniharu Ijiro and Kazuhisa Azumi, and Associate professor Yoshitaka Aoki, Hokkaido University, for their readings and wholesome advices and assessment of this thesis.

My sincere thanks also go to Assisntant professor Chunyu Zhu and Emeritus professor Masahiro Seo, and Postdoctoral fellows Dr. Damian Kowalski and Dr. Akira Koyama, Hokkaido University, Lecturer Etsushi Tsuji, Tottori University, Professor Soo-Gil Park, Chungbuk National University, Dr. Takashi Fujii, Nippon Steel & Sumitomo Metal Corporation, Dr. Yoshiki Konno, Kyoto Municipal Institute of Industrial Technology and Culture and Dr. Khurram Shahzad, Pakistani corporation, for their kind and beneficial help and advices not only about my study but also about a resercher's readiness.

I am also grateful to Ms. Tomomi Takeuchi, who is our research assistant on this

Acknowledgements

study, for her great and careful works.

I also would like to express my thank for Ms. Kanae Inoue and Ms. Yoko Iwata, who are secretaries of our laboratory, for their quick and perfect works about my research and conference trips.

I would like to show my appreciation to Associate professors Tomoya Takada, Chitose Institute of Science and Technology, Makoto Chiba and Keisuke Sugimoto and Professors Yasuhiko Furihata, National Institute of Technology, Asahikawa College, and Yukari Numata, Otaru University of Commerce, for leading me to the road to be a scientist. I pray for their future success and health.

I would like to be grateful to my seniors, Dr. Takahiro Misawa, Mr. Satoshi Tsunekawa, Mr. Masatoshi Ishizuka, Mr. Yoshiaki Taguchi, Mr. Kou Kakeda, Mr. Ryo Nonaka, for their kind communications and advices.

I am profoundly grateful to my colleagues, Hiroshi Oba, Kanbun Kure, Hina Sato, Naoto Hirata and Cao Jinhui, my juniors, Chiharu Kura, Cheong Kim, Kazumasa Kikutani, Takenori Yamasaki, Taiki Kimura, Yuki Nakayama, Fumitaka Kataoka, Keishi Inoue, Kohei Kobayashi, Shohei Kobayashi, Hiroyuki Noda, Shiki Matsuura, Takuya Hiraga, Yuto Okazaki, Kosuke Kuroda, Taisei Kobayashi, Ryosuke Sakashita, Ryosuke Tomizawa, Atsushi Kasuga, Tomoyuki Yamaguchi, Kanta Akane, Sho Fujimoto, Yusuke Kunii, Yuki Sato, Kentaro Takase, Keisuke Wada, Seongwoo Jeong, Tomohiro Inoue, Xiangjun Shen, Hikaru Kobayashi, Miku Saito, Manami Takata, Hajime Toriumi and Naohito Yamada, and all intern students and research fellows, inspired me and made my enjoyable life in this laboratory. They are treasures for my life. I pray for their future

success and health.

I also would like to give thanks to Dr. Yusuke Sato, Teijin Limited, who is my best friend for 10 years since we were students in National Institute of Technology, Asahikawa college, for his kind support to my most student life.

I would like to gratefully acknowledge the financial supports by Japan Society for the Promotion of Science for young scientists (Grant-in-Aid for JSPS fellows, No. 15J00802) and Ministry of Education, Culture, Sports, Science and Technology (MEXT).

Finally, I dedicate this thesis to my family who always supported and cheered me up in token of affection and gratitude.

Katsutoshi Nakayama

Sapporo, Japan

September 2017

List of Publications

Research articles on this study

- 1) Katsutoshi Nakayama, Etsushi Tsuji, Yoshitaka Aoki, Hiroki Habazaki, “Fabrication of superoleophobic hierarchical surfaces for low-surface-tension liquids”, *RSC Advances* **4**, 30927 (2014).
- 2) Katsutoshi Nakayama, Etsushi Tsuji, Yoshitaka Aoki, Soo-Gil Park, Hiroki Habazaki, “Control of surface wettability of aluminum mesh with hierarchical surface morphology by monolayer coating: from superoleophobic to superhydrophilic”, *J. Phys. Chem. C* **120**, 15684 (2016).
- 3) Katsutoshi Nakayama, Takuya Hiraga, Chunyu Zhu, Etsushi Tsuji, Yoshitaka Aoki, Hiroki Habazaki, “Facile preparation of self-healing superhydrophobic CeO₂ surface by electrochemical processes”, *Appl. Surf. Sci.*, **423**, 968 (2017).

Reviews

- 1) 幅崎浩樹, 藤井隆志, 中山勝利, 辻 悦司, 青木芳尚, 「陽極酸化を利用した金属表面の超撥水・超撥油化」, 表面技術 **65**, 426 (2014).
- 2) 幅崎浩樹, 中山勝利, 「陽極酸化技術による金属表面の超撥水・超撥油化」, 「超撥水・超撥油・滑液性表面の技術」第3章第4節, サイエンス&テクノロジー株式会社, 東京, 158 (2016).

Other research articles

- 1) Sigeaki Abe, Katsutoshi Nakayama, Daisuke Hayashi, Tsukasa Akasaka, Motohiro Uo, Fumio Watari, Tomoya Takada, “Development of a novel transparent substrate coated by carbon nanotubes through covalent bonding”, *Phys. Procedia* **14**, 147 (2011).
- 2) Sigeaki Abe, Katsutoshi Nakayama, Hirohisa Kobayashi, Takayuki Kiba, Tsukasa Akasaka, Shin-ichiro Sato, Motohiro Uo, Fumio Watari, Tomoya Takada, “Versatile

- surface modification by carbon nanotubes through an amide-bond formation”, *Nano Biomed.* **3**, 208 (2011).
- 3) Katsutoshi Nakayama, Tomoya Takada, Shigeaki Abe, Yoshihito Honda, Haruya Ikeyama, Yasuyuki Nakaya, Atsushi Furusaki, “Amide bond formation between carboxylated multi-walled carbon nanotubes and glass surface by using carbodiimide condensing agent and triazole derivatives”, *Mol. Cryst. Liq. Cryst.* **568**, 38 (2011).
 - 4) Tomoya Takada, Yuji Konno, Katsutoshi Nakayama, Pasan Tharuka Dunuwila, Yoji Maeda, Shigeaki Abe, “Chemical immobilization of multi-walled carbon nanotubes onto glass surface in aqueous media”, *Nano Biomed.* **4**, 113 (2012).
 - 5) Shigeaki Abe, Atsushi Hyono, Katsutoshi Nakayama, Tomoya Takada, Tetsu Yonezawa, “Scanning electron microscope observation of nano carbon materials with imidazolium-type room temperature ionic liquids”, *Jpn. J. Appl. Phys.* **52**, 01AH02 (2013).